UNIVERSITAT POLITÈCNICA DE CATALUNYA
BARCELONATECH
Departament d'Enginyeria Electrònica

NEW AUTONOMOUS SENSOR SYSTEM FOR THE CONTINUOUS MONITORING OF THE COMPOSTING PROCES S FROM THE INS IDE

Thesis submitted in partial fulfillment of the requirement for the PhD Degree issued by the Universitat Politècnica de Catalunya, in its Electronic Engineering Program.

Francesc Iu Rillo Moral

Supervisor: *J. Oscar Casas Piedrafita*

February 2016

To my grandparents: Ana, Ángeles, Juan and Rafael. In this moment of maximum maturity they are the link to my chilhood.

Paper stands everything.

— Juan López, engineer

ABSTRACT

The composting process is Nature's way of recycling organic wastes with a good quality organic fertilizer as a result. This process, though, needs of a thoroughly monitoring of temperature and humidity for a good resulting material. During this Ph.D thesis we developed a wireless temperature and humidity autonomous system that monitored from the inside of compost. The fact of measuring and transmitting from the inside implies the need of a protection for the circuit and an issue in the measure. Temperature suffers delays when measuring from the inside of a protection and, as such, we developed an algorithm, implementable on microcontrollers, to counteract the effects of first order step responses. Commercial humidity sensors need to be in direct contact with the environment they are measuring, but that is not possible in compost since they can get damaged. That is why we designed a humidity sensor based on coplanar capacitive electrodes that can measure through a protection layer. Compost has never been characterised as a transmission environment, and as such, communications in compost are innovative. The heterogeneity of the material and its changes in humidity, temperature and density made the transmission complex. We found the proper frequency band to commercially work in compost and the RF transmission model in compost to estimate attenuation vs distance.

PUBLICATIONS

As follows the publications resulting from this thesis are listed:

Casas, J. O.; Rillo, F. I. "Method for reducing response time in sensor measurement," *Review of Scientific Instruments*, 80, 085102 (2009).

You have five seconds to enjoy it,
and then you remember who you didn't thank.

— Helen Hunt, actress.

ACKNOWLEDGMENTS

I would like, first of all, to thank my supervisor, Oscar Casas, for the opportunity, the help, the teachings, the support, the friendship, the scolding and the fun. He is one of the most exceptional persons I have ever known and I am proud of being his student.

Next I would like to thank my family for the support. To my parents, Carme and Francesc, for everything I am and will be; to my sister and brother-in-law, Meri and Fer, for their affection; and to my grandparents, well you know, they are in the dedication.

I would like to thank my very dear friends and colleagues who supported me with chats, laughs, poker, beers and mojitos. To Dani Rodríguez, for he is my best friend; to Davide Vega, who can understand my research more than anyone; to Xavier Calvo, one of the most affective persons I have known; Javier López, who perfectly shares my worries; to Juan López, who is my teacher-colleague-student; to Guillem Enero, beer-poker best guy ever; and to Toni Oller, for supporting me when I had no money income at the beginning of my PhD. I also want to thank Sara Martínez, for she was part of my PhD for some time.

I would like to thank the family Aguilera-Esteve for they taught me something very valuable: I will be the same person after receiving my PhD. And yes, my PhD. is about some shit balls that are put into a fridge with some sensors from the elevators.

I want to thank all the ISI group for their support in my research. Specially to Marcos Quílez, who supervised the communication system for the European Project, to José Polo and to Carles Aliau. Also, thanks to Joan Albesa, the best laboratory mate I had and could have. Also to Marga López, Oscar Huerta and Montserrat Soliva from the *Escola Superior d'Agricultura de Barcelona* (ESAB).

Moreover, I would like to really thank:

Compoball: Novel on-line composting monitoring system. Unió Europea: FP7-243625-COMPO-BALL. 2010-2013.

Composens: Diseño de sistemas de sensores para la vigilancia y control del proceso de compostaje. DPI2010-14829. Ministerio de ciencia e innovación. 2011.

My thesis was developed and funded in the research framework of those projects, as well as to the Composting plants from Torrelles and Castelldefels.

Finally I want to thank the Sensors and Instrumentation research group from Graz, that accepted me for three months at their laboratory. Specially to Hubert Zangl, from whom I learned a lot and to Thomas Schlegl, Michael Moser and Thomas Bretterklieber.

I may have forgotten some people to thank, but I normally am a very thankful person so I guess they will not mind, hehe.

CONTENTS

LIST OF FIGURES

LIST OF TABLES

LIST OF ALGORITHMS

ACRONYMS

ACK Acknowledgement

CEPT European Conference of Postal and Telecommunications Administrations

CPU Control Processing Unit

DAQ Data Acquisition

EC European Community

EEPROM Electrically Erasable Programmable Read Only Memory

ERC European Radiocommunications Committee

EU European Union

FSS Frequency Selective Surface

I2C Inter-Integrated Circuit

IC Integrated Circuit

ISM Industrial, Scientific and Medical

IP Ingress Protection

MCU MicroController Unit

PET Polyethylene Terephthalate

PMR Personal Mobile Radio

PP PolyPropylene

PS PolyStyrene

PU Polyurethane

PVC PolyVinyl Chloride

RAM Random Access Memory

RC Resistance-Capacitance

RH Relative Humidity

RS232 Recommended Standard 232

RTD Resistance Temperature Detector

RF RadioFrequency

RFID RadioFrequency IDentification

SNR Signal-to-Noise-Ratio

SoC State of Charge

SoH State of Health

UART Universal Asynchronous Receiver Transmitter

Sigmund Freud was a novelist with a scientific background.
He just didn't know he was a novelist.
All those damn psychiatrists after him,
they didn't know he was a novelist either.

— John Irving, novelist

1

INTRODUCTION

Composting is Nature's way of recycling and represents a sustainable solution for the treatment of organic waste, whatever its origin. It is a natural biological process, carried out under controlled aerobic conditions, whereby various microorganisms, including bacteria and fungi, break down organic matter into an organic fertilizer. Since approximately 45 % to 55 % of the waste stream is organic matter, composting can play a significant role in diverting waste from landfills thereby conserving landfill space and reducing the production of leachates and methane gas.

The composting process requires of a good previous planing but also of a right monitoring of the control parameters. Being an aerobic, bio-oxidative and thermophile process the main parameters that permit interpreting what is happening are the temperature and the water evolution. If the initial mix is adequate and it has a correct humidity and oxygen concentration values, the composting material heats up as a result of the degradation activity of the microorganisms working in. As a thermophile process it is mandatory to maintain a minimal temperature, in order to clean the material, and it is also mandatory to maintain the temperature level not too high since it can end up affecting the decomposing microorganisms. Also, water is essential to sustain microorganisms, although if too much they die. Therefore, controlling temperature and humidity through time is a key factor to obtain good results.

Currently there is a lack of thoroughness in the composting process monitoring. This work aims to develop new proposals in the measure of temperature and humidity in compost, allowing optimizing the instrumentation and communication in terms of power consumption, cost and size. With field tests realized at the composting plant we will develop some guidelines and proper procedures to optimize the composting process, in order to increase the quality of the resulting product.

1.1 STATE OF THE ART

Composting plants are the locations where urban organic wastes are brought, in order to enter into the composting process to produce organic fertilizers.

Composting (Figure 1) is the biological decomposition and stabilization of organic material through the action of microorganisms (fungus and bacteria) with the presence of oxygen, and under controlled humidity and temperature conditions. In the first step of the composting process the organic wastes arrive to the plant and are prepared in order to be crunched and mixed. Normally, a magnet is used previously in order to extract possible metals. As follows, the organic wastes are put into piles, tunnels or matrices and the active composting stage begins, lasting between 5 and 6 weeks. During this stage most of the degradable organic matter is decomposed. A management plan is needed to maintain proper temperature, oxygen and moisture for the organisms.

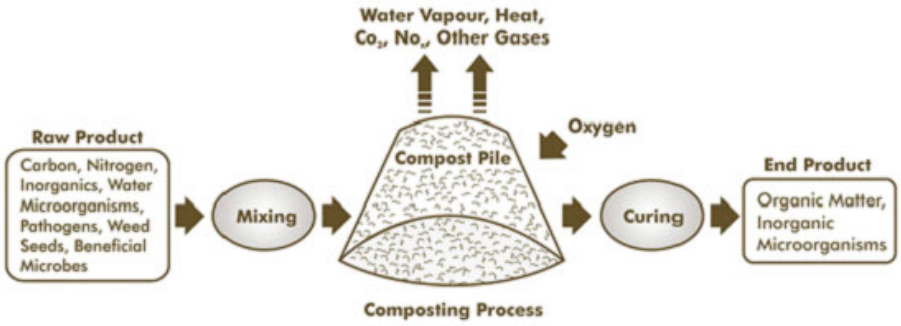

Figure 1: Composting process (Source: Composting manual. Alberta government. Canada)

During the composting stage, temperature reaches really high values due to the microorganism action, but it cannot surpass 70 °C because microorganisms start dying[1]. The ideal temperature range during this stage is 54 °C to 60 °C [2], if temperature goes beyond this range the compost is turned over or aired. During the curing stage, temperature drops dramatically and thus its monitoring is not as important (Figure 2).

Decomposition of organic matter needs of a high moisture level but decreases as the process goes on. During the decomposition stage (the first 40 days), the acceptable moisture content range goes from 40 % to 60 % [3] of relative humidity and can reach values of 80 % [4] (Figure 3). If moisture goes bellow this range the compost pile is wet.

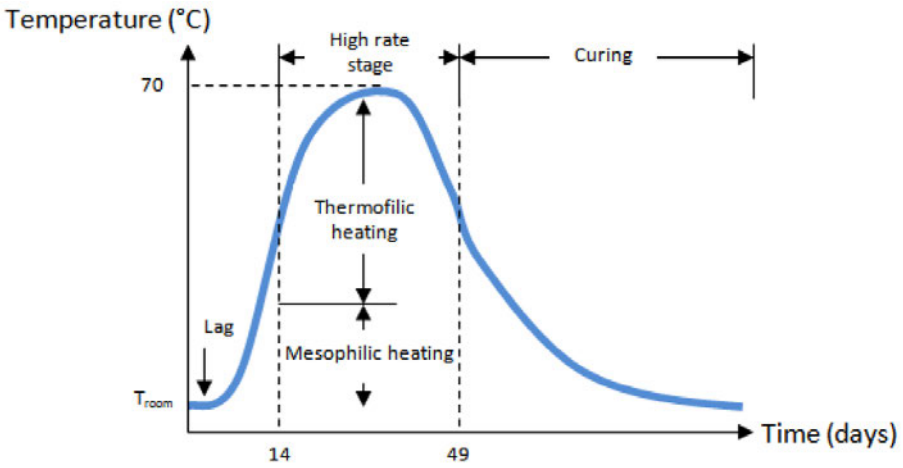

Figure 2: Composting process temperature evolution (extracted from [2])

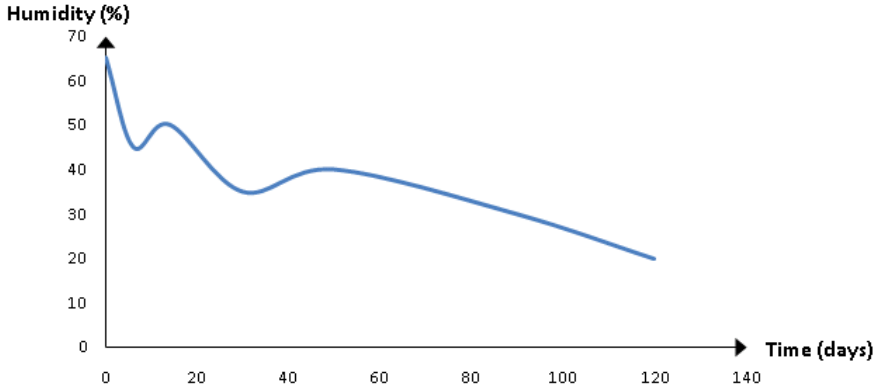

Figure 3: Composting process humidity evolution (extracted from [3])

After the active composting stage the curing stage follows. In this stage the microbial activity slows down and as the process nears completion, the material approaches environment air temperature. Finished compost takes on many of the characteristics of humus, the organic fraction of soil. The material will have been reduced in volume by 20 % to 60 %, in moisture content by 40 % and in weight by up to 50 % from the original organic matter [5].

The process produces at the end a product that is stable and can be beneficially applied to the land, and within its duration, heat is produced. Ideally, composting will enhance the usefulness of organic by-products as fertilizers, privately and commercially [6].

One could think of it as not only a non harmful way to deal with organic wastes, but also a way to produce high quality organic fertilizers. Reality, though, proves to be much less idyllic.

There are basically two group of individuals in the composting process: waste producers, responsible for the quality of the input, and plant workers, responsible for the quality of the output.

The **waste producer** is everyone of us who separates our day-to-day wastes. Their failure in their task can decrease the quality of the resulting compost. Metal is separated from the organic matter at the beginning of the process, paper is not a big deal since its decomposition is easy, plastic can damage the compost turner but it does not usually end in the resulting compost, glass is the big problem since it can easily avoid the filters of the composting plant and end up in the resulting compost. Still, these individuals do not influence in the scope of this scientific work.

The **plant workers** are in charge of the control of the whole composting process, from its waste obtaining to its compost output. As said before the monitoring has to be realized during the active decomposition stage of the composting process in order to get a good quality result and to avoid stink from the process. Although the main chemical and biological parameters affecting the composting process are well known, the developed models until now are very complex [7] and require expensive instrumental systems [8] for its validation and use. Also, the heterogeneity of the composting material would force having several measuring points. Consequently, those parameters are measured sporadically or they are not even measured. Therefore, the decision of activating the compost turner (in piles) or the air fan (in tunnels) in order to decrease the temperature of the compost results arbitrary or by intuition, and so is the decision of activating the water sprinkler in order to increase humidity.

The monitoring ways in composting result very subjective with the punctual use of sensors with no rigorous guideline regarding the proper monitoring when using them. This can be seen in [6] and even more subjectively in [9].

Therefore, since temperature is not properly controlled, the microorganisms in charge of the decomposition die and the process is not completely done. As for humidity, if too wet the composting pile stinks, and if not enough, the microorganisms die again.

Research in Europe [10] and in the United States [11] indicates that quality and marketing of the end product are the most crucial composting issues. There is a clear need of providing composting operators with improved process control technology, especially in view of increasingly stringent and evolving regulations, such as EC Regulation 1774/2002 which stipulates EU treatment standard for manure was 70 °C/1 hour/12 mm particle size [12], with some Euro-

pean countries imposing this only for products intended to be traded internationally. EC Regulation 208/2006 allows for the approval of alternative composting and bio gas standards for the treatment of animal by-products, whereby rather than setting out the process requirements (time/temperature/particle size) for treatment of raw material it permits the operator specifying their own treatment parameters, provided that the operator can demonstrate through microbiological testing of the finished product that the system has produced sufficient pathogen reduction (and of course provided the system still complies with all other aspects of 1774/2002). Such regulations, along with market demands for high quality, stable and safe composting are clear drivers for bridging the current gaps in compost monitoring and control technology.

Each country in the world has its own regulations to measure the quality of the resulting compost [13]. Still, the procedure is similar, the only change resides on the level of particles. A sample of compost is taken, isolating it in order to avoid contamination, and brought into a laboratory [14]. Once there, the levels of heavy metals and pathogens are measured and compared to the acceptable levels to decide whether it has a good quality or not.

This work will guide a research effort in the development of an on-line wireless system that will be effective for the measurement of both temperature and humidity at various points in the composting material.

Since compost is a heterogeneous material higher temperatures will be produced in punctual focus inside the composting material. Furthermore, current probes can be affected by external conditions. Thus, measures have to be realized from the inside. However, an enclosure for the circuit is needed to isolate the system from hazardous substances and from humidity. This enclosure will have to stand blows due to the action of the compost turner. For further information regarding the need of protection refer to Appendix B.

The fundamental material used for industrial and electrical isolation is the family of polymers [15]. But in front of high temperatures we have to discard Polyvinyl chloride (PVC) because it melts at temperatures of 80 °C [16] (and it becomes deformed earlier) and the blows of the compost turner makes Polyethylene terephthalate (PET) to be also discarded since its hardness is so great [17] that it can jam the shovels of the compost turner. Polystyrene (PS) is also discarded due to its low impact strength [18] along with Polypropylene (PP) [19]. Polyurethane (PU) on another hand has a high impact strength and high melting point (107 °C) [20], but it provides thermal isolation which will increase the transference of temperature

(which we have already considered when talking of temperature). Silicone has similar properties to PU but it has a great heat transference, which would make it ideal if it were not for its opposition to microbiological growth [21].

As said previously, the system will include wireless communication to be able to interact with to control it or to receive data of the monitoring. It is not a simple development due to the high humidity levels of compost. At the final stage, though, electronic methods will be supported by the fact that compost will be much more homogeneous and will have a lower water level. For transmission inside compost there can be arisen some possible solutions:

- The first one would be using sonar waves. We could have a system transmitting a pure acoustic frequency or an ultrasound (it could be activated through a wireless network) [22]. The emission could be temporally realized at different times and with different frequencies if we wish to identify each system.
- The second would be using a radio-frequency signal [23]. Low frequencies should be used (10-800 MHz).

When recovering the capsule at the end of the composting mechanical methods of object separation can be used, meaning that the sensor-capsule will have bigger dimensions than the ones of the holes of a filter where the compost material is made go past.

As a result of this work we have stated that we wish to develop some models in order to optimize the composting monitoring. Currently there are already models and guidelines for the same purpose. In Catalonia, the company with greatest involvement in the management of Composting plants is Metrocompost S.A[1]. They propose some guidelines and technologies to monitor the composting process. The control of parameters of the the process is realized through a set of probes which allow knowing these parameters at all times [24]. In Spain there are no regular models nor guidelines for the correct composting monitoring as in Alberta [6] or Ontario [25], which give clear recommendations of how to ensure that the composting operation maintains the ongoing quality needed. Most of these recommendations rely on grabbing samples and analyzing them which is an expensive procedure, temporally talking. We conclude that there is a lack of information for the proper monitoring of the composting process and therefore our models may be a good contribution for the organic matter management.

1 Public Limited Company (PLC). Incorporated (Inc.)

1.2 OBJECTIVES

The final objective of this thesis is to increase the quality of compost, developing a novel optimum humidity and temperature measuring system in a **continuous** and **autonomous** way at various points **inside** the composting material. The proposed solution will consist of a set of independent sensor nodes, i.e. the nodes will not require any external connections to feed or read the sensors, and which will be encapsulated in an inert material that will be capable of withstanding the harsh composting environment. The system will transmit data from the compost pile to existing data analysis systems and will be programmed to be controlled through receiving instructions via a wireless sensor network.

Hence the main objectives of this work are:

1. Optimization and development of the optimal interfaces for the temperature sensor system for the application of composting process monitoring.

In this objective the development of the temperature sensor system will be realized. We will take into account that the sensors will not be able to be in contact with the compost material and that the whole system will be embedded into a capsule, to isolate it from the worsen and damage of the contact with the environment and with the movement of the compost turner. We will search for different alternatives of temperature sensors and will choose one, and next its low-cost and low-power conditioning. Basically, a model to optimize the measure of temperature will be developed to advance on the technical state.

2. Wireless data communication study.

The main difficulty of this objective will be characterizing compost as a transmission environment by studying the signal propagation. We will require finding the optimum operation frequency to be able to determine a good enough transmission distance. At the same time we intend to find the RF propagation model for compost to have an estimation of the distance.

3. Development of the optimal method for the humidity sensor system for the application of composting process monitoring.

We will develop, design and test a humidity sensing method suitable to the characteristics of our problem involving measuring at low frequencies with the help of capacitive electrodes. An optimization of

the design of the measuring electrodes will be realized to maximize the sensitvity of the sensor. We will not focus on the electronics involved into the sensor system but on the physics, since that does not involve any improvement in the current state of the art.

Everything popular is wrong.

— Oscar Wilde, dramatist

2 TEMPERATURE SYSTEM

2.1 STATE OF THE ART AND PROPOSED SOLUTION

As stated in the Objectives, in this chapter and the following ones we will develop a temperature system for the autonomous measure of compost from the inside with a protection. To do so, we first need to know what the current solutions are and identify the problems against the improvements we can offer.

We have seen, that for temperature monitoring in composting the most extended use is the insertion of probes [26, 27]. There are many manufacturers involved in their distribution, some of them innovating with probes that are left put and communicate via wireless with a transceiver [28]. The idea of wireless sensors is supported and evolved to wireless sensor networks as in the patent [29] and in the products of [30]. The problem of this kind of product is that it results expensive and it has to be removed in order to turn over the compost material. This last problem is really old and even the possibility of inserting sensors in the turner shovels was arisen in some patents [31], but that is nonsense since the compost turner is activated only when the measured temperature is above some limited temperature levels.

A part from the probe insertion, there are really few solutions for the control of temperature; the following one refers to its monitoring on tunnels where no turning is realized and where the answer in front of a too high temperature is the action of a fan [32]. This cannot be extrapolated to other enclosures rather than tunnels. Therefore, as stated before, a good solution would be a sensor system measuring from the inside and protected enough to stand the blows of the compost turner (with an elastic protective enclosure) and to protect it from humidity (hence a minimum IP 67 grade is needed). The problem of a sensor inside a capsule is the delay due to the thermal capacitance that implies. In order to know what the temperature outside the capsule is we can use a method to estimate what the transient of the temperature sensor tends to [33].

On the other hand, to have a proper monitoring of the composting process a continuous measurement is needed. The time interval between samples has to be adaptable because temperature changes during the active decomposition stage are dependent of the location and the processing time. Temperature changes very slowly during the whole composting process and its values may vary half a degree per hour, and so a measuring rate of at least 30 min is more than enough for the monitoring of temperature.

If the system has to be measuring from the inside during the whole composting process autonomously, we will need to minimize the system consumption as much as possible. The basics for this will be based on a low-consumption microcontroller, one that allows exactly controlling which part of the microcontroller is active at each time, incredibly optimizing the overall consumption [34]. As said before, temperature changes in compost are really slow, this permits using the method to estimate the tendency of a first order transient [33], with which we will save taking at least 40 % of the samples of a transient.

We wish to elaborate a scalable product; meaning one able to be used in all kind of composting enclosures, therefore its prize has to be the minimum possible. To minimize its prize we could decrease the number of components; like using a conditioning of a direct sensor to microcontroller interface [35] or other conditioning techniques like Dynamic Power Management [36]. The composting process lasts around 2 months and as such, the batteries should be able to stand at least this time supplying the system.

2.1.1 *Proposed solution*

Our system is wished to be adaptable basically to different composting enclosures, like tunnels and piles, and to the different environments of geographical zones all over the world. Also it would be interesting to be able to use this same system on other processes rather than in composting enclosures, as for example in silos. The main and only critical changing factor of this adaptability is the time that the process lasts. With the development of a programming interface, the final user would be able to define the time of each stage of the process for the sensor system to act consequently.

As said in Chapter 1 the maximum temperature during the composting process is of 70 °C, therefore we will look for an electronic system able to work at this temperature or even until 80 °C just to have some margin. An accuracy of 0.3 °C and a precision of 0.1 °C is required by definition from the European project Compoball in

which this thesis have been developed, which agrees to the standard regulations of the European Union in the measure of temperature in compost.

Therefore, in this part of the Thesis we will develop a Temperature system that works autonomously inside compost protected by an elastic enclosure (IP67 to be able to protect both from water and chemical attacks) and supplied by some batteries, during around 2 months (which is the time a whole composting process lasts). The system will measure with an adaptable rate of at least 30 minutes and will keep the measures, with the time in which they were taken, in order to be able to see the evolution afterward.

2.2 DESIGN AND IMPLEMENTATION

The design and implementation of the Temperature system will focus on the conditioning of the sensor and everything related to the measure of temperature which will be what will determine the consumption of the system in front of the quality in the measure.

On the other hand, our system has to be embedded into a capsule as said in chapter 2, therefore in order to fit our circuit inside a capsule we have to consider minimizing its size and the size of all its components. Moreover, we find that the duration of the batteries has to last the whole composting process, and thus the components must have the minimal consumption. Besides, the composting process can reach values of temperature up to 70 °C, and so the operating temperature of our devices has to be over this value. Furthermore, we have specified that we wish to produce a scalable final product; therefore the total prize has to be the lowest.

In Appendix A the selection and justification of all the devices in the architecture can be found. As follows we will explain the innovative parts which are the sensor conditioning and the protective capsule.

2.3 SENSOR CONDITIONING

Our sensor conditioning has to be applied to detect the changes of the resisting sensor with the highest resolution-consumption rate. There are many solutions to reduce consumption and to improve the resolution, we will find a balanced one for our system. As follows the different alternatives in the bibliography are described.

Typically, to reduce analog and digital consumption a Dynamic Power Management (DPM) is commonly used (wake-up methods[37]), consisting on a sensor system remaining in different sleep times effectively reducing the consumption as long as the sleep time is much bigger than the active stage time. Another method commonly linked to the DPM is the Dynamic Voltage Scaling (DVS) for digital consumption reduction. While DPM reduces the overall consumption using low power modes, it is possible to have an additional energy saving if in the active stages the parts of the microcontroller not used are switched off. A part from the previous alternatives, the bibliography offers other less common solutions for digital consumption reduction, as including optimal synchronization of the communications[38] or optimizing pre-processing operations[39]. Another extended solution is the reduction of the clock in the mi-

crocontroller to reduc consumption (e.g use 32 kHz instead of 8 MHz).

A part from DPM, a very extended solution to reduce the number of components of the system, and sometimes the analog consumption, is using completely integrated systems, like the *Texas Instruments* MSC1210[40] to condition impedance bridges or the *Analog Devices* AD7745[41] to condition capacitive sensors. The problem of these solutions is their specific use and their high prize. Another trend is eliminating stages from amplitude conditioning (Figure 4a) or to integrate them into the digital processing. Eliminating the dynamic range adjustment (Figure 4b) would mean increasing the ADC number of bits and, sometimes, including the offset correction in the sensor conversion, this way it is possible to reduce consumption, physical dimensions and noise. This last solution proposes a system with an excitation, filtering and analog-to-digital conversion stages, limited by the number of bits of commercial ADCs. A new method proposes eliminating all the conditioning stages by applying a direct sensor-to-microcontroller interface (Figure 4c), designed to measure the value of a capacitance[42], resistance[43] or bridge[44]. Most sensors are impedance-based and used in almost all fields; from typical health monitoring[45, 46, 47] or acoustic sensing[48] to more specific uses as fireside corrosion measurement[49] or Salmonella typhimurium detection[50]. Therefore direct sensor-to-microcontroller interfaces seem an alternative to amplitude conditioning methods.

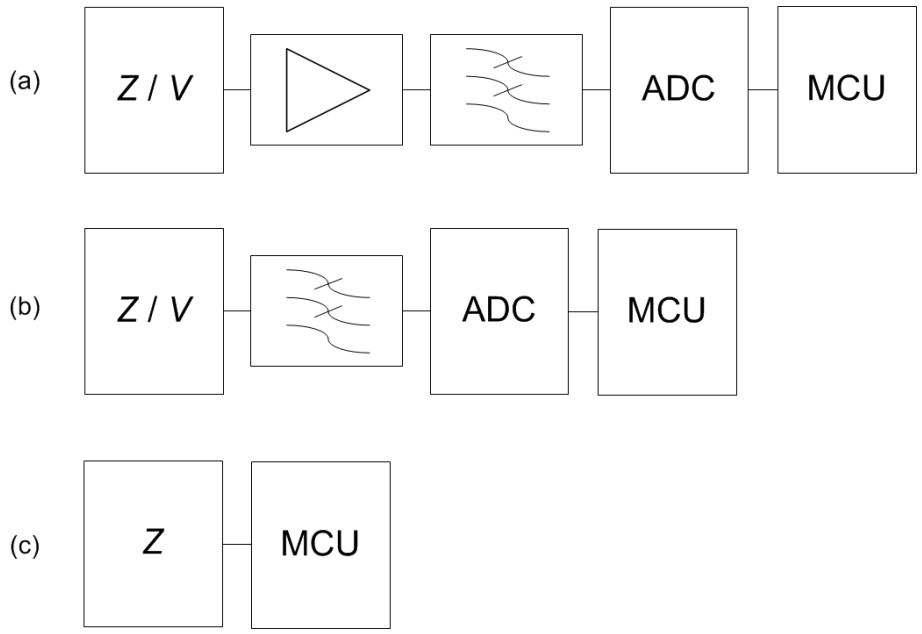

Figure 4: (a) Classic conditioning. (b) Classic conditioning without dynamic range adjustment. (c) direct sensor-to-microcontroller interface.

Hitherto, no systematic study has been realized to compare the consumption and effective resolution trade-off of the different conditioning alternatives, to see how the design is affected. Thus, our objective is comparing the performance of amplitude conditioning methods with direct sensor-to-microcontroller interfaces, by studying the consumption vs the effective resolution of each system. This way we would find out which is the most efficient sensor conditioning technique for our system.

2.3.1 *Theoretical models*

The alternatives for classic amplitude conditioning systems and direct sensor-to-microcontroller interfaces are explained in the following subsections. In classic conditioning systems, reactive sensors need of an AC excitation voltage or current, that implies additionally using a demodulator in front of the DC excitation needed on resistive sensors. For direct sensor-to-microcontroller interfaces the use of a resistive or a capacitive sensor does not matter and thus, if the consumption and noise were to be reduced using a resistive sensor (which we have not proven yet), in the case of using a capacitive sensor would be even better since the demodulator is not necessary.

Hence, the use of a resistive sensor as the input will serve also as a reference for the use of capacitive sensors.

Amplitude conditioning

Amplitude signal conditioning includes the sensor excitation, the dynamic range adjustment, the filtering, the analog-to-digital conversion (ADC) and the processing[51], as shown in Figure 4a. But the trend gives an alternative as can be seen in Figure 4b, representing the compromise between gain and number of bits. Although there are so many commercial ADCs with embedded amplifiers, if we avoid using an amplification (embedded or not) we avoid the current consumption of this stage and the noise it adds. However, the number of bits of the analog to digital converter (ADC) is bigger which, although it reduces the quantization noise, it may suppose an increase in its consumption according to the trend[52]. Still, the bibliography supports the fact of designs where increasing the number of bits of a Sigma-Delta converter does not imply an increase in the consumption[53, 54]. For example, if we take commercial Sigma-Delta converters *Analog Devices* AD7788 and AD7789 we see that with a resolution of 16 and 24 bits respectively their consumption is the same keeping the same characteristics, even with the increase in the conversion time. Therefore if the consumption is not critical and

the noise can be reduced then the choice would be using the second conditioning alternative (Figure 4b).

To realize the analysis the system is divided into three stages: the sensor excitation, the filter and the analog to digital conversion. The supplying of the sensor and the ADC is supposed to be provided by the microcontroller and, thus, can be off when not measuring, reducing the average consumption. Besides, the noise related to the output voltage of such a ports is negligible.

The consumption, the voltage of the signal and the noise influence are analyzed on each stage, and the final expression of the overall average consumption and effective resolution is given.

SENSOR EXCITATION STAGE This will be the stage critical in terms of consumption and noise, and thus we will focus on its optimization.

There are two conditioning options for resistive sensors: bridges and pseudo-bridges. When using a resistive sensor, bridges are not linear, but can come close to linear by increasing the additional resistors which also implies a reduction in consumption, an increase in noise [55] and a loss of sensitivity. The problem of doing so is that sensitivity becomes very low and needs of low-power gain stage to compensate. Pseudo-bridges use operational amplifiers to make the output linear, and can deal with the trade-off between consumption and noise by increasing the additional resistors in the same way as in bridges. Since the consumption of an operational amplifier can be of really few μA, bridges and pseudo-bridges become the same in terms of consumption and effective resolution. Since the only difference between them is that bridges are not fully linear it is reasonable to choose pseudo-bridges as the option to work with.

There are two typical circuits for conditioning through pseudo-bridges[56], unipolar as can be seen in Figure 5 and bipolar in Figure 6. On a first sight we can see that Figure 6 will not have mismatch problems since its output is regulated by an operational amplifier (OA). Still both circuits are analyzed in order to see which will need a lower ADC resolution.

A Pt1000 sensor , with a nominal resistance of $R_o = 1\,k\Omega$, besides, and a range of $R_x = [1 - 1.272]\ k\Omega$ are considered. In this stage, the variables that will determine the trade-off between the consumption and the effective resolution are k_i. Let us calculate first the voltage of the signal for the option in Figure 5.

This option would need a reference instead of ground in the positive input of the amplifier, or bipolar supplying, in order to be able to output the whole range of the sensor. Thus, to reduce the

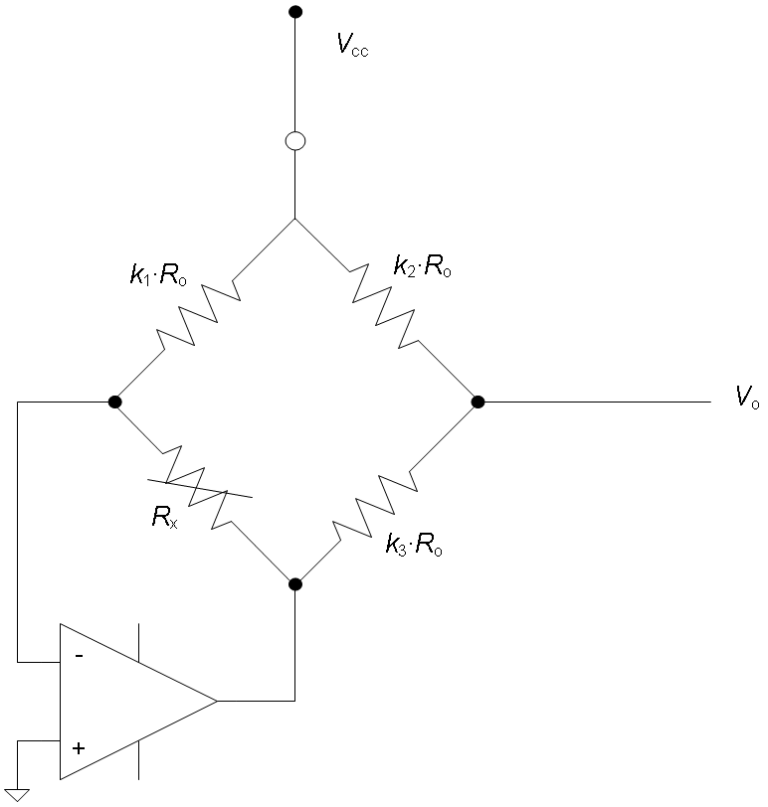

Figure 5: Sensor stage option (a) current flow

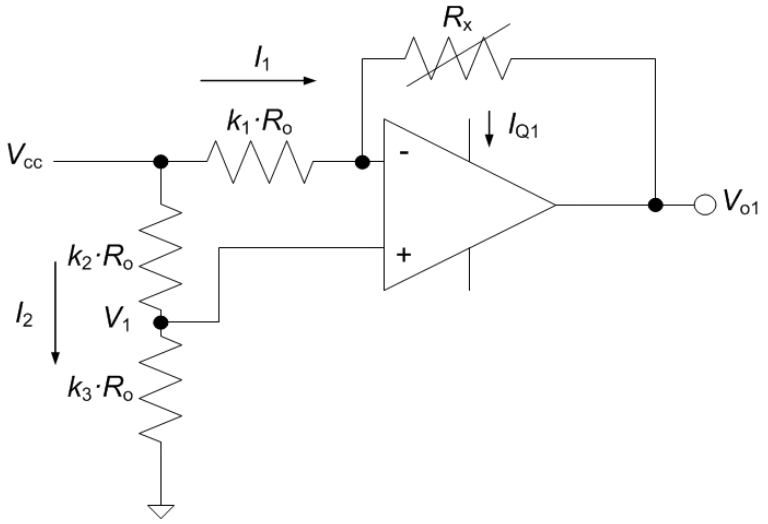

Figure 6: Sensor stage option (b) current flow

voltage level and to simplify the supplying the best option is using a unipolar solution.

The current flowing through the two branches of the Wheatstone bridge can be modeled as a system of equation based on the voltage dividers (Figure 5), which if solved (2.1) is obtained

$$V_{o1} = \left(k_3 - \frac{k_2\,(1+x)}{k_1}\right) \cdot \frac{V_{cc}}{k_2 + k_3} \tag{2.1}$$

If we optimize the dynamic range to improve the resolution with the relation of the three k_i constants we obtain that the possible ranges for α $\left(\text{where } \alpha = \frac{k_2}{k_2+k_3}\right)$ are $\left[0, \frac{2k_1}{k_1+1+x_{max}}\right]$ and for k_1 are $\left[\frac{(1+x_{max})\alpha}{2-\alpha}, \infty\right]$.

If we, for instance, take $\alpha = 0.1$ ($k_1 = 0.115$ and choosing $k_2 = 0.09$ and $k_3 = 0.081$), with the range of the resistive sensor (x = [0, 0.272], T›[0, 70] ^{o}C) and the input range of the microcontroller (V_{o1} =[0, 3] V), the number of bits needed in the ADC results of $n \approx 10$ bits (0.1 ^{o}C resolution).

Now let us calculate the voltage of the signal for the other case shown in Figure 6. The current flowing through the two branches can be modeled as a system of equation based on the voltage dividers ($R_x = R_o \cdot (1+x)$), which if solved (2.1) is also obtained.

Having the same output voltage, we see that both options need of the same resolution. Nonetheless, the second option avoids problems with impedance mismatch, and would not need of extra design features to work. Thus we will continue with that option as the sensor stage of the conditioning system.

If we analyze the voltage of the signal and the consumption with the help of Figure 6 we obtain that the voltage of the signal is the specified in (2.1). There are some limit values of k_2 and k_3 in order to stay within the limits of the power supply.

The current consumption is determined by the sum of currents supposing an infinite load resistor. If we analyze the circuit in Figure 6 we get that the overall sensor stage consumption is

$$I_{s1} = I_1 + I_2 + I_{Q1} \tag{2.2}$$

In terms of power, the total power of the circuit is the power in the different resistors plus the quiescent power $\left(I_{Q1}V_{cc}\right)$ and the

internal power depending on the amplification[57]. The resulting power consumption in Figure 6 is

$$P_{s1} = \frac{V_{cc}^2}{R_o}\left(\frac{1}{k_1}\left(1 - \frac{k_3}{k_2 + k_3}\right) + \frac{1}{k_2 + k_3}\right) + I_{Q1}V_{cc} \tag{2.3}$$

As we can see in equation (2.3), $\frac{k_3}{k_2+k_3}$ needs to be smaller than 1 in order to fulfill the equation.

As for the noise, when added it is possible to see that the predominant noises are the thermal and flicker noise and all the rest are negligible[57].

With that in mind, in Figure 6 the voltage and current thermal noise sources are identified. A method to determine the circuit gain for each noise source is to replace them by a conventional voltage or current source and calculate the corresponding gain [52].

We get the equation defining the output voltage in Figure 6 taking into account the voltage and current thermal noise sources, which shows the respective gain for each voltage and current source. Therefore, the Power Spectral Density (PSD) of the output voltage noise will be

$$\begin{aligned} e_{no1}^2 = &\left[\left(\frac{1 + k_1}{k_1}\right)^2 \left(\frac{k_3}{k_2 + k_3}\right)^2 (k_2 + k_3) + \frac{1}{k_1} + 1\right] e_{to}^2 \\ &+ \left(\frac{1 + k_1}{k_1}\right)^2 e_{n1}^2 + \left[\left(\frac{1 + k_1}{k_1}\right)\left(\frac{k_2 k_3}{k_2 + k_3}\right) + 1\right]^2 R_o^2 \cdot i_{n1}^2 \end{aligned} \tag{2.4}$$

If the output mean-square voltage noise when measured with a device whose bandwidth goes from f_L to $f_H$is [56]

$$E_{no1}^2 = \int_{f_L}^{f_H} e_{no}^2\,(f)\,df \tag{2.5}$$

and if the flicker noise for the respective frequency dependence of e_n and i_n for common operational amplifiers[57] is

$$e_n^2\,(f) = e_{no}^2 \cdot \left(f_{ce} \ln\left(\frac{f_H}{f_L}\right) + (f_H - f_L)\right) \tag{2.6}$$

$$i_n^2\,(f) = i_{no}^2 \cdot \left(f_{ce} \ln\left(\frac{f_H}{f_L}\right) + (f_H - f_L)\right) \tag{2.7}$$

we can finally obtain from (2.4) and with (2.5), (2.6) and (2.7)

$$E_{no1}^2 = \left[\left(\frac{1+k_1}{k_1}\right)^2\left(\frac{k_3}{k_2+k_3}\right)^2(k_2+k_3)+\frac{1}{k_1}+1\right]e_{to}^2 \cdot (f_H-f_L)+\left(\frac{1+k_1}{k_1}\right)^2 e_{no}^2\cdot\left(f_{ce}\ln\left(\frac{f_H}{f_L}\right)+(f_H-f_L)\right) + \left[\left(\frac{1+k_1}{k_1}\right)\left(\frac{k_2k_3}{k_2+k_3}\right)+1\right]^2 R_o^2\cdot i_{no}^2\cdot\left(f_{ce}\ln\left(\frac{f_H}{f_L}\right)+(f_H-f_L)\right) \tag{2.8}$$

FILTERING STAGE A first order low-pass filter is considered. Let us see the voltage of the signal and the consumption considering a resistance of the filter R_f and a capacitance of the filter C.

In this case voltage V_{o2} in steady state will equal the voltage in the input V_{o1}.

As for the consumption, if the capacitor is initially discharged, the voltage in this stage will be function of the time of charge. Therefore, the current evolution is represented by (2.9) as

$$I_f = \frac{V_{o1}}{R_f}\cdot\left(1-e^{-t/fi}\right)\cdot u(t) \tag{2.9}$$

If we consider the filtering time $l\tau = 6.9\tau$ or $l\tau = 9.2\tau$, the effective number of bits results 10 and 14 bits respectively and hence the average consumption is

$$I_{f,a} = \frac{1}{l\tau}\int_0^{l\tau}\frac{V_{o1}}{R_f}\cdot e^{-t/fi}d\tau = \frac{V_{o1}C}{l}\left(1-e^{-l}\right) \tag{2.10}$$

Knowing that $f_H = \frac{1}{2\pi RC}$ and considering that the values of l are really high (an integration time of 6.9τ or higher to decrease the time in active), making $e^{-l} \approx 0$, then

$$I_{f,a} = \frac{V_{o1}}{l\cdot 2\pi\cdot f_H\cdot R_f} \tag{2.11}$$

The power consumption similarly is

$$P_{f,a} = \frac{1}{l\tau}\int_0^{l\tau}\frac{2V_{o1}^2}{R_f}\cdot e^{-2t/fi}d\tau \approx \frac{V_{o1}^2}{l\cdot R_f} \tag{2.12}$$

And for noise, since there is no active components and there is only one resistor, the influence of noise for the filtering stage will add the thermal noise of that resistor, finally obtain the output mean-square voltage noise with (2.5), (2.6) and (2.7)

$$E_{no2}^2 = E_{no1}^2 + e_{tf}^2 (f_H - f_L) \tag{2.13}$$

PROCESSING AND ADC STAGE We will not consider the active processing stage because it is very variable depending of the compiler and the program, and because it is common for all the conditioning systems and, thus, not a differential point. The case of the ADC is different since there are conditioning systems not using it.

The analog-to-digital conversion is characterized by three time intervals: synchronism time (t_{sync}), sampling time (t_s) and conversion time (t_c). During these intervals the ADC is actively consuming.

As for the influence of noise for the ADC stage we will consider the Quantization noise, which is due to the finite resolution of the ADC, and is an unavoidable imperfection in all types of ADC. The ADC thermal noise is negligible with an order of 10^{-18}. Also, one has to be careful when choosing an ADC due to the error coming from non-linearities, gain error, etc.

The magnitude of the quantization error at the sampling instant is between zero and half one LSB. In the general case, the original signal is much larger than one LSB. When this happens, the quantization error is not correlated with the signal, and has a uniform distribution. Its RMS value is the standard deviation of this distribution, given by[58].

$$e_Q = \frac{Q}{\sqrt{12}} \tag{2.14}$$

where

$$Q = \frac{V_{FS}}{2^n} \tag{2.15}$$

V_{FS} is the full scale voltage and n is the number of bits of the ADC.

Therefore, the output mean-square voltage noise is

$$E_Q^2 = \frac{V_{FS}^2}{12 \cdot 2^{2n}} \tag{2.16}$$

OVERALL AVERAGE CONSUMPTION AND EFFECTIVE RESOLUTION

In order to calculate the energy consumption of the overall conditioning system (E_a), an average depending on the monitoring rate is realized

$$E_{s,a} = t_1 P_{s1} + t_f P_{f,a} + t_{ADC} P_{ADC} + t_{uC,sleep} P_{uC,sleep} \tag{2.17}$$

where t_T is the monitoring rate, t_f is the time the filtering stage is active

$$t_f = l \cdot \tau \tag{2.18}$$

t_{ADC} is the time the ADC is active in the worst case

$$t_{ADC} = t_{sinc} + t_s + t_c \tag{2.19}$$

$t_{uC,sleep}$ is the time the microcontroller is in sleep mode, which is the rest of the time

$$t_{uC,sleep} = t_T - t_1 \tag{2.20}$$

and t_1 is the time the sensor stage is active, which equals to the time spent on the filtering and amplification stage (the 2 additional clocks are the intervals between the active cycles of the ADC)

$$t_1 = t_f + t_{ADC} + 2 \cdot T_{SCLK} \tag{2.21}$$

As for the resolution, we will define it as the effective number of bits after the signal has been digitized

$$ENOB = \frac{10 \log\left(\frac{V_{o2}^2}{E_{noT}^2}\right) - 1.76}{6.02} \tag{2.22}$$

where E_{noT}^2 is the total output mean-square voltage noise

$$E_{noT}^2 = E_{no2}^2 + E_Q^2 \tag{2.23}$$

With equations (2.17) and (2.22) we will study the consumption and effective resolution of a classic conditioning system in section 2.3.1.

Time conditioning (Direct sensor-to-microcontroller interface)

This conditioning consists on the time measure of the charge and discharge of a capacitor through the resistive sensor, using the digital inputs and outputs of an MCU, whilst capturing the time with a counter. This time will depend directly on the resistance value of the sensor.

From the direct sensor-to-microcontroller interface options the three signal measurement method is the most recommended[43] (Figure 7). With it, it is possible to obtain a maximum absolute error of 0.08 Ω, a maximum non-linearity error of 0.01 % FSS and an accuracy of 0.10 Ω[43] when using a Pt1000 alpha class.

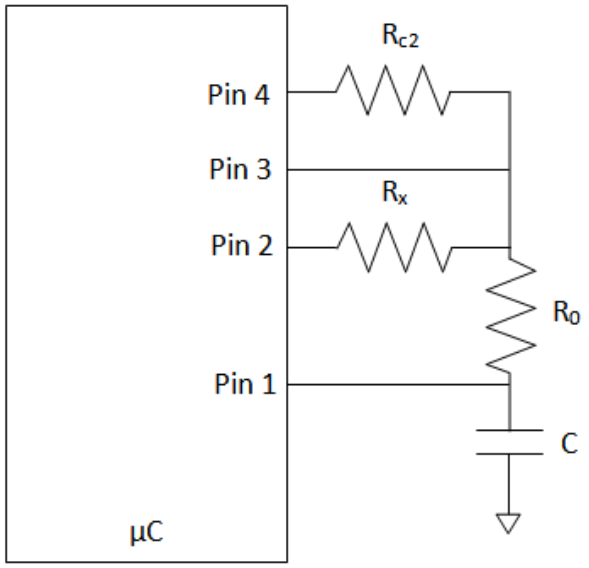

Figure 7: Direct sensor-to-microcontroller interface (three signal method)

It consists on charging a capacitor (1 µF in order to have a good speed-resolution trade-off) and discharging through three different pins. One of the pin lines contains a reference resistor R_{c2} (that can be around 1.5 kΩ a value near the nominal value of the sensor and not to high to suppose a noise problem), another is short-circuited and the last has the resistive sensor R_x. In other words, the sensor to measure plus a reference and an offset measure. R_0 is an additional resistor that is placed to limit the sink charge current to the maximal current sunk by a port pin (which is 20-25 mA and thus $R_0 = 330\,\Omega$) and hence to ensure a correct exponential discharge waveform.

From each discharge the time it lasts is measured, and with each time the resistance value of the sensor can be calculated with (2.24)[59]

$$R_x = R_0 \cdot \frac{N_x - N_{c1}}{N_{c2} - N_{c1}} \tag{2.24}$$

where N_x is the time counter of discharge through the resistive sensor, N_{c1} is the time counter of discharge through the short-circuit and N_{c2} is the time counter of discharge through the resistor R_{c2}.

OVERALL CONSUMPTION The overall consumption of this system only depends on the operation of the microcontroller and the charges and discharges of the three signal measurement method. As in the previous system we suppose that the microcontroller is sleeping most of the time except when measuring. Also while charging and discharging the MCU is sleeping until the trigger is activated. Therefore the overall energy consumption as an averaging of the consumption is

$$E_{s,a} = t_{uC,active} P_{uC,active} + t_{R_{c2}} P_{R_{c2}} + t_{R_{sc}} P_{R_{sc}} + t_{R_x} P_{R_x} + t_{uC,sleep} P_{uC,sleep} \tag{2.25}$$

where $t_{uC,active}$ is the time the microcontroller is active, $P_{uC,active}$ is the power consumption of the microcontroller when active, $t_{R_{c2}}$ is the discharge time through R_{c2}, $P_{R_{c2}}$ is the power consumption of the discharge through R_{c2}, $t_{R_{sc}}$is the discharge time through the short-circuit, $P_{R_{sc}}$is power consumption of the discharge through the short-circuit, t_{R_x} is the discharge time through the sensor, P_{R_x} is the power consumption of the discharge through the sensor, $t_{uC,sleep}$ is the time the microcontroller is asleep and $P_{uC,sleep}$ is the power consumption when the microcontroller is asleep.

EFFECTIVE RESOLUTION The effective resolution of the three signal measurement method can be simplified to (2.26) since $R_x \gg R_{sc}$ and $R_{c2} \gg R_{sc}$[60]

$$\frac{u(R_x^*)}{R_x^*} = u_{r,0} \cdot \sqrt{2} \tag{2.26}$$

where $u_{r,0}$ is the relative standard uncertainty of the discharging time measurement, which remains constant as in (2.27)

$$u_{r,0} = \frac{u(N_x)}{N_x} = \frac{u(N_{c1})}{N_{c1}} = \frac{u(N_{c2})}{N_{c2}} \tag{2.27}$$

Since the value of the discharge measurement cannot be considered small, the Slew Rate (*SR*) at the trigger point is small and hence the effects of the trigger noise predominate over those of quantization[21], therefore the relative standard uncertainty of the discharging time measurement can be approximated to (2.28)

$$u_{r,0} \approx \frac{\sqrt{E_{n,i}^2 + E_{n,e}^2}}{(V_{TL} - V_0) \cdot \ln\left(\frac{V_1 - V_0}{V_{TL} - V_0}\right)} \tag{2.28}$$

where $E_{n,i}$ is the rms voltage noise superimposed on the threshold voltage, $E_{n,e}$ is the rms voltage noise superimposed on the input signal to be measured, V_{TL} is the lower threshold voltage of the microcontroller, V_0 is the value to which the discharge arrives and V_1 is the value from which the discharge departs.

And thus the effective number of bits (*ENOB*) results as (2.29)

$$\mathrm{ENOB} = \log_2\left(\frac{R_{max} - R_{min}}{R_{max}} \frac{(V_{TL} - V_0) \cdot \ln\left(\frac{V_1 - V_0}{V_{TL} - V_0}\right)}{\sqrt{12} \cdot \sqrt{E_{n,i}^2 + E_{n,e}^2}}\right) \tag{2.29}$$

where R_{max} and R_{min} are the maximal and minimal values of the resistive sensor.

If a reduction of the trigger noise is realized (similar to filtering) by averaging several measures (above 100 measures[43]) then quantization noise predominates and the relative standard uncertainty can be approximated to (2.30)

$$u_{r,0} \approx \frac{T_s}{\sqrt{12}\tau \cdot \ln\left(\frac{V_1 - V_0}{V_{TL} - V_0}\right)} \tag{2.30}$$

where T_s is the time-base of the digital timer.

And thus the *ENOB* results as (2.31)

$$\mathrm{ENOB} = \log_2\left(\frac{T_{o,max} - T_{o,min}}{T_s}\right) \tag{2.31}$$

where $T_{o,min}$ and $T_{o,max}$ are respectively the minimal and maximal discharging times to be measured.

Theoretical results and discussion

First, the energy consumption and the effective number of bits are calculated for the amplitude conditioning and compared. Frequencies from 0.47 Hz to 20 Hz are considered; most of sensors work at low frequencies and the selected 16 bit ADC samples at 38.15 Hz and hence 20 Hz is more than enough. The 24 bit ADC cannot be used due to sampling time issues (the sampling frequency is 0.30 Hz and as such cannot sample signals between the specified frequency range) and also the consumption would be increased dramatically to achieve an extra bit of resolution.

In order to emulate a real example, a voltage supply of $V_{cc} = 3\,V$, a monitoring rate of 1 sample/h and a temperature of 273 K are supposed. Optimum devices are chosen in order to minimize their effect in the consumption and in the noise:

- A low power AD8500 amplifier is used, with a quiescent current of $I_{Q1} = 1.5\,\mu A$, a voltage noise density of $e_{no} = 190\,nV/\sqrt{Hz}$ and a current noise density of $i_{no} = 0.1\,pA$.
- The very low consumption MSP430F1232 microcontroller, with an active current of $I_{uC,active} = 580\,\mu A$ and a sleep mode current of $I_{uC,sleep} = 0.5\,\mu A$. The same MCU is supposed in both systems ($E_{n,i} = E_{n.e} \leqslant 1.45\,mV$, $V_{TL} = 1.65\,V$, $f = 8\,MHz$).
- The AD7788/AD7789 16/24 bit ADC, with a current supply of $I_{ADC} = 75\,\mu A$ for a $V_{DD} = 3.6\,V$, and a $T_{SCLK} = 200\,ns$; in the case of this device the working times are defined as $t_{sync} = t_T$, $t_s = 2^n \cdot T_{SCLK}$ and $t_c = 2 \cdot t_T$.

As said in the excitation stage section, α and k_1 need to be as near of 0 as possible. Figure 8 shows the effective number of bits in function of the energy consumption for $\alpha = 0.1$ and $k_2 = 0.09$ and with a range of k_1 from 0.1121 to 0.1414, the limit values to be within the voltage supply range. From left to right the points of the graph equal the values of effective resolution and energy consumption for bandwidth of [20, 17.6, ... , 0.538, 0.473] Hz.

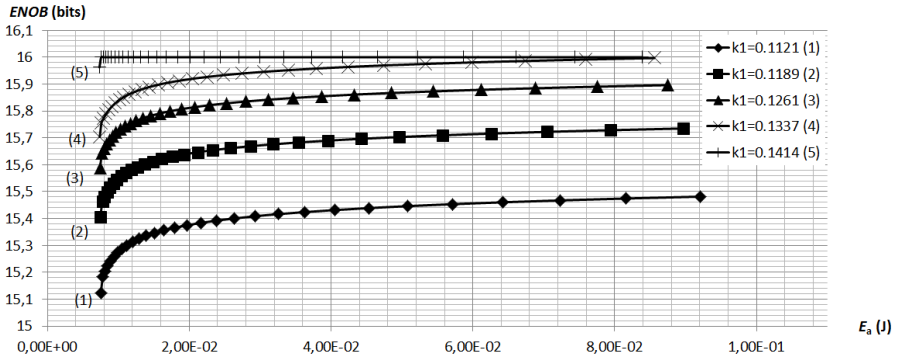

Figure 8: Energy consumption vs effective number of bits ($\alpha = 0.1$). Points of each series are, from left to right, 20, 17.6, ..., 0.538, 0.473 Hz. For a 16 bit ADC.

As we can see, the bigger the value of k_1 the better the resolution and the consumption. In this case Equation (2.8) is not affected by α and so it directly affects the signal amplitude of Equation (2.1) and the power consumption of Equation (2.3). Without taking a look at the equations, this behavior may seem not logical, but there are works that have proved the seemingly paradoxical noise behavior of some active circuits[61].

If we take a medium case in Figure 8 ($k_1 = 0.1185$) and we modify α within its limit values $[0.0712, 0.1060]$ we obtain Figure 9. This time, the smaller the value of α the better the resolution and the consumption, which implies that k_3 must be much bigger than k_2. This can be expected since if we take a look at equation 2.4 we see that the bigger $k_3$compared to k_2 the less noise and in equation 2.3 less consumption.

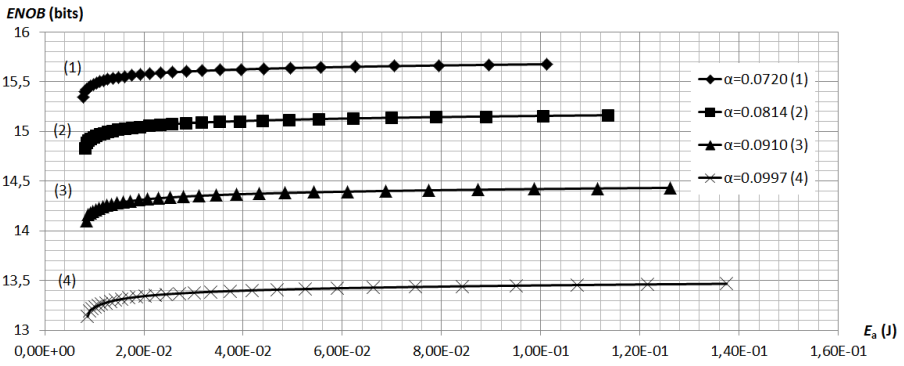

Figure 9: Energy consumption vs effective number of bits ($k_1 = 0.1185$). Points of each series are, from left to right, 20, 17.6, ..., 0.538, 0.473 Hz. For a 16 bit ADC.

If we take the bandwidth of 20 Hz for all the k_1 (Figure 10)and the alphas (Figure 11) we see that the error when increasing k_1 decreases

discontinously and the error when increasing alpha decreases as first order.

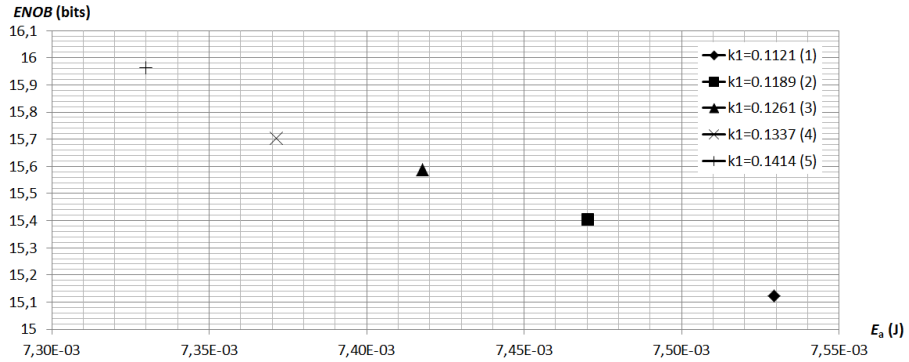

Figure 10: Energy consumption vs effective number of bits ($\alpha = 0.1$). f = 20 Hz

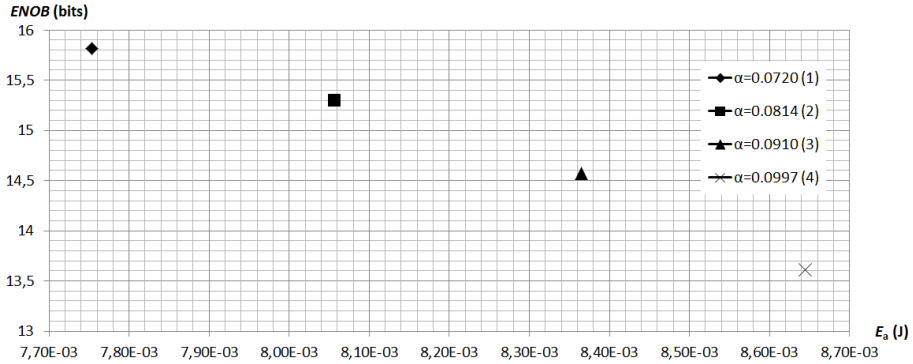

Figure 11: Energy consumption vs effective number of bits ($k_1 = 0.1185$). f=20 Hz.

If we were to use the 24 bit ADC we could only use it for very low bandwidths. An example for a 0.145 Hz bandwidth can be seen in Figure 12 and 13.

Now, we will show the performance of the time conditioning. This can be seen in Table 1, where the overall system energy consumption and the effective number of bits of the direct sensor-to-microcontroller are shown. The difference of *ENOB* averaging or not is considerably big, yet the energy consumption also increases but not drastically. The energy consumption of the direct sensor-to-microcontroller interface is characterized by a processing routine active during around 44 clock cycles, something negligible even multiplied by 100. The increase in consumption is mainly due to the charges and discharges of the three signal method.

As we can see, classic conditioning systems consume much more than direct sensor-to-microcontroller interfaces without averaging

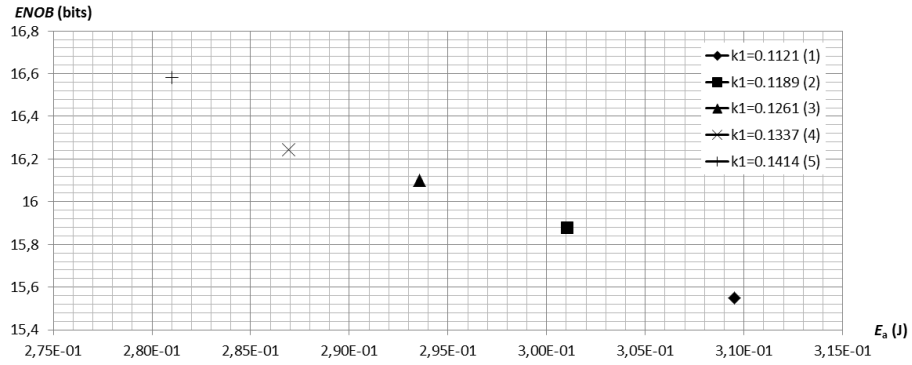

Figure 12: Energy consumption vs effective number of bits ($\alpha = 0.1$). f = 0,145 Hz. Using 24 bit ADC.

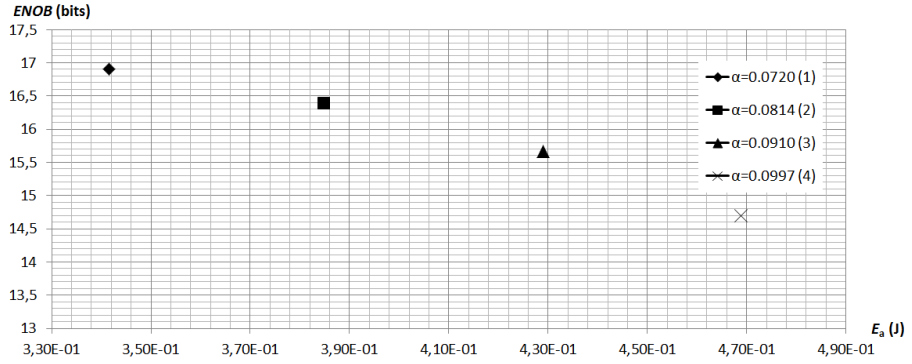

Figure 13: Energy consumption vs effective number of bits ($k_1 = 0.1185$). f=0.145 Hz. Using 24 bit ADC.

	ENOB (bits)	E_a (mJ)	t (s)
Not averaging	8.2	5.43	0.0217
Averaging	12.9	8.1	2.11

Table 1: *ENOB* and energy of using the direct sensor-to-microcontroller interface

and also when averaging. In terms of resolution it is possible to have more resolution in classic conditioning, since direct-interfaces have an offset noise due to the specifications of the microcontroller.

We see that classic conditioning has a limitation in terms of effective resolution (in Figure 8 we can see that the *ENOB* value saturates) and so the consumption, whilst direct interfaces have a limitation in terms of consumption (we cannot get a consumption lower than the dissipation of the interface resistances). Direct interfaces have also a limitation in terms of resolution due to the quantization noise, but we have to take into account that the direct interface was working with an MCU at 8 MHz. If a MCU working at a higher frequency

is chosen, the resolution can be increased when averaging (e.g. 20 MHz obtains 14.2 bits) with a negligible change in consumption. Also, the clock frequency cannot be increased indefinitely since you depend on your MCU and you may have to change of technology in order be able to increase it (and so the consumption may increase a lot). Still, the difference in resolution of classic conditioning is considerably big.

That is the result of using a Pt1000 as the input sensor in the conditioning system, if a Pt100 is used the result of classic conditioning is a big increase in consumption keeping the same effective resolution. In the case of the direct sensor-to-microcontroller interfaces (with reference resistor of 150 Ω of the three-signal method) the resolution is considerably decreased, when averaging, to around 9.5 bits keeping the same consumption. When not averaging the result is the same as using a Pt1000.

2.3.2 *Experimental setup*

To verify the theoretical models, experimental setups for both the amplitude and time conditioning were developed.

Amplitude conditioning

As said before, the main power consumer and noise source in the amplitude conditioning is the excitation stage. As such, we have designed a PCB circuit based on the excitation stage. The circuit was composed by the AD8500 amplifier and some pin connections to modify the value of the resistances in the circuit. The power supply was 3 V (sourced with a FAC-363 voltage supply).

CONSUMPTION To measure the consumption of the circuit a resistance (R_{meas}) was connected between the positive connection of the voltage generator and the supplying pin of the circuit. The voltage in this resistance was measured with a $6^1/_2$ digit resolution *Keithley* 2100 digital multimeter for each case, and the current consumption was obtained by applying the Ohm law.

As in section 2.3.1 a case with α constant and another with k_1 were analyzed.

In the case with α constant, the values of the resistances were measured ($R_o = 998.2\ \Omega$, $k_2 = 0.0902$, $\alpha = 0.0704$, $R_{meas} = 9.9\ \Omega$) and the voltage supplied $V_{cc} = 2.98$ V.

In Table 2 we can see the experimental values compared to the theoretical values (calculated with the measured values of the variables) in function of k_1. As we can see, the theoretical and experimental

values are almost identical and the consumption is both theoretically and experimentally demonstrated to decrease as k_1 increases. Experimental energy values where calculated taking into account that the acquisition time of the multimiter is the same as the theoretical ADC, meaning that the acquisition time of the multimiter was configured through a LabVIEW interface to be 20 Hz.

k_1	$I_{s,theo}$ (V)	$I_{s,exp}$ (V)	$E_{s,theo}$ (J)	$E_{s,exp}$ (J)
0.1115	$4.17{\cdot}10^{-3}$	$4.17{\cdot}10^{-3}$	$7.48{\cdot}10^{-3}$	$7.48{\cdot}10^{-3}$
0.1184	$4.06{\cdot}10^{-3}$	$4.06{\cdot}10^{-3}$	$7.43{\cdot}10^{-3}$	$7.43{\cdot}10^{-3}$
0.1261	$3.95{\cdot}10^{-3}$	$3.95{\cdot}10^{-3}$	$7.38{\cdot}10^{-3}$	$7.38{\cdot}10^{-3}$
0.1340	$3.86{\cdot}10^{-3}$	$3.86{\cdot}10^{-3}$	$7.33{\cdot}10^{-3}$	$7.33{\cdot}10^{-3}$
0.1425	$3.77{\cdot}10^{-3}$	$3.76{\cdot}10^{-3}$	$7.29{\cdot}10^{-3}$	$7.29{\cdot}10^{-3}$

Table 2: Consumption experimental vs theoretical results (α constant)

In the case with k_1 constant, R_o, R_{meas} and V_{cc} are the same and $k_1 = 118.95\ \Omega$ and $k_2 = 0.075$.

In Table 3 we can see the experimental values compared to the theoretical values (calculated with the measured values of the variables) in function of α. Again, the theoretical and experimental values are almost identical and the consumption is both theoretically and experimentally demonstrated to increase as α does.

α	$I_{s,theo}$ (V)	$I_{s,exp}$ (V)	$E_{s,theo}$ (J)	$E_{s,exp}$ (J)
0.0720	$4.62{\cdot}10^{-3}$	$4{,}59{\cdot}10^{-3}$	$7.70{\cdot}10^{-3}$	$7.68{\cdot}10^{-3}$
0.0814	$5.22{\cdot}10^{-3}$	$5{,}20{\cdot}10^{-3}$	$7.99{\cdot}10^{-3}$	$7.98{\cdot}10^{-3}$
0.0910	$5.84{\cdot}10^{-3}$	$5{,}79{\cdot}10^{-3}$	$8.28{\cdot}10^{-3}$	$8.26{\cdot}10^{-3}$
0.0997	$6.40{\cdot}10^{-3}$	$6{,}34{\cdot}10^{-3}$	$8.55{\cdot}10^{-3}$	$8.53{\cdot}10^{-3}$

Table 3: Consumption experimental vs theoretical results (k_1 constant)

NOISE To measure the effect of noise in the circuit we used the same setup as before but this time we measured the output voltage of the circuit with the digital multimeter (5 Hz bandwidth and 10 PLCs). The digital multimeter was switched on 30 minutes before the experiment began and was configured to measure 6 1/2 digits of resolution and its PLC was adjusted to reject the 50 Hz signal. The circuit was shielded with a metallic box connected to ground and it was placed inside an isolated chamber to avoid changes in temperature.

Both the k_1 and α modification cases were tested with the same characteristics as in the previous experiment. One could think that these are really small values for resistances, but as explained in section 2.3.1 k_1 and α need to be within certain margins to fulfill the dynamic range. Morevore, given that R_o is equal to 1000 Ω, as per the Pt1000 sensor used, the values of the rest of resistances are very small.

The output voltage was captured during 15 minutes at a 10 Hz rate. From the resulting signal we obtained the mean and standard deviation, and with those we could obtain subsequently the *ENOB* with equation 2.22 using the mean as the power of the signal and the deviation as the power of the noise.

In Table 16 and 4 we can see that the experimental and the theoretical results approximately coincide.

k_1	ρ (V)	σ_{exp} (μV)	$ENOB_{exp}$ (bits)	σ_{theo} (μV)	$ENOB_{theo}$ (bits)
0.1098	0.85	28.8	14.6	14.7	15.6
0.1189	1.00	26.5	14.9	13.7	15.9
0.1264	1.11	29.0	15.0	13.0	16.1
0.1320	1.17	29.8	15.1	11.9	16.3
0.1478	1.35	17.8	15.9	11.3	16.6

Table 4: Experimental and theoretical ENOB in function of k_1

α	ρ (V)	σ_{exp} (μV)	$ENOB_{exp}$ (bits)	σ_{theo} (μV)	$ENOB_{theo}$ (bits)
0.0720	0.97	33.2	14.5	13.7	15.8
0.0814	0.68	36.6	13.9	13.7	15.3
0.0910	0.41	31.9	13.4	13.7	14.6
0.0997	0.21	39.1	12.0	13.7	13.6

Table 5: Experimental and theoretical ENOB in function of α

As we can see, by changing the values of the resistances of the excitation stage, the value of the the *ENOB* changes, this shows us that they are one of the main noise sources for classic conditioning. If we were to use bigger values of R_2 and R_3 to reduce consumption it would always be limited by the consumption of the amplifier, and the resolution would decrease, but you can always reach a trade-off.

In Table 5 we see that the theoretical noise is constant and in Table 4 is not; this shows that k_1 greatly affects the noise proportionally.

We can see that the experimental value is slightly smaller than the theoretical one, this is mainly due to the variation on noise on the operational amplifier. There is no fixed variation of the typical voltage noise and the maximum voltage noise for operational amplifiers. However, we can find many examples that show that the maximum voltage noise of commercial operational amplifiers can be more than twice the typical (e.g. OPA2111AM, OPA2111BM, OPA2111SM, OPA37G, AD795JN/JR, AD795K).

In Figure 14 we can see the voltage measure for the case of alpha equal to 0.0720. As we can see, it follows a normal patern with the presence of noise which we confirm in Figure 15, where we see the histogram of that case with a gaussian behavior.

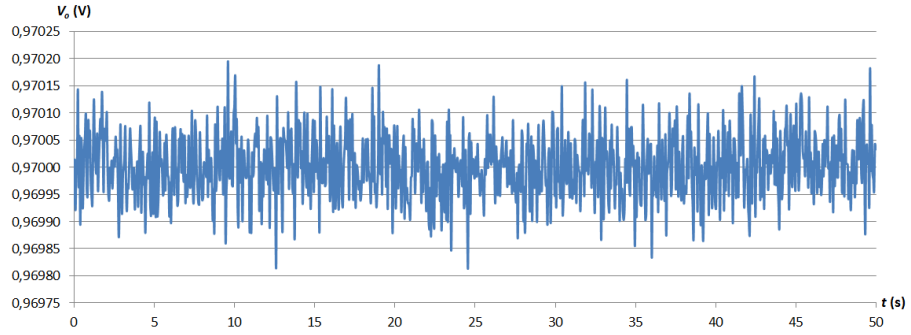

Figure 14: Voltage in function of time for the case of alpha equal to 0.0720

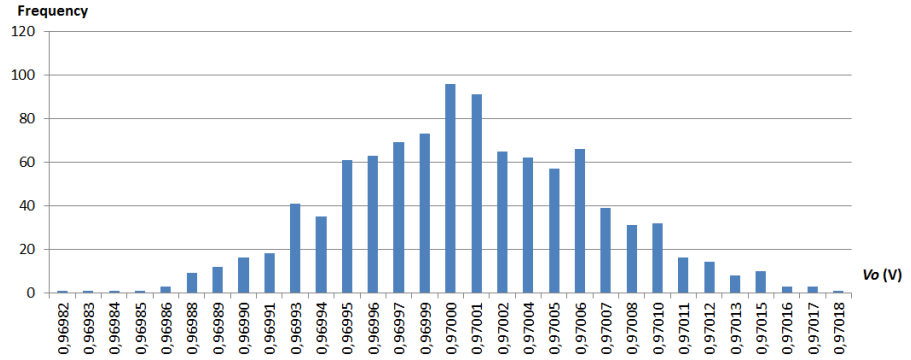

Figure 15: Voltage histogram for the case of alpha equal to 0.0720

Time conditioning

CONSUMPTION The consumption was measured in the same way as in the amplitude conditioning; this time, though, the consumption measuring resistance between the supply and the circuit was of 1796

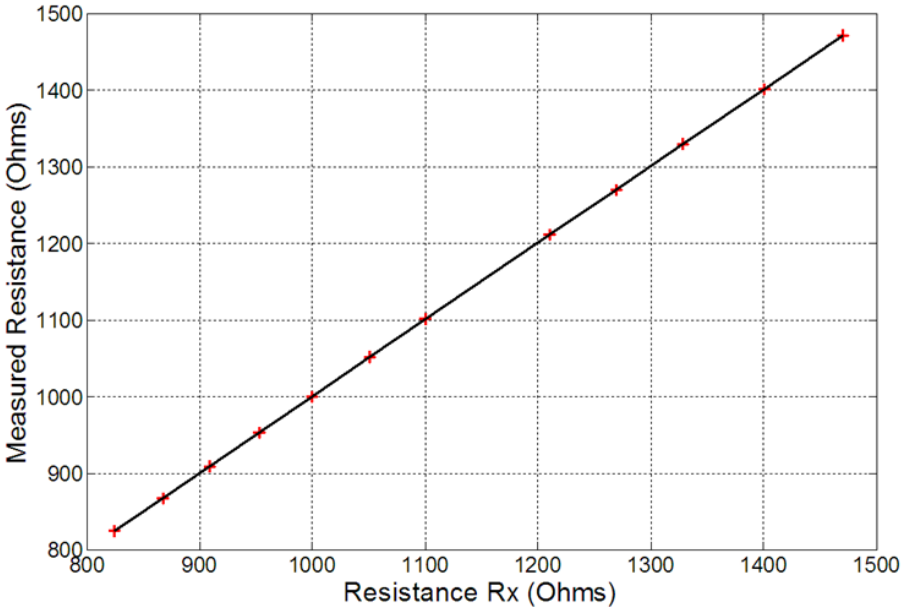

Figure 16: Calibration of R measured

Ω. Also, in this case we measured the consumption when the circuit is active and when the circuit is in standby. The voltage in the measure resistance was 0.89 V when active and 0.05 V in standby. Now using equation 2.25, as in the theoretical calculation, we find that the value of the energy results 5.01 mJ. As we can see, the experimental energy consumption is slightly less than the theoretical values. This may be due to the fact that the chosen theoretical current consumption value of the microcontroller was the worst case indicated by the datasheet.

NOISE To measure the noise effect in the measure of the temperature using direct interfaces we measured the resistance of the sensor and we compared it to its theoretical value in Figure 16; obtaining a maximum absolute error of 0.08 Ω, a maximum non-linearity error of 0.01 % FSS and an effective number of bits of 13 bits (which is translated as an accuracy of 0.10 Ω or 0.025 °C). This confirms the error induced by the own resolution on the climatic chamber.

Also, we took the circuit and inserted the Pt1000 to a *Hart Scientific* 9102S temperature chamber.We selected 6 temperatures to measure 10 samples at a stable temperature supplied by the chamber. For each temperature the average and standard deviation in the measure were calculated and subsequently the *ENOB* with equation 2.22.

The results of the experiment can be seen in Table 6. As it is possible to see, the value of the *ENOB* oscillates near the theoretical value seen in Table 1 when not averaging.

T (°C)	ρ (°C)	σ (°C)	*ENOB* (bits)
20	20.06	0.05	8.4
30	30.15	0.10	8.0
40	40.19	0.11	8.3
50	50.18	0.11	8.5
60	60.20	0.12	8.7
70	70.20	0.20	8.2

Table 6: Experimental measure of the *ENOB*

We can see that there is a systematic error in the measure of the temperature since the higher the temperature the higher the error. This systematic error can come mainly from the own resolution of the temperature chamber.

2.3.3 *Conclusions*

Direct sensor-to-microcontroller interfaces can be seen as a good alternative to classic conditioning when not needing a high *SNR* value. Their performance is clearly better in terms of consumption which makes them very suitable for autonomous sensor systems and our application. The consumption in the direct interface is 5.43 mJ or 8.10 mJ (depending on the measuring time) as seen in Table 1, whilst the energy in the classic conditioning oscillates from 30.40 mJ to 48.70 mJ as seen in Tables 2 and 3. The main consumer in classic conditioning systems is the excitation stage which direct sensor-to-microcontroller interfaces lack. It is the stage that consumes the most and the longest; that is the main reason for the difference in energy consumption. Direct sensor-to-microcontroller resolution is worse than classic conditioning systems, but can improve a little bit by averaging samples and giving up some of the consumption improvement. The bigger the number of samples to average the better the resolution and the bigger the consumption, until a value from which the resolution cannot improve anymore but the consumption keeps getting bigger. Still, we find that the resolution of the direct interface is enough for our requirements; moreover, this resolution is constant for all the temperature range whilst the resolution of the classic conditioning gets worse as temperature is increased due to the temperature effects in the ADC due to the voltage reference.

In other words, since we are looking for a low consumption system (e.g. autonomous system) and agree with a regular effective

resolution, then the system to choose would be the direct sensor-to-microcontroller interface. In this case, we could choose whether averaging or not, also seen as decreasing consumption or increasing the number of effective bits. Also we can overcome the resolution limitation by increasing the clock counter of the MCU. If we were interested in a high resolution system regardless the consumption, then the system to choose would be a classic conditioning. In this case, we could increase the value of k_1 and decrease α to increase the effective resolution and the consumption. However, we cannot improve indefinitely the effective resolution due to the maximum number of bits an ADC can have.

If a low resistance sensor were needed (Pt100) we would have to choose between the very low consumption of the direct sensor-to-microcontroller interface or the very big resolution of classic conditioning systems. Resolution can be increased and consumption can be decreased in direct interfaces, when averaging, by increasing the capacitor of the three-signal method. Still this solution implies increasing the size of the circuit which goes against the philosophy of direct interfaces. On the other hand, if the capacitor is increased and no averaging is realized, the resolutions remains the same and the consumption is increased. Hence, in the case of a Pt100, we could play with the size of the capacitor of the direct interface to reduce even more the consumption of the system and increase the resolution as long as an averaging is realized.

Finally, if we were to use capacitive sensors, direct interfaces have exactly the same consumption and resolution, whilst classic conditioning worsens due to the addition of the demodulation module. Still, regular capacitive sensors are normally of pF, and as such, very big resistances (around MΩ) would be needed in direct interfaces since this method cannot work with high bandwidth systems. In this case, the consumption would be even lower, but the resolution would slightly decrease.

As such, we will have enough with the *SNR* provided by the direct interface for our application and we will be able to have a very low consumption which will extend the lifetime of our batteries.

2.4 CAPSULE

As said in at the beginning of this chapter, the circuit needs to be protected from humidity and blows. Besides, in the State of the art (Chapter 1) it is indicated that if we use a method to deal with transference heat delays, the proper material to use as a capsule is Polyurethane.

2.4.1 *Material suitability*

We have analyzed the characteristics of three types of polyurethane: rigid, rigid-foam and foam. As follows we will see how this material stands the hard conditions of the composting process in terms of temperature and humidity, together with the effect of the liquids segregated during the composting process and the physical effects.

Temperature and humidity resistance

A foam polyurethane capsule was tested with different time cycles simulating the composting process and on extreme temperature and humidity conditions inside a *FCH* climatic chamber (Fig. 17), in order to simulate the aging of the capsule on a quick way. The capsule was able to stand temperatures up to 80 °C and an 80 % of humidity without notably modifying its physical properties.

Figure 17: FCH climatic chamber used in our tests

This capsule was also tested on real composting conditions, inside a pile, in the Castelldefels (Barcelona outskirts) composting plant, and inside an urban composter. The capsule properties were not significantly modified due to the effect of temperature and humidity. In the following sections we will see how their weight change and their degradation was minimal, not only because of temperature and humidity, but also due to the gasses produced during the composting process and the action of the compost turner.

A rigid polyurethane capsule was tested on real composting conditions inside an urban composter, and some minor deformation was observed.

Physical resistance

Figure 18: Capsules after the test in an urban composter

Two capsules of foam polyurethane (of 9 mm and 12 mm of diameter) and 2 capsules of rigid polyurethane were introduced inside a composter to test their resistance to the physical conditions during the composting process. The capsules were not visibly affected by the pressure and the weight of the composting material, as can be seen in Fig. 18. Table 7 shows how the weight was not significantly affected by the process. The increase of weight was obviously due to the waste attached during the composting process.

	Initial weight (g)	**Final weight (g)**
9 mm foam polyurethane ball	215.7	224.9
Rigid polyurethane ball 1	95.9	100.8
Rigid polyurethane ball 2	88.5	91.0

Table 7: Changes in the weight after the composting process in the composter

Also, 10 foam polyurethane capsules were introduced on a pile from a composting plant just before the compost turner was activated, in order to see their blow resistance. They had the number cut on them and ball 9 and 10 were cut removing a significant slice (Fig. 19a). Only six of them were recovered, the other four were lost due to the action of the compost turner. They were not destroyed; they bounced out of the pile. As we can see in Table 8 the change in weight indicated an increase as in the last test, this was again due to the waste that was attached to them during the composting process. This waste only affected externally.

	Initial weight (g)	Final weight (g)
Ball 1	190.53	191.13
Ball 2	208.88	209.29
Ball 3	181.31	-
Ball 4	202.92	-
Ball 5	194.22	-
Ball 6	188.84	-
Ball 7	212.97	213.36
Ball 8	174.17	175.03
Ball 9	182.70	183.43
Ball 10	196.24	196.49

Table 8: Changes in the weight after the composting process in the pile

No damage was observed in either type of capsule after the compost turner had gone several times through the compost pile (Fig. 19b). The only effect was that foam polyurethane capsules bounced and some of them went out of the pile during the process. Rigid polyurethane could minimize this effect and probably avoid the loss of the capsules.

(a) (b)

Figure 19: (a) Capsules before the test. (b) Capsules after the test (only the ones recovered).

Chemical resistance

Looking at the result of both tests, regarding the introduction of the balls inside composting environments, we can conclude that the capsules are chemically resistant to the chemicals produced during the composting process.

2.4.2 *Material influence on the temperature sensor system*

It is clear that the material stands the conditions of the composting process. Now we will see how the material influences into the composting process and into the operation of the temperature sensor system.

As said in the first section, polyurethane delays the thermal radiation and thus the measure of temperature changes can be affected from the inside of a polyurethane capsule. We will quantify this delay and will propose a solution to deal with it.

Theoretical calculation

In order to verify the validity of our experimental results we need to compare to the theoretical calculation.

The heat transference time (Δt) from the environment at a temperature (T_f) to a body with a volume defined by an area (A) and a width (x) (plain surface) at another temperature (T_o) comes defined by[62]

$$\Delta t = \frac{\Delta Q \cdot x}{A \cdot \Delta T \cdot K} \tag{2.32}$$

where K is the body material conductivity, ΔT is the temperature change $T_f - T_o$, and ΔQ is the thermal energy change $Q_f - Q_o$which comes from

$$Q = E_a \cdot \#atoms \tag{2.33}$$

where E_a is the average kinetic energy per atom defined as

$$E_a = \frac{3}{2} \cdot k \cdot T \tag{2.34}$$

where k is the Boltzmann constant which is $1.3806504 \cdot 10^{-23}$ J/K. And the number of atoms of the body $\#atoms$ is defined as

$$\#atoms = m \cdot N_a$$

where m is the mass of the body and N_a is the Avogadro number of $6.02214179 \cdot 10^{23}$ mol^{-1}.

Experimental setup

The balls were cut into pairs of slices of different widths. For each width a Pt1000 was inserted between the pair of slices and all was left inside a refrigerator during a long time. Once cold, the resistance of the Pt1000 between the polyurethane slices was measured with a *Keithley* 2100 digital multimeter until it reached the environmental temperature. The data measured was captured through a *Intel Pentium* M (1.70 GHz and 512 MB RAM) laptop, connected to the multimeter, with the 2100 *KI-TOOL* 1.0 software at a rate of 1 sample each 2 seconds.

Foam polyurethane

In Table 9 we can see the development of the theoretical calculation of the delay in the heat transfer for a pair of 0.6 cm slices of foam polyurethane (with a thermal conductivity of $K = [0.14 - 0.39]$ w/mK). Experimentally we obtained a heat transfer delay of $1.78 \cdot 10^3$ s which would be equal to a thermal conductivity of 0.21 w/mK. As we can see this value is between the ranges of the theoretical calculation.

Physical properties		
x (m)	width	$6 \cdot 10^{-3}$
A (m^2)	area	$3.12 \cdot 10^{-3}$
m (g)	mass	15.45
Measured variables		
T_o (K)	Initial temperature	281.72
T_f (K)	Final temperature	291.74
Calculated variables		
$E_{a,o}$ (J/atom)	Initial average kinetic energy per atom	$5.83 \cdot 10^{-21}$
$E_{a,f}$ (J/atom)	Final average kinetic energy per atom	$6.04 \cdot 10^{-21}$
# atoms (atom)	Number of atoms	$9.30 \cdot 10^{25}$
Δt (s)	heat transference time	$[9.51 \cdot 10^2 - 2.65 \cdot 10^3]$

Table 9: 0.6 cm measured magnitudes [63]

In Table 10 we can see the same for a pair of 1.2 cm slices. Experimentally we obtained a heat transfer delay of $4.73 \cdot 10^3$ s which would be equal to a thermal conductivity of 0.26 w/mK. As we can see this value is also between the ranges of the theoretical calculation.

Physical properties		
x (m)	width	$12 \cdot 10^{-3}$
A (m^2)	area	$3.63 \cdot 10^{-3}$
m (g)	mass	30.20
Measured variables		
T_o (K)	Initial temperature	281.74
T_f (K)	Final temperature	292.83
Calculated variables		
$E_{a,o}$ (J/atom)	Initial average kinetic energy per atom	$5.83 \cdot 10^{-21}$
$E_{a,f}$ (J/atom)	Final average kinetic energy per atom	$6.06 \cdot 10^{-21}$
# atoms (atom)	Number of atoms	$1.82 \cdot 10^{25}$
Δt (s)	heat transference time	$[3.19 \cdot 10^3 - 8.89 \cdot 10^3]$

Table 10: 1.2 cm measured magnitudes [63]

It is, thus, theoretically and experimentally demonstrated that the thicker the layer of polyurethane the bigger is the heat transfer delay.

Rigid foam polyurethane

In Table 11 we can see the development of the theoretical calculation of the delay in the heat transfer for a pair of 0.8 cm slices of rigid foam polyurethane (with a thermal conductivity of $K = [0.14 - 0.39]$ w/mK).

Experimentally we obtained a heat transfer delay of $1.22 \cdot 10^3$ s which would be equal to a thermal conductivity of 0.33 w/mK. As we can see this value is between the ranges of the theoretical calculation.

In Table 12 we can see the same for a pair of 1.8 cm slices. Experimentally we obtained a heat transfer delay of $6.06 \cdot 10^3$ s which would be equal to a thermal conductivity of 0.35 w/mK. As we can see this value is also between the ranges of the theoretical calculation.

It is, thus, theoretically and experimentally validated that the thicker the layer of polyurethane the bigger is the heat transfer delay. Also we see that rigid foam polyurethane has a higher thermal conductivity than foam polyurethane.

Physical properties		
x (m)	width	$8 \cdot 10^{-3}$
A (m^2)	area	$3.85 \cdot 10^{-3}$
m (g)	mass	15.75
Measured variables		
T_o (K)	Initial temperature	281.32
T_f (K)	Final temperature	290.21
Calculated variables		
$E_{a,o}$ (J/atom)	Initial average kinetic energy per atom	$5.83 \cdot 10^{-21}$
$E_{a,f}$ (J/atom)	Final average kinetic energy per atom	$6.01 \cdot 10^{-21}$
# atoms (atom)	Number of atoms	$9.48 \cdot 10^{24}$
Δt (s)	heat transference time	$[1.05 \cdot 10^3 - 2.92 \cdot 10^3]$

Table 11: 0.8 cm measured magnitudes [63]

Physical properties		
x (m)	width	$18 \cdot 10^{-3}$
A (m^2)	area	$3.74 \cdot 10^{-3}$
m (g)	mass	35.10
Measured variables		
T_o (K)	Initial temperature	281.96
T_f (K)	Final temperature	291.89
Calculated variables		
$E_{a,o}$ (J/atom)	Initial average kinetic energy per atom	$5.84 \cdot 10^{-21}$
$E_{a,f}$ (J/atom)	Final average kinetic energy per atom	$6.04 \cdot 10^{-21}$
# atoms (atom)	Number of atoms	$2.11 \cdot 10^{25}$
Δt (s)	heat transference time	$[5.40 \cdot 10^3 - 1.51 \cdot 10^4]$

Table 12: 1.8 cm measured magnitudes [63]

Rigid polyurethane

In Table 13 we can see the development of the theoretical calculation of the delay in the heat transfer for a pair of 0.4 cm

slices of rigid polyurethane (with a thermal conductivity of $K = [0.14 - 0.39]$ w/mK).

Physical properties		
x (m)	width	$4 \cdot 10^{-3}$
A (m^2)	area	$9.05 \cdot 10^{-3}$
m (g)	mass	60
Measured variables		
T_o (K)	Initial temperature	338.68
T_f (K)	Final temperature	297.67
Calculated variables		
$E_{a,o}$ (J/atom)	Initial average kinetic energy per atom	$7.01 \cdot 10^{-21}$
$E_{a,f}$ (J/atom)	Final average kinetic energy per atom	$6.16 \cdot 10^{-21}$
# atoms (atom)	Number of atoms	$3.61 \cdot 10^{25}$
Δt (s)	heat transference time	$[8.48 \cdot 10^2 - 2.36 \cdot 10^3]$

Table 13: 0.4 cm measured magnitudes [63]

Experimentally we obtained a heat transfer delay of $8.74 \cdot 10^2$ s which would be equal to a thermal conductivity of 0.39 w/mK. As we can see this value is between the ranges of the theoretical calculation.

We can see that rigid polyurethane has a higher thermal conductivity than foam and rigid foam polyurethane.

Proportionally it is possible to see that 1 cm of rigid polyurethane is translated as 36.43 min of delay, which would be the recommended monitoring rate due to the slow changes of temperature during the composting process. If faster measuring were needed a compensation method can be used in order to estimate/compensate each time the real temperature the capsule is trying to acquire. This problem can be fixed by using a new method for estimating the final value of a first-order system transient [33].

2.4.3 *Method for reducing response time in sensor measurement*

The previous section has stated the type of delay provoked by a plain model. However, we state that we are going to use a spheric capsule. The heat transfer equation for a spherical model is [64]

$$\frac{1}{r^2}\frac{\partial}{\partial r}\left(r^2\frac{\partial T}{\partial r}\right)+\frac{1}{r^2 \sin_{,,}}\frac{\partial}{\partial \theta}\left(\sin\theta\frac{\partial T}{\partial \theta}\right)+\frac{1}{r^2\sin\theta}\frac{\partial^2 T}{\partial \phi^2}+\frac{q_G}{k}=\frac{1}{\alpha}\frac{\partial T}{\partial t} \tag{2.35}$$

As can be seen the equation has three space coordinates (r, θ , ϕ) and time (t) as variables. This implies a complex analysis that would e presumably better analyzed through simulation. Nevertheles, the case we propose is placing a plain 15 x 3 mm Pt 1000 sensor separated 2 mm from the edge of a spheric capsule of radius 90 mm. If we calculate the volume of sphere section in front of the sensor we obtain 85,32 mm^3, whilst if it were a plain section it would be 90 mm^3. This gives a volume error of 5.21 %. This volume error will not be much relevant when concluding that for a plain section or for a sphere section the delay provoked in the measure is a predominating first order system.

Many sensor and instrumentation systems may have transients that extend their operation time, although they may sometimes give information about a measured quantity[65]. As a result, many transient analysis have been developed for this purpose[66]. When no information is contributed by the transient, it is desirable to reduce the time required to find the final value. Temperature systems are a typical example of systems in which transients are always present for measurement purposes[67], for instance, sensor systems contained in enclosures. Therefore, when two bodies of different temperatures are brought into contact, energy will flow spontaneously from one to the other[68]. This flow takes a certain time to be completed before the bodies reach a thermal equilibrium state. This effect may be critical in certain situations. We may have a very slow system in which a long time is required to receive the final value, or an autonomous system in which sample-taking is a critical factor for the battery life. Most of these system transients, in temperature or similar applications, are modeled as first-order systems[69], and the trend is often to use methods to optimally reduce the order of systems[70].

Solutions already exist for measuring time reduction, but they usually involve complex calculations such as estimating the delay through complex operations[71]. Our objective now is to look for

the final value of a first-order system using a method comprising simple equations able to be implemented on interfaces with low computational capacity, such as a microcontroller. This method has to be able to estimate the value by taking a few samples at the beginning of the transient. Therefore we will develop the generic first-order equation for a step function input, propose the method and simulate the theoretical model. Finally, an experimental setup will be devised in order to validate the theoretical method.

Theoretical model

On a first-order system, the relation input $x(t)$ and output $y(t)$ is defined as the differential equation

$$a_1 \cdot \frac{dy(t)}{dt} + a_0 \cdot y(t) = x(t) \quad (1)$$

If $x(t)$ is an step function $u(t)$, then the expression of the output of a first-order system is defined as the following expression[56]

$$y_i = (V_f - V_o) \cdot \left(1 - e^{-\frac{t_i}{\tau}}\right) + V_o \quad (2)$$

where y_i is the value of a certain magnitude at a time t_i, τ is the delay constant, V_o is the initial value and V_f is the final value of the magnitude. V_f and τ are unknown quantities, but in this work V_f is the only variable to be estimated.

The objective is to develop a method with simple expressions, i.e. formed by operations implementable on a low-cost microcontroller, so the exponential term will have to be eliminated N samples can be taken as displayed in Figure 20. For values of N above 3, the system becomes mathematically very complex, thus we focus on $N = 2, 3$ to fulfill the objective of achieving a simple equation. The cases in which the samples follow an arithmetic or geometric progression will be studied, in order to find the optimal equation. Therefore two cases have been studied: a) in which the samples are taken for $t_x = k \cdot t_1$ and b) in which the samples are taken for $t_x = t_1 + k \cdot \triangle t$.

The system developed for $t_x = k \cdot t_1$ and $N = 2$ is

$$\begin{cases} y_1 = (V_f - V_o) \cdot (1 - x) + V_o \\ y_2 = (V_f - V_o) \cdot \left(1 - x^2\right) + V_o \end{cases} \quad (3)$$

where $x = e^{-\frac{t_1}{\tau}}$.

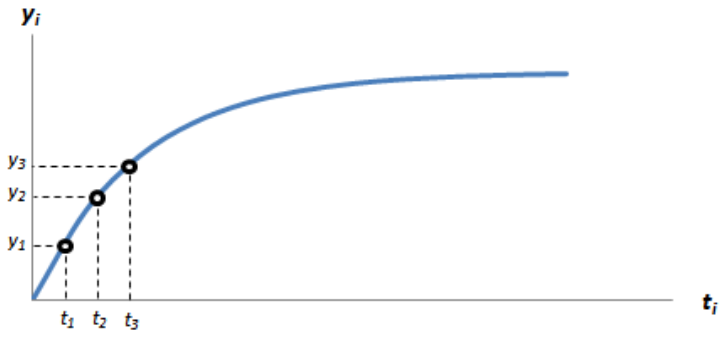

Figure 20: Samples taken on a first order system ($V_o < V_f$)

If we isolate x in the first equation of the system and replace it in the second, the final value V_f can be estimated with

$$V_f = \frac{y_1^2 - y_2 \cdot V_o}{2 \cdot y_1 - y_2 - V_o} \quad (4)$$

In the case of $N = 3$, the solution is

$$V_f = \frac{y_1 \cdot y_2 - y_3 \cdot V_o}{y_1 + y_2 - y_3 - V_o} \quad (5)$$

For $t_x = t_1 + k \cdot \triangle t$ and $N = 3$, the system developed is

$$\begin{cases} y_1 = (V_f - V_o) \cdot (1 - x) + V_o \\ y_2 = (V_f - V_o) \cdot (1 - x \cdot z) + V_o \\ y_3 = (V_f - V_o) \cdot (1 - x \cdot z^2) + V_o \end{cases} \quad (6)$$

where $x = e^{-\frac{t_1}{\tau}}$ and $z = e^{-\frac{\Delta t}{\tau}}$.
And the final value V_f can be estimated with

$$V_f = \frac{y_2^2 - y_3 \cdot y_1}{-y_1 + 2 \cdot y_2 - y_3} \quad (7) \qquad (2.36)$$

Figure 21 shows the equations that result from solving the systems of the different cases.

Equation (4), which results from the case $N = 2$ taking the samples on $t_x = k \cdot t_1$, is a simplification of the other two cases, as displayed in Figure 21.

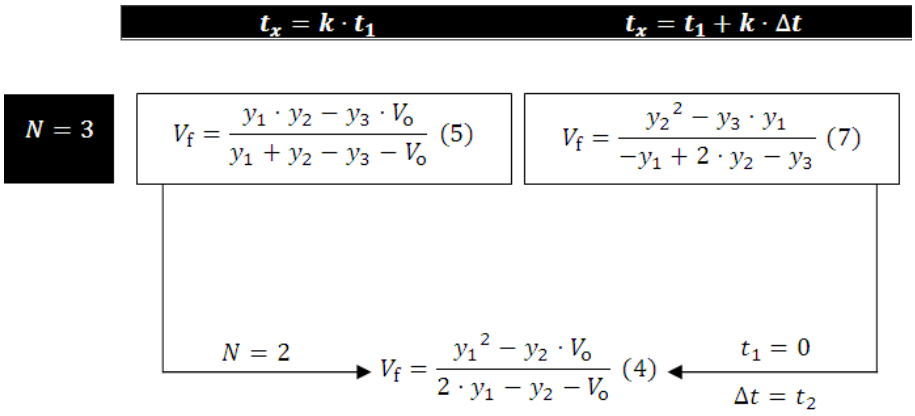

Figure 21: Resulting equations

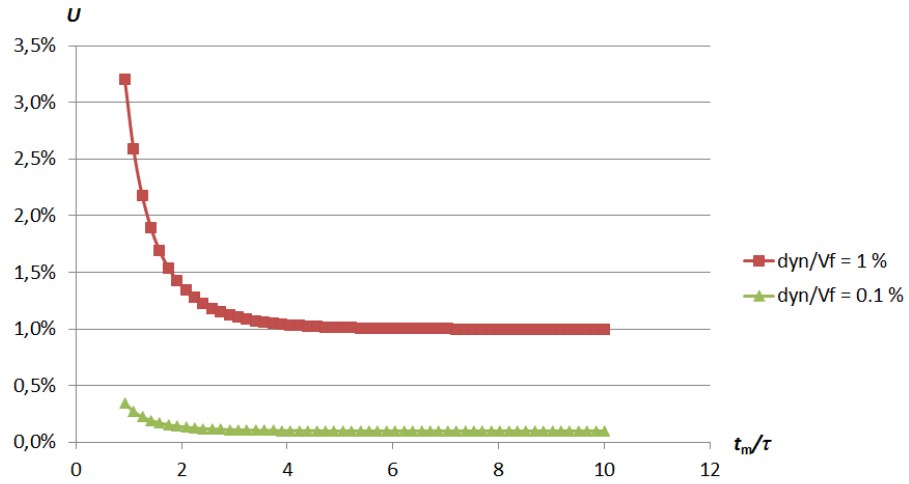

Figure 22: Uncertainty of Equation (7) for $dy_1/V_f = dy_2/V_f = dy_3/V_f = [0.001, 0.01]$ in function of Δt

Equation (7) does not depend on V_o, which makes it suitable when the initial value of an analyzed first-order system is unknown. Equation (4) and Equation (5) do have this information, which is equivalent to having an extra sample.

If we calculate the uncertainty of Equation (7) for y_1, y_2 and y_3 (asuming the uncertainty for systems of 10 and 8 bits) and we display the relative uncertainty for Equation (7) in function of Δt (which can be expressed as $\Delta t = \tau/4$, depending on the system) we obtain Figure 22.

Where

$$\frac{dV_f}{dy_1} = \frac{y_2 - 2y_2y_3 + y_3^2}{(-y_1 + 2y_2 - y_3)^2} \tag{2.37}$$

$$\frac{dV_f}{dy_2} = \frac{-2y_2y_1 + 2y_2^2 - 2y_2y_3 + 2y_3y_1}{(-y_1 + 2y_2 - y_3)^2} \tag{2.38}$$

$$\frac{dV_f}{dy_3} = \frac{y_1^2 - 2y_2y_1 + y_2^2}{(-y_1 + 2y_2 - y_3)^2} \tag{2.39}$$

As we can se, the more separated the samples are, the less uncertainty.

Simulation

On a real application, the value of V_o, y_1, y_2 and y_3 have an uncertainty due to different kinds of disturbance. In order to see the sensibility of our equations in front of these disturbances, we simulated a first-order system with an added Gaussian noise signal. The first-order system had an amplitude of $\pm$ 2 V and a delay of 1 s. The simulation was performed using the commercial software *Matlab* R2006b v.7.3.0.267.

Figure 23 and 24 show the error of the calculation made using equations (4), (5) and (7) for 8- and 10-bit systems, respectively which is what our system requires according to our specifications (*SNR* of the analyzed first order 48 and 60 dB). This error depends on when the last sample (time measured, t_m) was taken. For Equation (7) two situations are described, one in which the samples are separated $\tau/2$ and one for $\tau/4$. The graphs are represented with discretized data, taking a limited number of samples, enough to see the behavior of the equations.

All the cases show that the later in time the samples are taken, the lower the error is. This was expected because faster amplitude variations are found at the beginning of a first-order system.

The measuring time of all equations is the same, which means that their behavior is also the same. However, Equation (4) appears to behave better during the earlier measured times, whereas Equation (7) has a better performance when the samples are sufficiently separated in time. The difference may matter for 8-bit systems, but it becomes insignificant for 10-bit systems. Therefore, in applications with a high *SNR*, any of the three equations can be used without too much trouble.

If we compare the result for Equation 7 $\Delta t = \tau/4$ in these figures with the one in Figure 22 we see that the same levels of uncertainty are achieved for both 10 and 8 bits.

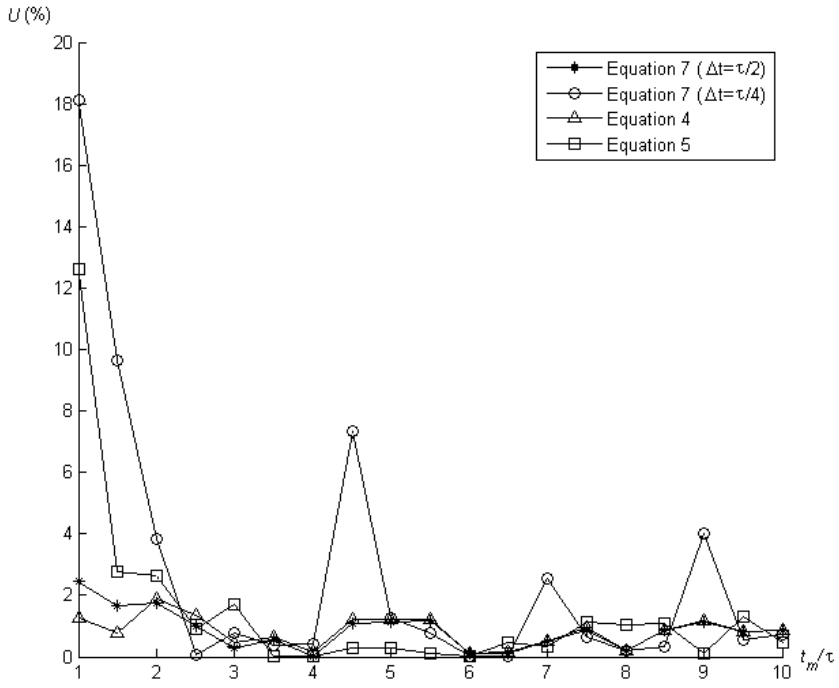

Figure 23: Error of the calculation depending on when the last sample (time measured t_m) was taken, using the different equations (8-bit systems)

Once the behavior of the three equations is known, we need to learn the time required to obtain an acceptable level of error.

Table 14 shows when the last sample (t_m/τ) should be taken in order to obtain an error lower than 1 % (a value close to the quantification error on 8-bit systems), and the delays (τ) that a first-order system may have in time. These are specific values found by simulating the application of the three equations in 8-bit systems, which means that each value was found by doing a single simulation, so the values have a high variation due to noise. Equation (7) analyzes the case of the samples that are separated $\tau/2$.

A wait of around $2.7{\cdot}\tau$ is required (taking into account the worst case) if the equations of Figure 21 are used, whereas around $4.6{\cdot}\tau$ would be required if the generic Equation (2) were used to obtain an error lower than 1 %. Consequently the same result is achieved in 59 % of the time previously needed for 8-bit systems.

The time required to achieve an error lower than 0.1 % (a value close to the 10-bit system quantification error) in a 10-bit system is shown in Table 15, which is the result of simulations made using the same characteristics as those displayed in Table 21.

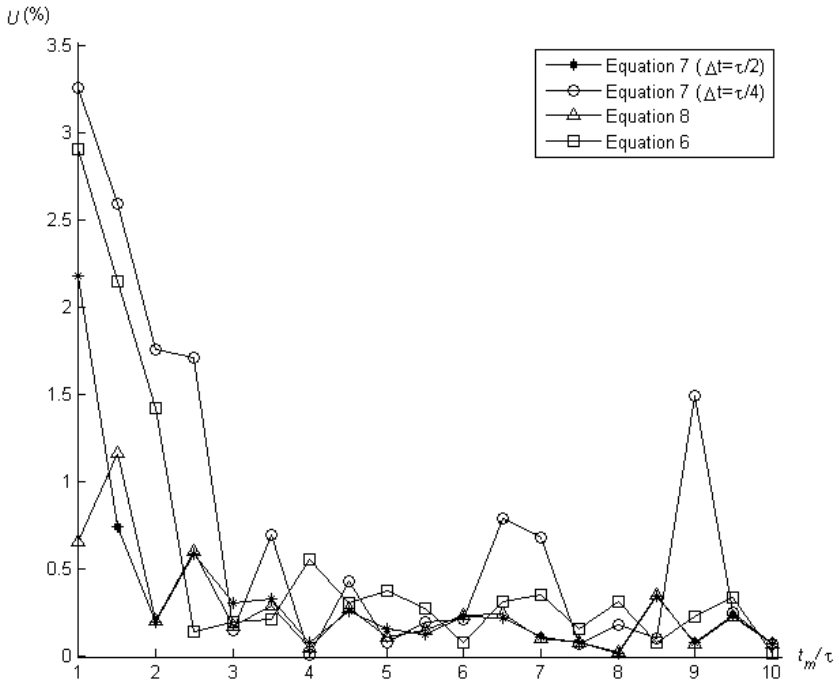

Figure 24: Error of the calculation depending on when the last sample (time measured t_m) was taken, using the different equations (10-bit systems)

τ (s)	Equation 4	Equation 5	Equation 7 ($\triangle t = \tau/2$)
1	2.5	2.7	2.5
10	2.2	2.7	2.5
100	2.1	2.7	2.6
300	2.0	2.5	2.3
600	2.0	2.6	2.3
1000	2.5	2.5	2.5

Table 14: Relation between t_m and τ for 8-bit systems

In this case, we would have to wait $4.5 \cdot \tau$ using the equations of Figure 21, and around $6.91 \cdot \tau$ using the generic Equation (2). Thus, the same result is obtained in 65 % of the time previously needed for 10-bit systems.

τ (s)	Equation 4	Equation 5	Equation 7 ($\triangle t = \tau/2$)
1	4.0	4.0	4.0
10	4.5	3.5	4.3
100	4.0	3.7	4.0
300	4.0	3.8	3.8
600	4.5	4.0	4.0
1000	4.3	3.8	4.3

Table 15: Relation between t_m and τ for 10-bit systems

Materials and method

The following experiment was set up to test the equations of Figure 21. We set up a first-order circuit supplied by the *Agilent* 33220A signal generator (internal resistance of 50 Ω) with a squared signal. The charge and discharge of the capacitor was obtained using an acquisition system and the data was analyzed.

The main interest is finding the final value of a first-order for situations where the system response is very slow. Thus, a high value of *R*, *C*, or both is necessary. But a high value of *R* can produce charge effects with the output impedance of the acquisition system. Furthermore, *C* cannot be much higher than 1 µF in order to avoid the use of an electrolytic capacitor. Therefore, the values chosen for *R* and *C* were 1 MΩ (1 % tolerance) and 1 µF (plastic package, 10 % tolerance), respectively, in order to theoretically have a delay of 1 s. We decided to simulate a high delay, although Table 14 and 15 show that the method does not depend on the delay.

Two tests were carried out, one acquired with an *Agilent Infiniium* MS08104A oscilloscope in order to emulate 8-bit systems, and one with an *Eagle* Data Acquisition (DAQ) *uDAQLite* for 10-bit systems.

In the test carried out with the oscilloscope, the voltage supplied by the signal generator was ± 2 V with a frequency of 50 mHz (in order to see $10 \cdot \tau$ of the charge and the discharge), and the data was acquired at a 5 kSamples/s rate. With a calibrated probe, the oscilloscope has a 10 MΩ internal resistance and a few pF of capacitance. Therefore, the delay will be 0.91 s, plus a certain uncertainty due to the uncertainty of the elements in the circuit.

In the test carried out with the DAQ, the voltage supplied by the signal generator was ± 5 V, with a frequency of 50 mHz, and the data was acquired at a 6 kSamples/s rate. The DAQ has a 2 MΩ

internal resistance and a negligible capacitance. Thus, the delay is a 0.67 s delay plus an uncertainty.

A charge and a discharge of the capacitor were acquired for each test and their *SNR* was measured. In the case of the oscilloscope, both the charge and the discharge had an *SNR* of 43 dB; for the DAQ, the charge had an *SNR* of 59 dB and the discharge had an *SNR* of 58 dB. The *SNR* was measured by taking a one standard deviation (1σ) of the noise in the signal and calculating it using Equation (8).

$$\mathrm{SNR} = 20 \cdot \log \frac{\Delta V}{\sigma} \quad (8)$$

where $\triangle V$ is the change ($V_{max} - V_{min}$) of voltage performed by the first-order.

Since we found different *SNR* levels in each signal, the worst values of each case were taken.

Experimental results and discussion

The equations of Figure 21 were applied to the charge and the discharge of both tests in order to see how good they are when calculating the V_f of a real signal.

In the case of the oscilloscope, the final value tends to 2.03 V for the charge and -2.03 V for the discharge. These values were calculated based on the mean of the last 10 % of samples, and the delay of both cases was 0.97 s.

Figure 25 and 26 show that Equation (4) appears to work better, as in the theoretical simulation. However, the Simulation shows that, over time, the use of Equation (4) or Equation (7) when $\triangle t = \tau/2$ is indifferent. Moreover, Equation (5) seems to behave worse than the other two.

In the case of the DAQ, the final value tends to 3.85 V for the charge and -2.96 V for the discharge. Again, these values were calculated according to the mean of the last 10 % of samples, and the delay of both cases was 0.71 s. These values are not just the result of an attenuation due to a voltage divider given the connection between the first-order circuit and the acquisition system, but also of an offset voltage addition introduced by the DAQ.

Figure 27 and 28 show that the difference is lower using the three equations than in the case of the oscilloscope, because the *SNR* is bigger.

Figure 28 had two samples of Equation (7), when $\Delta t = \tau/4$, that tended to infinite between $9{\cdot}\tau$ and $10{\cdot}\tau$. This is because the samples

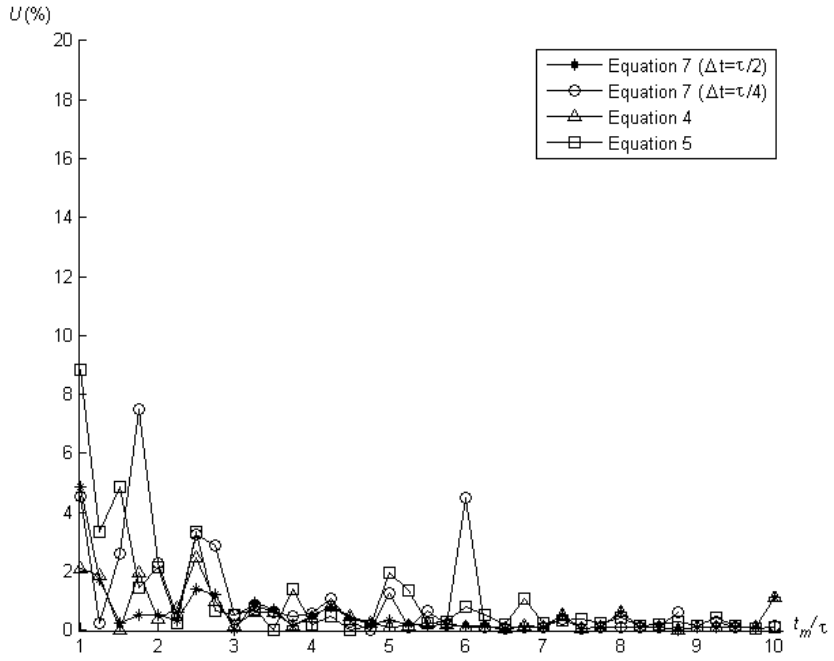

Figure 25: Error of the different equations applied to the charge acquired with the oscilloscope

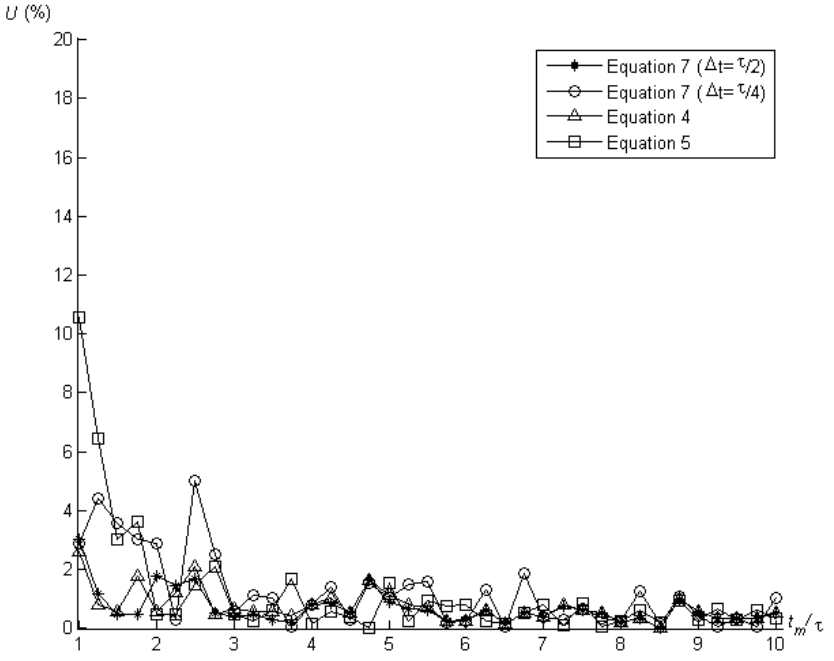

Figure 26: Error of the different equations applied to the discharge acquired with the oscilloscope

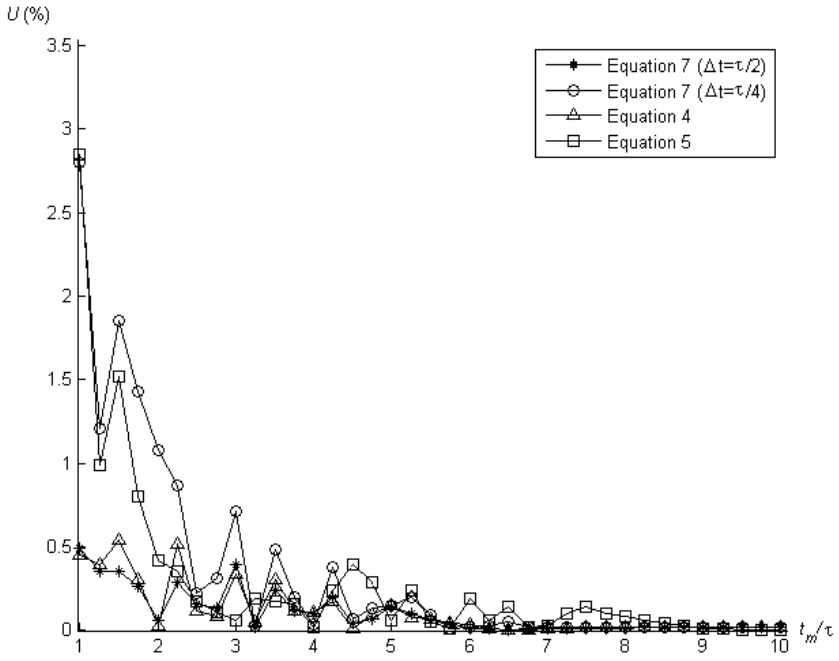

Figure 27: Error of the different equations applied to the charge acquired with the DAQ

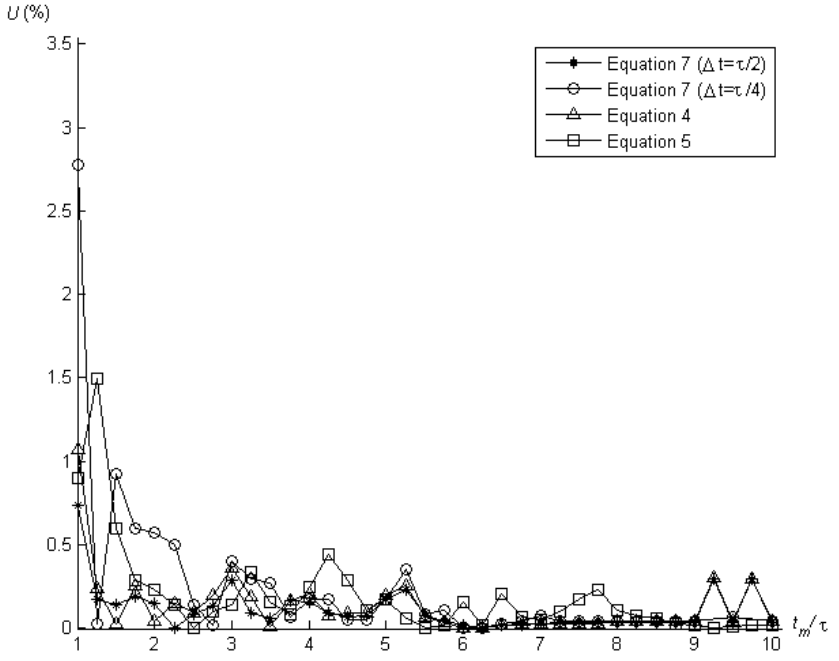

Figure 28: Error of the different equations applied to the discharge acquired with the DAQ

were taken very close, and at the end of a first-order system the amplitude of the samples barely varies; as shown in Equation (7), if the samples have a very similar value, the denominator tends to 0, and thus the result tends to infinite.

The error in Figure 25, 26, 27 and 28 has a similar distribution to that in Figure 23 and 24; thus, the error of the real application behaved like that of the simulation. The error was then quantified at certain times to see if there was any difference.

The maximal error was measured from a certain time to 10·τ (Table 16), which is pessimistic information as points can digress too much from the right value. Measurements were made of the standard deviation and the mean of the error of the same point and its 4 consecutive points (Table 17), which clarified whether there was a high digression. In the case of 8-bit systems (43 dB), we measured it from 2.5·τ, and in the case of 10-bit systems (58 and 59 dB) we measured it from 4.0·τ. These points correspond to the points described in Table 14 and 15 to find a full scale relative error (U) of 1 % and 0.1 %, respectively, for the simulation of the theoretical model.

SNR (dB)	*U* (%)			Characteristics
	Equation 4	Equation 5	Equation 7	
43	2.5 (2.6)	8.9 (10.1)	4.9 (3.6)	Charge, oscilloscope
43	2.6 (2.6)	10.6 (7.4)	3.0 (3.6)	Discharge, oscilloscope
58	0.5 (0.6)	2.9 (3.9)	0.5 (0.6)	Charge, DAQ
59	1.1 (1.2)	1.5 (3.0)	0.7 (0.9)	Discharge, DAQ

Table 16: Maximal error of the experimental and theoretical results from 2.5·τ (8-bit) and 4.0·τ (10-bit) to 10·τ (numbers between brackets in the table correspond to the application of the equations with theoretically generated data)

The cases are displayed in Table 16 and 17: a charge and a discharge for two *SNR* levels for each equation. The first shows that the higher the *SNR*, the lower the earlier U.

The charges and discharges were computably created with the same characteristics as the experimental ones (enumerated in Ma-

SNR (dB)	*U* (%)			Characteristics
	Equation 4 Mean, σ	Equation 5 Mean, σ	Equation 7 Mean, σ	
43	0.52, 0.25 (0.40, 0.25)	0.46, 0.53 (0.51, 0.27)	0.58, 0.29 (0.40, 0.20)	Charge, oscilloscope
43	0.66, 0.22 (0.66, 0.20)	0.61, 0.56 (0.53, 0.27)	0.51, 0.26 (0.52, 0.27)	Discharge, oscilloscope
58	0.08, 0.04 (0.09, 0.04)	0.14, 0.12 (0.08, 0.04)	0.07, 0.05 (0.08, 0.04)	Charge, DAQ
59	0.11, 0.10 (0.09, 0.04)	0.09, 0.07 (0.09, 0.06)	0.10, 0.08 (0.09, 0.04)	Discharge, DAQ

Table 17: Mean and standard deviation of the error of the experimental and theoretical results in $t_m = 2.5 \cdot \tau$ (8-bit) and $4.0 \cdot \tau$ (10-bit) and its 4 consecutive points (numbers between brackets in the table correspond to the application of the equations with theoretically generated data)

terials and method and at the beginning of this section) in order to compare results.

Table 16 shows that, as described for the graphs of the tests and the theoretical simulation, the Equation that has the worst *U* from these points to $10 \cdot \tau$ is (5). The theoretical simulation and the tests have similar results except for certain cases in which there might be an isolated disturbance that digresses a great deal from the right value.

Table 17 demonstrates that averaging all Equations have similar results. This means that Equation (5) causes certain high-error digressions, and that the remaining points are closer to the right value than they were in Equations (7) and (4), with averaging results on the same *U*.

Conclusions

A method for estimating the final value of a first-order system has been developed. The equations involved are simple expressions implementable on interfaces with a low computational capacity as a microcontroller. For 10-bit systems and in order to have an error lower than 0.1 %, this method allows the final value to be found in 65 % of the time required using the first-order system generic equation. For 8-bit systems, to have an error lower than 1 %, the final value can be found in 59 % of the time. Therefore the behavior of

the error in the calculation is lower earlier, and if we wish to reduce the possibility of having negative digressions on the error we can realize the mean of calculations taking the samples at consecutive moments.

The model can be used in our autonomous system to save processing time and thus decrease its overall consumption with a negligible error introduction.

2.5 CONCLUSIONS

We have designed a temperature system that autonomously measures temperature of compost from the inside of a capsule. The following conclusions have been extracted from the development:

1. We have compared two different conditioning methods: classic conditioning and a direct interface sensor-to-microcontroller. We found that the main consumer of the classic consumption is the excitation stage and that depending on that varying the resistances the consumption/resolution trade-off can be optimized. The direct interface method has proved to consume much less than the classic conditioning at the cost of some resolution. Still the resolution provided by the direct interface method is more than enoguh for most of temperature sensing applications.

2. We have studied different materials for the protection of the circuit and found that depending on the material the delay on the sensing of temeprature varies.

3. To counteract the delay in the temperature measuring we have developed an algorithm to estimate the final value of the delayed measure of temperature. In other words, while the outside temperature is being acquired by the whole body of the circuit protective material at the rate of a first order, our algorithm can estimate what the temperature is by taking some initial samples reducing the measuring time to 60 % of what it would take otherwise.

2.6 EXPERIMENTAL TESTS

2.6.1 *Lab tests*

Some lab tests were performed in order to see the uncertainty and the accuracy of the measuring system. Also, they served us to see the behavior of the system when measuring inside the polyurethane capsule.

The MCU of our temperature system was programmed with *IAR Embedded Workbench 4.21* in a mix of both C and assembler (the main program in C and the timer capture for the direct interface in assembler to have an exact timing). The performance of the MCU has been divided in two: the monitoring and the uploading of the recorded information.

For more information regarding the program implementation please refer to Appendix **??**.

Continuous measuring

This experiment consisted on the continuous measure of a controlled temperature provided by a HAR9102S temperature chamber, in order to see the accuracy and the precision introduced by our system. The circuit was supplied by a FAC-662B power supplier and the temperature range measured was from 20 to 70 °C with increments of 10 °C. For each temperature around 100 measures were taken.

In Table 18 we can see the standard deviation and the mean of the continuous measuring of each temperature. In terms of accuracy, the maximal error in the measure was of 0.31 °C and the mean error was 0.17 °C. Most of this error is systematical implying that it can be decreased by calibrating. In terms of precision we can see that the maximum standard deviation of the 6 measures is 0.25 °C.

If a two-point calibration is applied to the mean of the measures ($T_{cal} = T_{meas} \cdot 99.71 \cdot 10^{-2} - 5.6 \cdot 10^{-4}$) the maximal error in the measure results 0.19 °C.

As we can see our system fulfills the accuracy specifications even without calibrating as we were expecting from the use of a direct interface sensor-to-microcontroller conditioning.

Our system accuracy, though, is more than twice worse than our specifications. There are many possible reasons behind this fact, like the heating and cooling cycles of the climatic chamber or the precision of the components of the conditioning system. To solve it we can use high accuracy components which can significantly improve the accuracy performance. On the other hand, we can also

Chamber temperature (°C)	Circuit Maximal deviation (°C)	Circuit Mean (°C)	Calibrated Mean (°C)
20.0	0.05	20.06	20.00
30.0	0.13	30.15	30.06
40.0	0.25	40.19	40.07
50.0	0.19	50.18	50.03
60.0	0.04	60.20	60.03
70.0	0.15	70.21	70.00

Table 18: Continuous measure test results

average several samples in order to improve the accuracy as long as we agree with the increase in consumption it would imply.

Measure inside the capsule

The experiment consisted on the designed circuit measuring temperature inside the ball during 64 hours. The capsule was cut in half and emptied, leaving a cavity of the circuit volume. The circuit was programmed and subsequently inserted inside the ball, which finally was sealed with hot glue. Figure 29 shows the circuit inside the ball and a ball sealed with the circuit inside. In section 2.4.2, it was theoretically and experimentally seen that the bigger the width, the higher the transference time independently of the temperature change. Therefore, the temperature sensor was placed as close to the border of the capsule as long as it is protected against blows (0.6 cm).

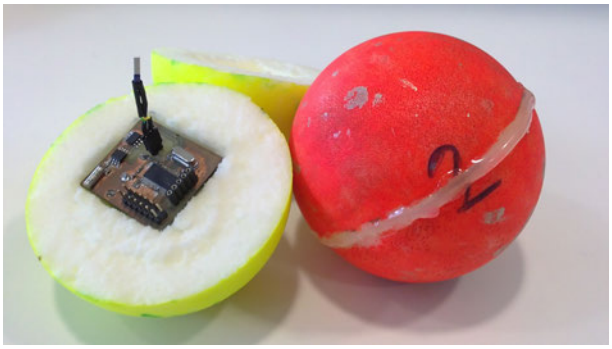

Figure 29: Circuit inserted into the High Bouncing balls

A measure was taken each 15 minutes. In parallel a *Delta Ohm* 9406 Thermometer Hygrometer probe was used as a reference measuring at the same rate and during the same time. The result of the test can be seen at Fig. 30. The maximum difference between the probe and

the circuit was less than 0.4 °C, which is the worst scenario in which the error of the circuit and the error in the probe are combined.

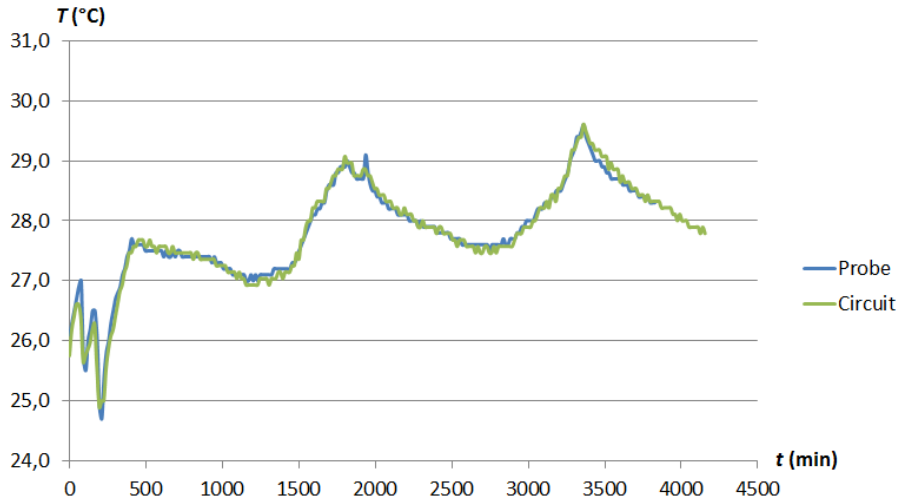

Figure 30: Measure inside the capsule of the answer to a temperature step.

Then the capsule was tested by introducing it from a temperature of around 21.5 ºC to a fridge at around 9 ºC. The system measured 1 sample per minute during half an hour to take part of the acquisition of the temperature. The result can be seen in Fig. 31.

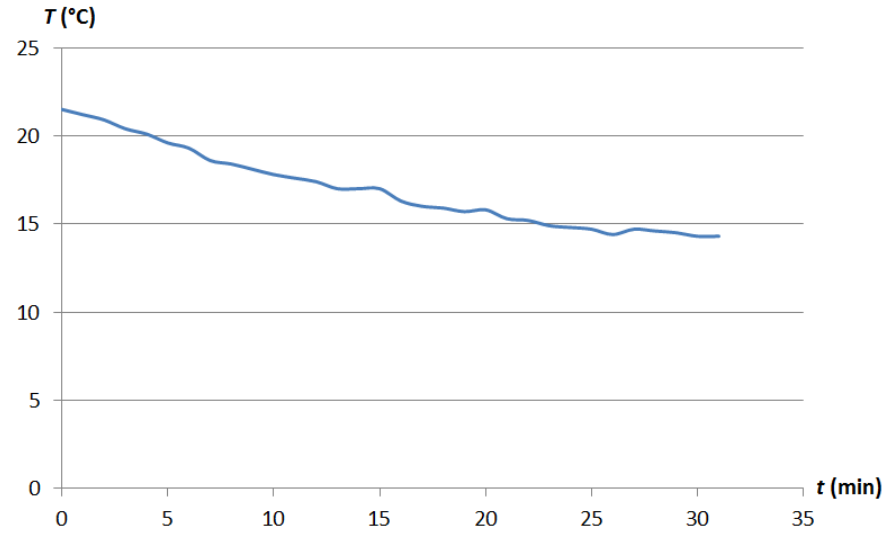

Figure 31: Measure inside the capsule (1 sample per measure)

If we apply the method for reducing response time (in this example with Equation (4)) in sensor measurement we could safe measuring time by using equation 2.36. As we can see in Figure 32, the tendence is that the later we apply the method the less uncertainty. More

experimental data points and a longer measure time would be needed to see the whole development of the uncertainty.

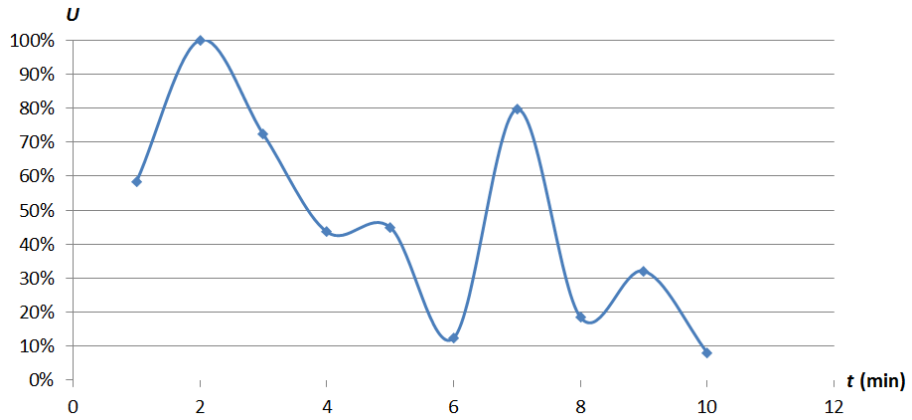

Figure 32: Uncertainty of applying the method to the experimental data

Measure inside ground

The experiment consisted on the designed circuit measuring temperature inside the ball and at the same time inside a pot filled with ground, with the dimensions shown in Fig. 33, in order to simulate the conditions of the composting material.

Figure 33: Pot measures distribution

The experiment lasted around 7 hours and the measuring rate was one sample each 15 minutes.

The Thermometer Hygrometer was inserted in the pot as a reference measuring at the same rate half an hour later when the circuit would have acquired the same temperature as the pot and until the same time.

As can be seen in the results of Fig. 34, the circuit has a minimal error compared to the measure of the probe. The maximum difference

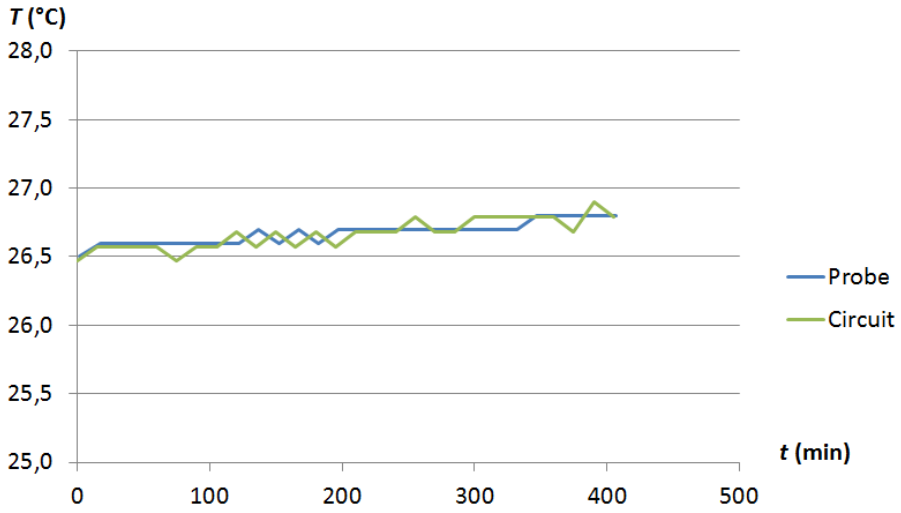

Figure 34: Results of measuring inside ground

between the measure of the circuit and the measure of the probe was 0.13°C.

2.6.2 *Field tests*

Some field test measures are needed in order to check the proper operation of our system inside the capsule and within the real environmental conditions.

Measure on pile

The experiment consisted on the designed circuit measuring temperature inside the ball and at the same time inside a pile of compost in the curing stage located at the *Parc Mediterrani de la Tecnologia* (PMT) (Fig. 35).In parallel the Thermometer Hygrometer was inserted in the pile as a reference measuring at the same rate.

Figure 35: Pile in maturing stage

The circuit was introduced into the pile 3 hours before the probe, in order for the circuit to reach the temperature of the pile and avoid observing the delay in the answer. The probe measured during 20 min and both of them measured at a 1 sample per minute rate.

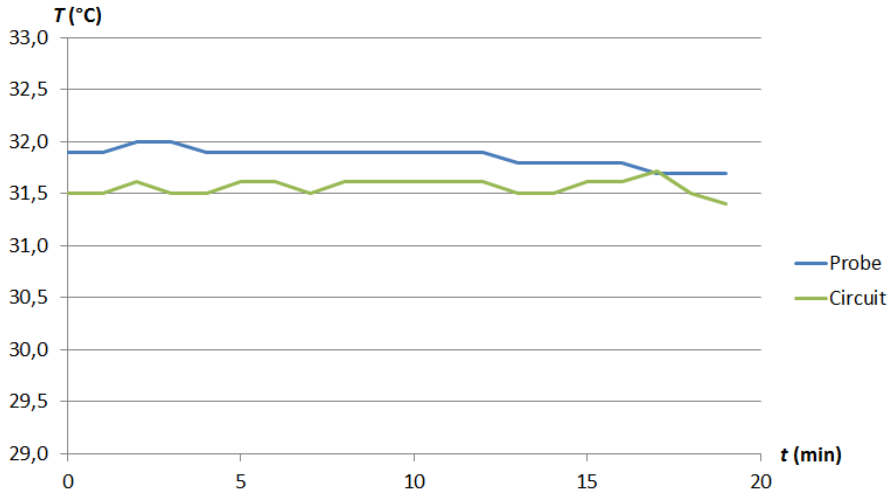

Figure 36: Result of the second test inside the compost pile

As we can see in Fig. 36, the temperature of the pile has been acquired by the circuit and is measuring as if it were outside in the air. Similar to previous results, the maximum difference between the circuit and the reference is less than 0.5 °C. We can see that there is a difference in the measure of the circuit and the probe, this difference that seems as if they were measuring different temperatures comes mainly for the position difference between the probe and the circuit. In field tests during the compo-ball project was later showed that slight differences in the position implied great changes in the measure (e.g. half a meter may imply more than 10 degrees change).

Measure on composter

A similar experiment was realized but in a composter (Fig. 37) during the initial stage of the composting process. The circuit was buried inside the compost and a *Crison* Temperature probe was placed next to it. Both the probe and the circuit were measuring at a 1 sample each 5 min rate during 30 min.

In Fig. 38 we can see the temperature evolution measured by the probe and the circuit. As we can see there is a delay error in the measure of the circuit. One could think that if the answer of the composting pile in front of our system was a ramp our system would not be able to reach the right measure ever. That is correct, but as said in at the beginning of this chapter, changes of temperature

Figure 37: Composter

during the composting process are really slow, and hence our system would be able to follow these changes with a smaller error. In this case, the change of temperature in 30 minutes is of 0.8°C and the maximum error between probe and circuit is of 0.3°C.

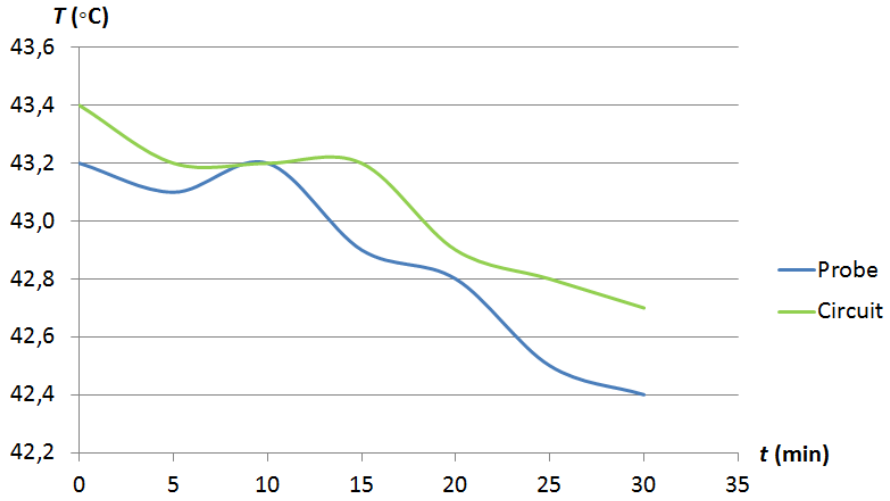

Figure 38: Test inside the composter

Also we can see that the maximum delay in the measure is of 7 minutes. The sensor was placed 3 mm inside the ball, and the ball was a foam polyurethane ball, around 100 g and a 12 cm diameter. Theoretically, with this data the delay suffered by a measure should be of 8.62 min. The reason why our measure is better is because the model is not completely uniform and the sensor is not between two equal masses and volumes, the delay decreases since its nearer from the heat focus due to the heat-transfer principles.

Measure with 4 reference probes

The placement of the reference probe with which we compare our sensors can provoke a great variation in the measure. To show this behavior four probes were attached around one of the sensors with a 90 ° separation (Figure 39). The measure was realized at Happs' plant (Netherlands) by the Compoball project team.

Figure 39: Our sensor with four probes attached to its surface with a 90 °

In Table 19 we can see that the maximum difference between probes is 2 °C and the maximum difference between our sensor and the probes is 1.2 °C. This way we can see how the measure of the probe can have affected to the comparisons realized in the previous tests.

Sensor T (°C)	Probes T (°C)	Mean T (°C)	Max. difference between probes T (°C)
42.7	41.9, 41.9, 42.4, 43.9	42.3	2

Table 19: Experimental measures with our sensor and four probes attached to its surface

Long measure on pile

During the development of the Compoball project a test was realized at Manresa's Composting plant with a system measuring during almost 2 months inside of a pile (from November the 27th to January the 22nd). In Fig. 40 we can see the results obtained from the tests.

As we can see, the temperature measure starts with high values during the decomposition stage and slowly decreases to lower values where it stabilizes during the curing stage. The evolution in

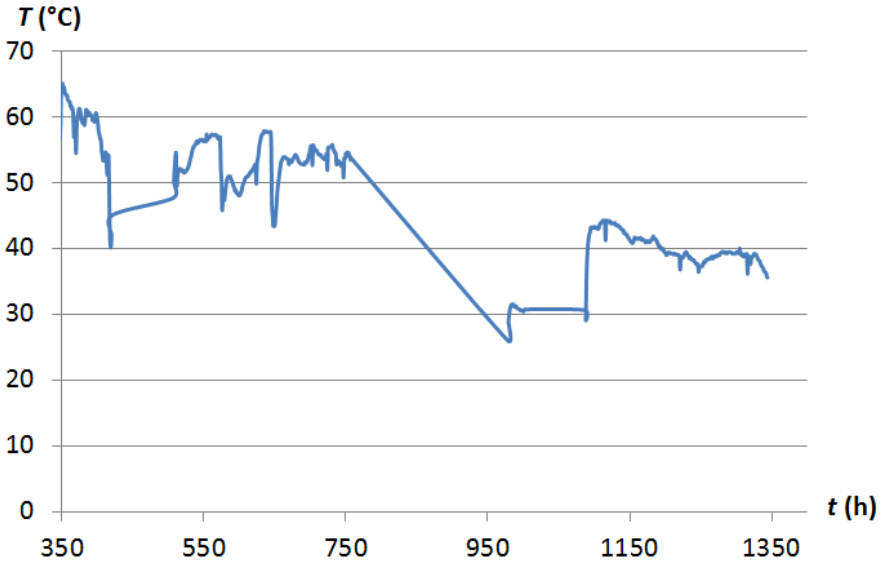

Figure 40: Test inside pile for two months

temperature was not continuous as there were moments in which the compost was turned over to aerate it, and as such the sensors were moved in position. At some points the sensors were moved so far away (or outside of the pile) that the data communication was impossible.

I am not young enough to know everything.

— Oscar Wilde, dramatist

3 COMMUNICATION SYSTEM

3.1 STATE OF THE ART AND PROPOSED SOLUTION

In order to interact from the outside of the compost with the sensor systems or between them, we will need a data communication system. There are not known studies related to the transmission inside compost and thus this feature becomes critical and innovative.

Compost is well known for being a very heterogeneous material [72] which can be mainly divided into water, organic matter and air. In terms of wave propagation the attenuation that a transmitted signal has when going through a material is very big on water particles [73], smaller on organic matter (similar to underground [74]) and much smaller on air (Figure 41). Therefore, the more humidity or density in the material the more attenuation will affect a transmission.

As stated in the first chapter, humidity decreases and density increases along the composting process (Fig. 44). During the decomposition stage humidity levels are in its highest levels (up to 80 % and typically between 50 and 60 % [5]) and, as time goes by, it gradually decreases until its lowest levels in the curing stage (Figure 42). Density, on the other hand, behaves the other way around

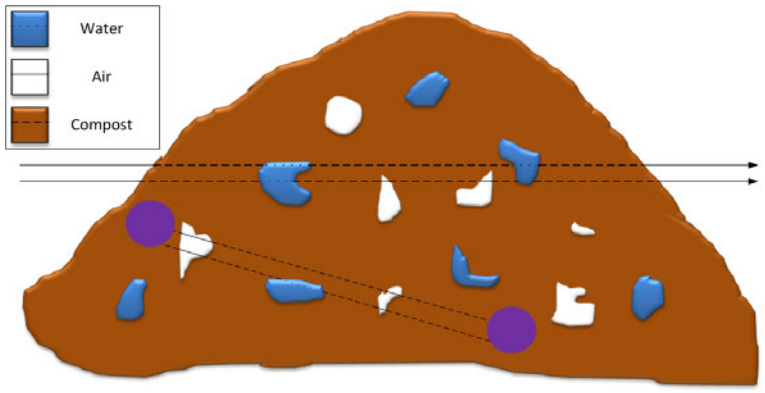

Figure 41: Theoretical transmission through compost

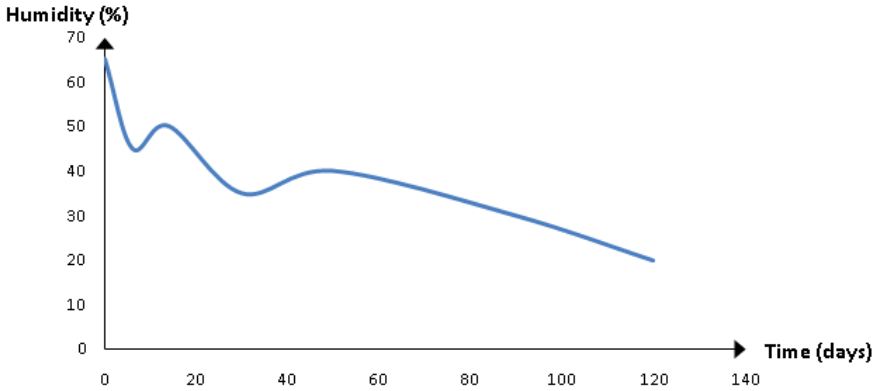

Figure 42: Humidity evolution (extracted from [3])

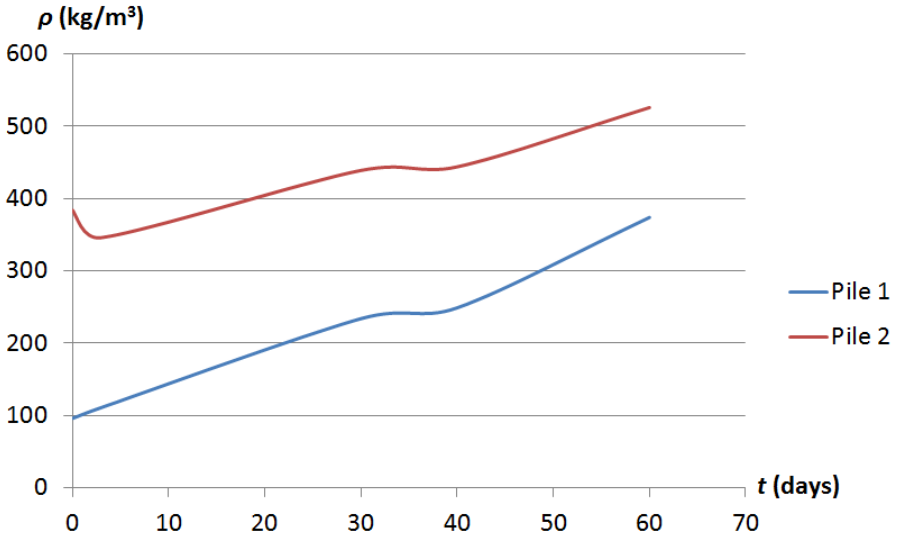

Figure 43: Density evolution (extracted from Table 3.2 from [75])

(Figure 43); it starts with a very low compost density from the decomposition stage (over 100 kg/m^3) and ends up with a high value of density during the curing stage (typically over 500 kg/m^3 and with maximum values of 800 kg/m^3) [75]. Changes on humidity and density affect the value of the material relative permittivity [76], and as such, they affect the performance on communications. When humidity increases, the communications get worse and the same for density. Hence, if we take a look at the qualitative reprsentation from Fig. 44 we see that the behavior of communications in compost will more or less behave the same during the whole process, since this two magnitudes compensate each other.

As such, compost in the earlier stages has a high level of water, and the extreme environment for transmission would be underwater [77] (as used for submarines). On the other hand, compost in the final

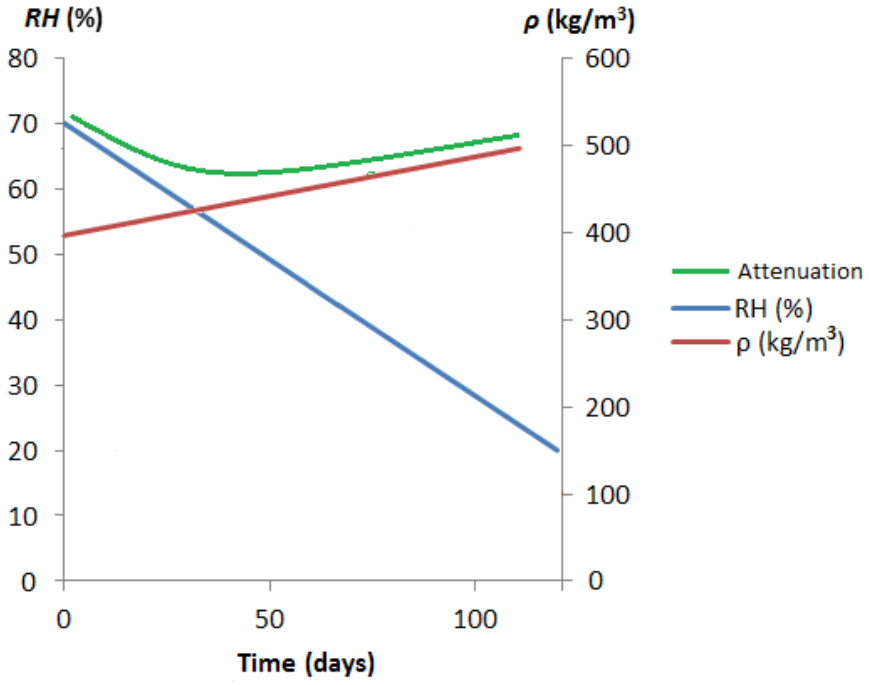

Figure 44: Qualitative evolution of humidity and density during the composting process

stages has a low level of water and a very high density with a relative permittivity similar to soil, and hence, its transmission is similar to underground [78] (as used for the communication in mines[79]). The whole process, though, implies a variation of the characteristics of the transmission environment, as such, the transmission in compost can be seen analogue as the transmission in grain [80].

Sonar waves are the most extended transmission method for the underwater acoustic channel, that is characterized by a path loss that depends not only on the transmission distance, but also on the signal frequency [81]. This method, though, is very complex and very expensive to apply. However, it shows us that an environment with a very high level of water content would rely on lower frequencies for transmission and that is what one could expect for the earlier stages of compost.

There are studies that show that the heterogeneous composition of the underground medium requires a very good characterization for a proper deployment of underground wireless devices [78]. Moreover, those studies specify the frequency range of 150 to 900 MHz to take under consideration when characterizing the underground medium [79]. Still, ground has very similar properties as compost in the final stages and as such it can be seen as a reference for the transmission model.

On the other hand, compost can be compared to grain due to their similar heterogeneity and very similar relative permittivity (as we will find in the following chapter compost has a relative permittivity from 4 to 13 depending on the stage of compost and grain has a relative permittivity from 3 to 12 depending on the type of grain), we also should refer to its examples to look for the proper transmission method. Studies in grain monitoring with wireless transmission have shown that the most effective transmission is the RF band and more specifically the 433.05 - 434.79 MHz free frequency band [82, 83]. Studies of RF transmission in grain indicate that the maximum distance can be up to 10 m transmitting at 30 dBm and 500 MHz[84] (which would be an acceptable distance for transmission in compost). Another study, worked with a much higher frequency band (around 915 MHz) transmitting at 0 dBm. In this case the maximum transmission distance was reduced to 1.1 m [85].

Therefore, we see that transmission seems possible on compost for proper values of power, frequency band and distance. To determine the behavior of compost for wireless communications, an experimental characterization of the compost as a transmission environment will be realized. Simulations are not used in this characterizations since compost is a very heterogeneous material which makes it impossible to model and also, due to the unknown distance between transmitter and receiver.

In the following chapter we will look for the free frequency bands in which communications are possible and in which commercial devices are available. We will describe the communication system and its commercial devices. Finally, some tests with the commercial devices will be realized to try to theoretically model the transmission in compost in function of a distance between 1 and 10 meters (acceptable distance range for the length of a typical compost pile).

3.1.1 *Theoretical model*

The attenuation theoretical model for different transmission environments can be as simple as Coulomb's law for the magnitude of the electric field (E) created by a single point charge (q) at a certain distance (d) in the free space [86]:

$$E = \frac{1}{4\pi\varepsilon_0}\frac{q}{d^2} \tag{3.1}$$

or the simplified formula for the path loss (L) in the air for RF transmission [13]

$$L\,(\mathrm{dB}) = 20\log\left(\frac{4\pi d}{\lambda}\right) \tag{3.2}$$

where d is the distance the wave travels and λ is the wavelength.

or even as complex as the Okumura-Hata wireless communication model for predicting the behavior of cellular transmissions in urban areas. There, the path loss is

$$\begin{aligned} L_U\,(\mathrm{dB}) = 69.55 + 26.16\log(f) - 13.82\log(h_B) - C_H + \\ + [44.9 - 6.55\log(h_B)]\log(d) \end{aligned} \tag{3.3}$$

where f is the transmission frequency in MHz, h_B is the height of the base station antenna, C_H is the antenna height correction factor (also known as antenna factor) and d is the distance between the base and mobile stations in km. As we can see, the higher the frequency the higher the attenuation of the environment.

In the case of small or medium sized cities

$$C_H = 0.8 + (1.1\log(f) - 0.7)\,h_M - 1.56\log(f) \tag{3.4}$$

and for large cities

$$C_H = \begin{cases} 8.29\,(\log(1.54h_M))^2 - 1.1, \text{ if } 150 \leqslant f \leqslant 200 \\ 3.2\,(\log(11.75h_M))^2 - 4.97, \text{ if } 200 < f \leqslant 1500 \end{cases} \tag{3.5}$$

where h_M is the height of the mobile station antenna.

This last model is suited for both point-to-point and broadcast transmissions in urban areas and it is based on extensive empirical measurements taken, and as such, it is very complex to apply to our case because the size of the antennas is really small. This implies that, according to this model (Equation 3.3) and considering an antenna of 1 m, our wave would attenuate at a minimum rate of $1/d^{4.49}$ approximately and would attenuate more for smaller antennas ($1/d^{[4.49-0.655\log(h_B)]}$).

We stated that one of the most analogue studied material to transmission inside compost is grain together with ground. Hence, we would expect compost to have a similar attenuation theoretical

model and similar relative permittivity (around 12). According to [80] the attenuation theoretical model for transmission inside grain is

$$P = P_t e^{-2d,} \tag{3.6}$$

where P is the received power, P_t is the transmitted power, d is the distance in the direction of travel and α is the attenuation constant that can be expressed in nepers/m and in terms of dielectric properties as [87]

$$\alpha = \frac{2\pi}{\lambda_o}\sqrt{\frac{\varepsilon'}{2}\left(\sqrt{1+\tan^2 d}-1\right)} \tag{3.7}$$

where λ_o is the free-space wavelength (a value used as a reference to compensate), ε' is the dielectric constant (function of the frequency) and $\tan\delta$ is the loss tangent often used as an index of energy dissipation or loss in a material exposed to RF or microwave fields.

As we can see, the higher the frequency or the relative permittivity, the higher the attenuation.

Attenuation, though, is often expressed in decibels/m. In terms of power densities and electric field intensity values, this can be expressed as

$$10\log\left[\frac{P_o}{P(z)}\right] = 20\log\left[\frac{E_o}{E(z)}\right] = 8.686,z \tag{3.8}$$

where P_o is the power at a point of reference, $P(z)$is the power in function of the distance, E_o is the electric field intensity at a point of reference and $E(z)$ is the electric field intensity in function of the distance.

The attenuation in decibels, combining equations 3.7 and 3.8, can be expressed in terms of the dielectric properties as follows

$$\alpha \cong \frac{8.686\pi\varepsilon''}{\lambda_o\sqrt{\varepsilon'}} \tag{3.9}$$

only when $(\varepsilon'')^2 \ll (\varepsilon')^2$, where ε'' is the dielectric loss factor.

In conclusion, there is no communication model in the inside of compost nor an optimum transmission frequency. Approximately,

air attenuates at a $1/d^2$ rate, grain attenuates at $e^{-,d}$, and in a city at $1/d^{4.49}$. There is a need for frequential characterization measures for compost which would be used to select the frequency and adjust the behavior to one of the previous models.

3.2 COMPOST CHARACTERIZATION AS A TRANSMISSION ENVIRONMENT

3.2.1 *Method*

The characterization of compost as a transmission environment was realized with a very simple method (Fig. 45). We transmitted through compost and measured the receiving signal spectrum from 10 MHz to 500 MHz (as stated in the case of grain in the state of the art at 500 MHz we can transmit until 10 m, with lower frequencies we are supposed to transmit farther). With the same setup and configuration, we did the same in the open air. We compared those two results to know what the attenuation is due to compost.

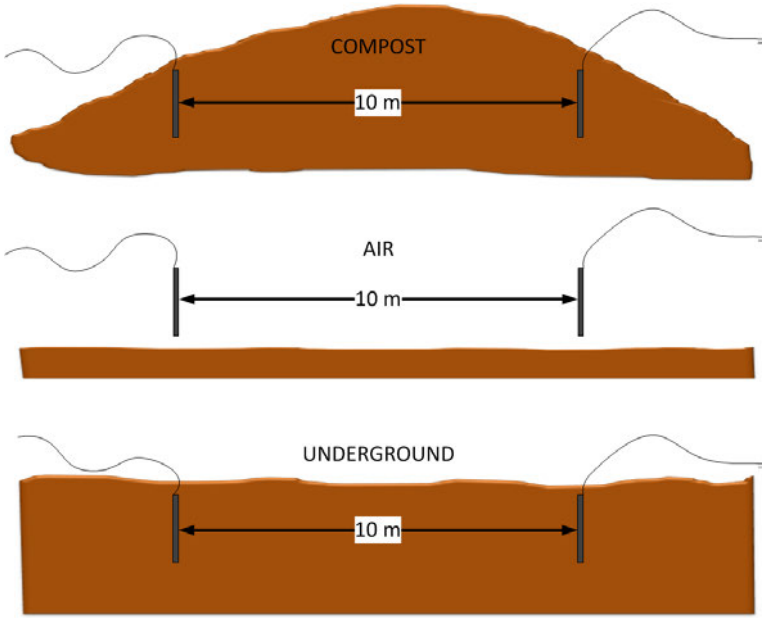

Figure 45: Characterization method

Furthermore, we also measured the transmission underground. Grain is more difficult to obtain and soil is an environment analogue to compost in the curing stage. As stated in the first chapter, transmission through compost should have the same characteristics as underground communications and comparing the two results we can somewhat validate them.

3.2.2 *Experimental setup*

The experimental setup (Fig. 46) consisted of two 490 MHz rod antennas buried into a compost pile, separated by ten meters (the maximum transmitting distance at 500 MHz). The transmitting antenna

was connected to an *Amplifier Research* 10W1000C gain amplifier, which, in turn, is connected to a *Hameg* HM 8133-2 signal generator. The receiving antenna was connected to a *Rohde & Schwarz* FSH3 spectrum analyzer measuring signal power level from 10 to 500 MHz.

Figure 46: Experimental setup. (left) Signal generator and gain amplifier. (right) Spectrum analyzer.

The spectrum analyzer was configured to measure the maximum signal level and the signal generator realized a frequency sweep from 10 to 500 MHz with a transmitting power P_1.

The power received by the spectrum analyzer depends on the gain distribution over the experimental setup. In Fig. 47 you can see the propagation of the power since the generation of the signal until its reception.

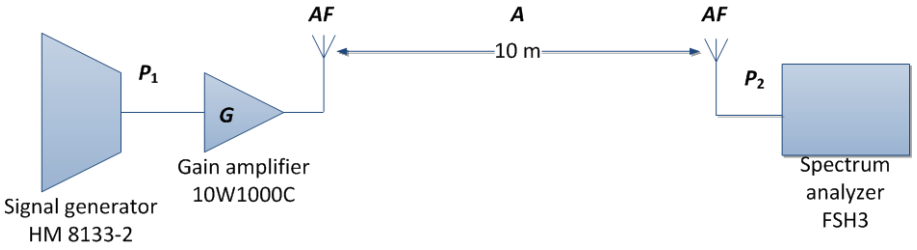

Figure 47: Power propagation model

Hence, the power received (P_2) is defined as

$$P_2(f)(dB) = P_1(dB) + G(dB) + AF(f)(dB) + A(f)(dB) + AF(dB) \tag{3.10}$$

where G is the gain of the amplifier, AF is the antenna factor, and A is the attenuation of the signal when being transmitted through an environment which is frequency dependent. As we can see the

models shown in the theoretical model section, correspond to the same variables shown in this generic equation.

The gain amplifier allows adjusting the gain level, but the exact amount of gain is not specified. The gain level used in all the experimental tests was characterized by some fellow members of the European project. The input of the gain amplifier was connected to a signal generator and the output was connected to the spectrum analyzer. With a frequency sweep from the generator and the analyzer measuring the maximum signal level the gain shown in Fig. 48 was obtained.

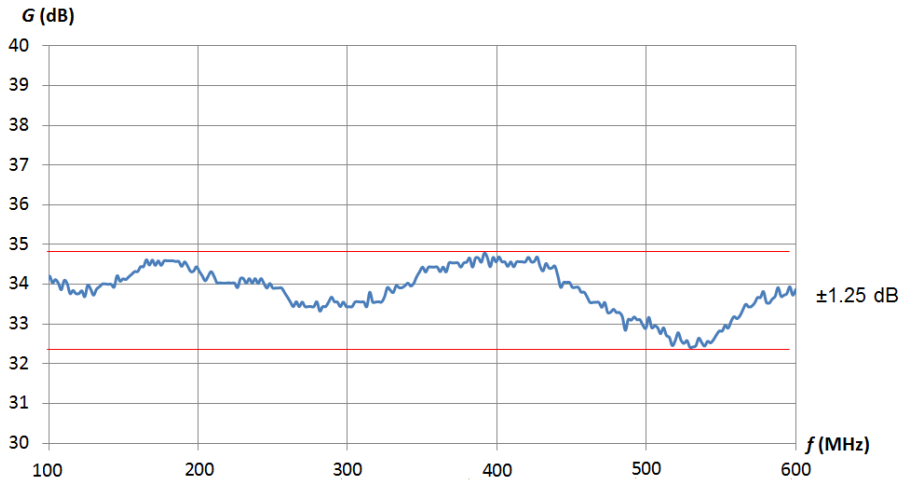

Figure 48: Gain characterization

As it is possible to see, the gain level oscillates around 34 dB with a frequency response of around ±1.25 dB from 10 MHz to 600 MHz.

The antenna factor can be measured with the input reflection from the scattering parameters (aka S_{11}) using a *Rohde and Schwarz* ZVL Network Analyzer.

As can be seen in Fig. 49, the antenna factor of the antenna in air is around its design frequency (490 MHz), but when the antenna is buried underground there is a slight detuning that displaces the frequency to around 480 MHz and its reflexion decreases to almost -18 dB. In the case of compost, the antenna factor main frequency is displaced even more to a frequency of around 440 MHz but its reflexion level is around -11 dB. As we can see, introducing an antenna with a design frequency characterized for the air implies a displacement in the design frequency when using the antenna on other environments. This includes the antenna mismatch effect due to the effect of the protective material, that is why, when designing an antenna with a protective material, a compensation network must be taken into account to counteract this effect.

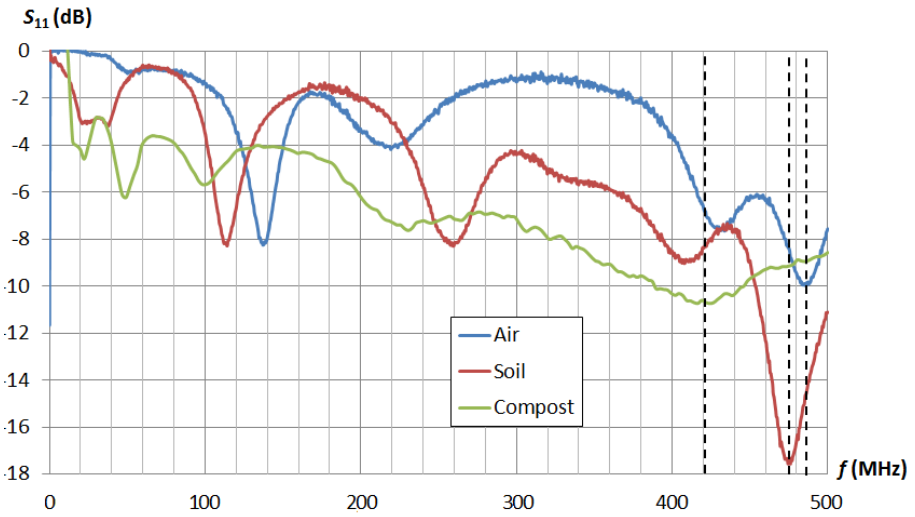

Figure 49: Dipole antenna factor characterization

In order to see how trustful those results are, the repeatability in the antenna factor measurement was analyzed. The S_{11} parameter was measured with the Network Analyzer for compost and air for two cases in which one day we measured in a pile from Barcelona and another day in a pile from the city of Sitges.

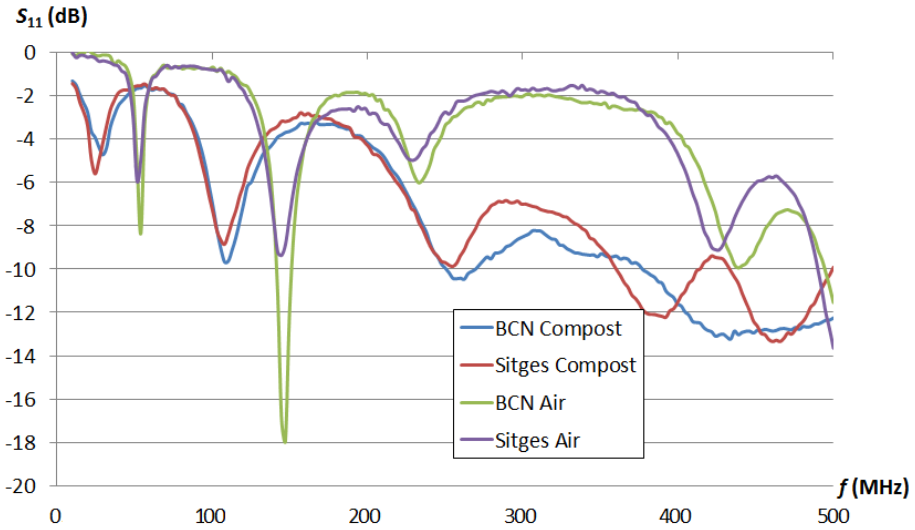

Figure 50: Dipole antenna factor repeatability

As we can see in Fig. 50, the repeatability of the antenna factor measurement in air is good (maximum 3 dB difference) but with a slight displacement in the main antenna frequency respect to that in Fig. 49. Also, there is an isolated peak in a frequency around 150 MHz which always more or less appears. The repeatability in compost is slightly worse than air with isolated peaks.

The antenna factor in compost has different repeatability when comparing Fig. 49 and 50. In Fig. 49 we have an antenna factor of -11 dBs at 440 MHz and -9 at 480 MHz and in Fig. 50 we have -13 dB at 440 MHz and -12.5 dB at 480 MHz in Sitges and -9.5 dB at 440 MHz and -13 dB at 480 MHz in Barcelona. Since we cannot directly subtract the antenna factor from the received signal due to its not perfect repeatability, we will have to take it into account qualitatively when analyzing the results of the test for each environment.

Therefore, since the gain and the antenna factor can be considered in our configuration, the attenuation of the signal when transmitted can be estimated.

3.2.3 *Results*

The captures realized by the spectrum analyzer in the cases of compost and air were compared in Fig. 51. The power of the signal generated was $P_1 = 0$ dBm (the typical power transmission for free-band ISM transmission systems). As can be seen, there is an attenuation of around 20 dB for a 10 m distance when transmitting through compost respect to transmitting through air (it can be seen clearer if we take a look at the 434 MHz band). That was expected since compost has a higher relative permittivity ($\varepsilon_r = [4, 13]$) than air ($\varepsilon_r = 1$) and, as such, it reflects more power.

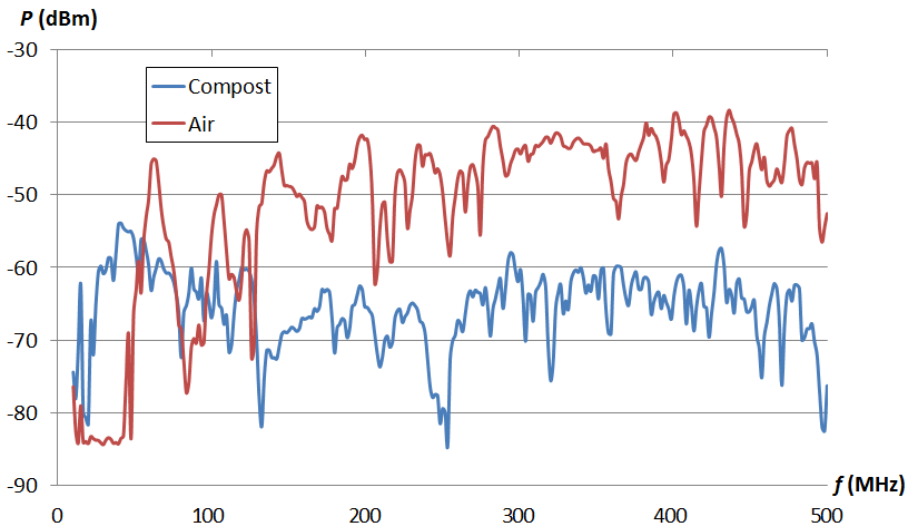

Figure 51: Air-compost comparison

We can see that at the lowest levels compost remains at around the same level and air dramatically drops, the reason behind this may be due to a coupling effect of the antennas. Since our equipment is connected to ground there may appear some parasitic capacitances.

Besides, the wavelength is lower the lower the frequency and we are not working at far field.

One could also think of a positive effect of the antenna factor at low frequencies, but we have already determined that this does not happen. Finally, it is possible that, due to been a good conductor, the transmission model of compost favors low frequencies.

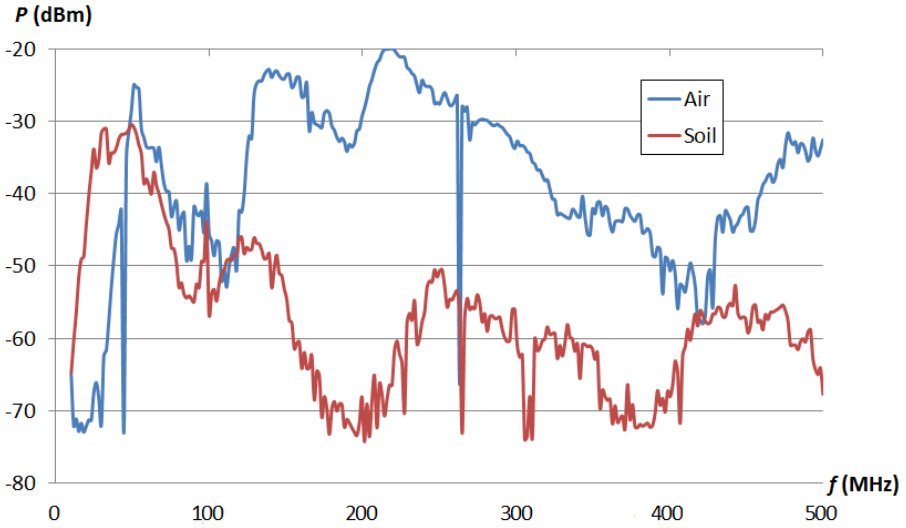

Figure 52: Air-soil comparison

In a similar way, we can see in Fig. 52 how the signal is attenuated more in soil than in air. It is more difficult to see a constant difference but the level of the signal in soil is most of the time under the level of the signal in air. As before, the level of the signal in the air at low frequencies drops for the same reason.

In general we see from Figures 51 and 52 that the power ranges received for each environment approximate to $P_{r,air} = [-25, -60]$ dB for air, $P_{r,soil} = [-35, -70]$ dB for soil, and $P_{r,compost} = [-40, -75]$ dB for compost. As can be seen, compost and soil attenuate more than air, as one could normally think. On the other hand, compost attenuates more than soil, probably for the high humidity content of the mixture. We can say at this moment that compost is valid as a transmission environment since its power can be received over 80 dB on some frequency bands for these specific conditions (distance 10 m, power transmitted 0 dBm and antenna factor centered around 433 MHz) as it is in soil. It is important to say that the repeatability of air comparing these two figures is pretty bad, this is mainly due to the extreme different conditions in the measure. These measures were taken in different days, locations and times, and some other conditions like equipment and position may have affected as well because otherwise the difference would not have been that high.

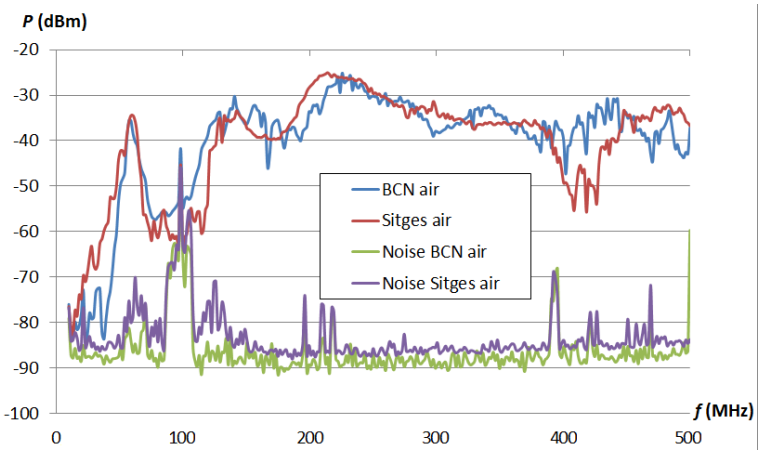

(a)

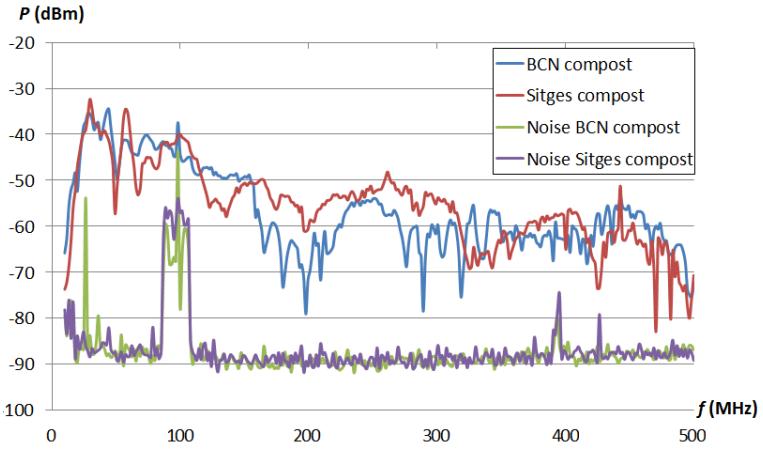

(b)

Figure 53: Signal and noise repeatability. (a) Air. (b) Compost.

If, as in the antenna factor, we measure the power of the signal transmitted through air and compost in two different times and places, we can determine the repeatability on the tests. Again, the locations for the two tests where one day a compost pile from Barcelona (BCN) and another day in a pile from the city of Sitges.

As can be seen in Fig. 53a and 53b, the repeatability of the measure in compost and in air is very good, with a maximum difference of 18 dB in compost and 16 dB in air, and an average difference of 6 dB and 5 dB respectively. On the other hand, it seems that transmission in compost is more feasible at low frequencies, since the level of the signal increases over the noise, as expected. The level gradually drops until around 460 MHz where it starts dropping dramatically, as such we ascertain that the proper free band to transmit at the highest frequency is the 433-434 MHz band, under our conditions.

3.3 EXPERIMENTAL TESTS

It was difficult to find commercial solutions allowing autonomous transmission systems at low frequencies in the past. However, in 2010, *Texas Instruments* brought out to the market an ultra-low-power microcontroller system-on-chip with integrated RF transceiver from the CC430 family, that adjusted better to our system due to the experience of using the same kind of microcontrollers for the first temperature system. Concretely, the CC430F6137 MCU allowed transmitting in the 300 MHz to 348 MHz, 389 MHz to 464 MHz, and 779 MHz to 928 MHz frequency bands.

When deciding which frequency band to use we see that according to the CEPT/ERC Recommendation [88], the free frequency bands at which we can transmit are the UN-32 ISM applications at 433 MHz, the UN-110 PMR 446 MHz and the UN-39 868-870 MHz band. As said before, we have tested the feasibility of transmitting under 460 MHz, and thus we cannot rely on the 800 MHz band. On the other hand, the PMR 446 MHz band corresponds to the Personal Mobile Radio band which is a very restrictive band (in terms of specifications) and is only license free in some countries of Europe. Hence, the band we will be using will be the UN-32 for ISM applications at 433 MHz.

When looking for 433 MHz antennas we looked for solutions able to be fit into the polyurethane capsule our system will be protected by. We also considered the best quality/prize, and a such we found the *Rain Sun* AN1603-433 Multilayer Chip Antenna.

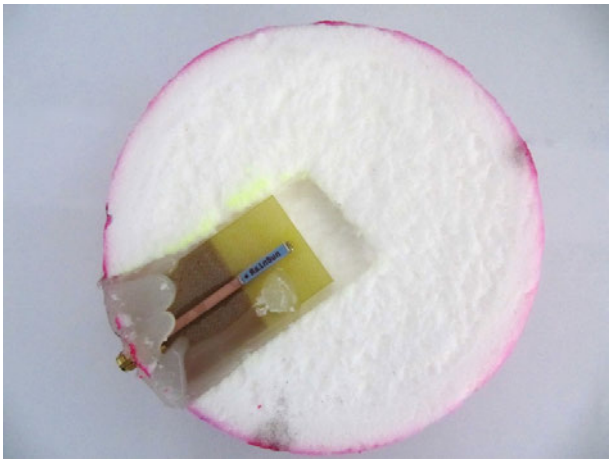

Figure 54: Antenna inside ball before closing

In the following experimental test we determined the distance until which the antenna could transmit inside compost. Also, with this test, we can determine the transmission model in air and in

compost. In this test the antennas were buried on a compost pile in the curing stage located in the *Parc Mediterrani de la Tecnologia* (PMT).

Two antennas were sealed inside a polyurethane ball (Fig. 54) to act one as transmitter and the other as receiver.

As in the previous section, we characterized the antenna factor of the AN1603 antenna to verify the goodness in its tuning. As we can see in Fig. 55, the antenna factor main frequency centers very precisely with $S_{11} = -14.4$ dB at 427 MHz in air. This antenna was supposed to be designed to transmit at 433 MHz, the change in frequency is due to a detuning due to the polyurethane protection, as we introduced in the previous section. In compost the main frequency slightly displaces to a frequency around 434 MHz with $S_{11} = -14.2$ dB and attenuates a little bit. We verified the repeatability of this measure by characterizing both antennas, as we can see the maximum difference in air was 3 dBs and in compost 2 dBs. This arises the need of a matching circuit to overcome the detuning caused by the environment.

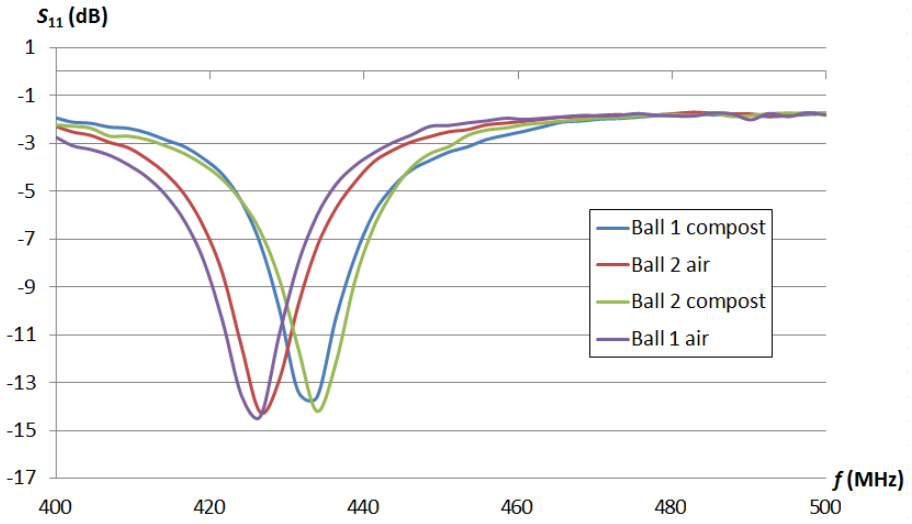

Figure 55: Antenna factor characterization

In the test, a 433 MHz signal was generated with the signal generator with a power $P_1 = 0$ dBm and transmitted with the antenna. The signal was transmitted through the air on one test and through compost on another and received with the other antenna connected to the spectrum analyzer. This test was realized modifying the distance between the antennas; from 2 m to 45 m in the air, and from 2 to 10 m in compost (similar to the grain works found in the state of the art). Compost in this test was in the curing stage but we would expect the same result in the decomposition stage, since the water

bags that are present are compensated by the air bags that are not present in the curing stage.

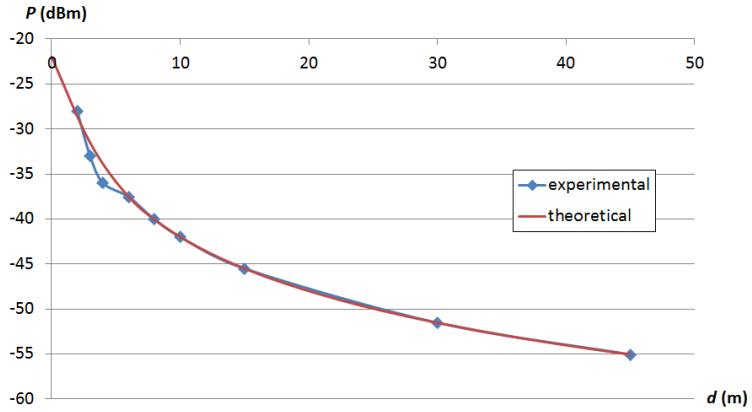

(a)

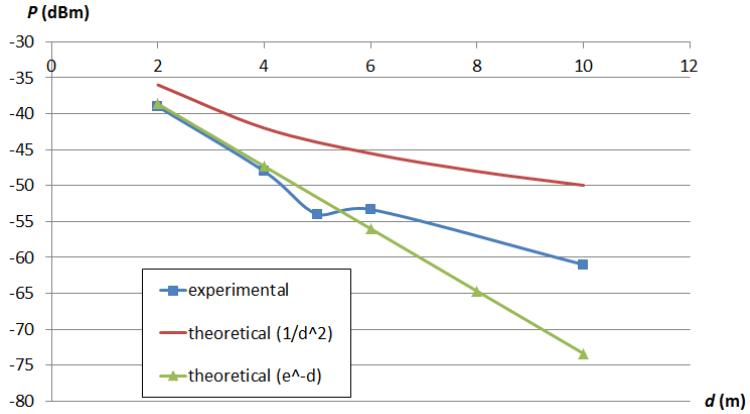

(b)

Figure 56: Theoretical and experimental transmission model. (a) Air. (b) Compost.

In Fig. 56a we can see the experimental model of the transmission through air. We found that the theoretical model that approximated the most was when considering an attenuation of $1/d^2$. This corresponds to what bibliography states at Coulomb's law.

In Fig. 56b we can see the experimental model of the transmission through compost. If we apply an attenuation similar to the found in Equation 3.6 (e^{-d}) we find that the experimental results seem to adequate well to that theoretical model but as good as in the air case. If we consider an attenuation equal to $1/d^2$ we see that the model does not match the experimental data at all. Still, we may consider

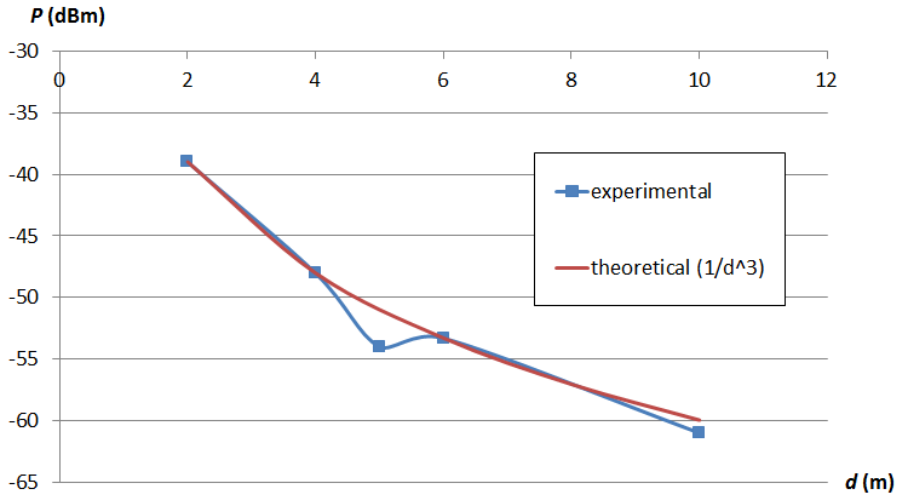

Figure 57: Compost theoretical transmission model for $1/d^3$ attenuation

that the model approximates to a different order. This can be seen as a mathematical series where the attenuation is seen as

$$\sum_{n=0}^{\infty} \frac{a_n}{d^n} = a_0 + \frac{a_1}{d} + \frac{a_2}{d^2} + \frac{a_3}{d^3} + \cdots \tag{3.11}$$

If we apply this equation to the experimental results from compost the coefficients would be $a_0 = -0.0013$, $a_1 = 0.017$, $a_2 = -0.072$ and $a_3 = 1.085$.

In Figure 58 we can see how using a different orde results in the tehoretical model. As can be clearly noted a third order is the one that has the lowest uncertainty.

As such we could say that air behaves as a second order and compost as a third. If we take a look at Fig. 57 we can see how this is fulfilled.

As we can see in the uncertainty between the theoretical transmission model for grain and the experimental results is not too good (from 0.9 % to 20.3 % uncertainty). We consider that variations in the α variable of Equation 3.6 would adequate better the theoretical model to our experimental results. On the other hand, the $1/d^3$ theoretical model approximates better to the experimental results (an error up to 1.71 %, except for the experimental value at d=5 m which is far from the tendency of the rest of experimental data). What is clear is that compost attenuates faster than the air, as one could expect, and that attenuates on a similar way as grain. We can take

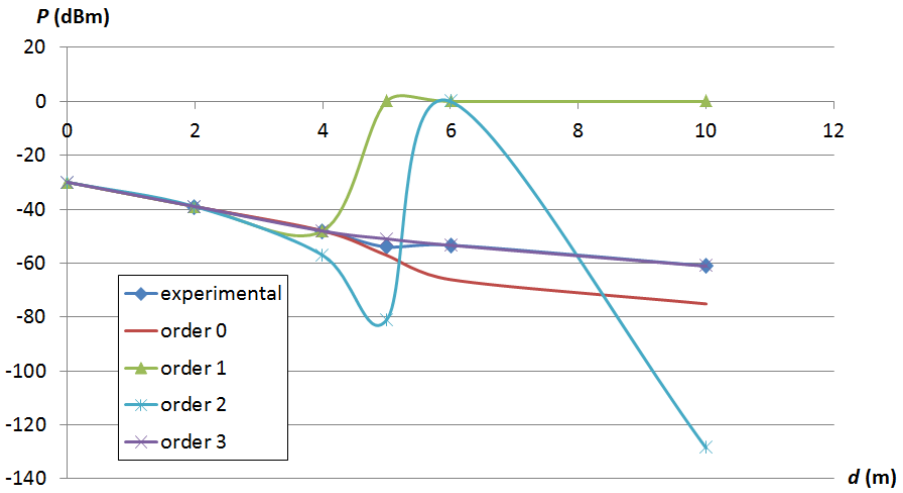

Figure 58: Distance attenuation coefficient uncertainty

these two theoretical models and see what would be the maximum distance at which we could receive the signal.

We will consider a transmitting power of 0 dBm which is the minimum allowed in the 446 MHz frequency band. No gain will be applied to the signal and we estimate from Fig. 55 that the antenna factor is -0.19 dB ($10\log\left(1-10^{(S_{11}/10)}\right)$). Finally, in our specifications we have stated that our reception sensitivity will be -60 dB. If we apply the grain theoretical model to equation 3.10 we obtain that the maximum distance at which we can transmit is 14 m and for the $1/d^3$ model the value rockets to the unreal value of 97 m. The reason why this last value is so high is because this model probably corresponds to near field propagation and for higher distances this model becomes false; we can check how this happens since the uncertainty of the model increases as the distance does.

As we can see, even with the grain model that attenuates far more fast than the experimental model we can obtain a transmission distance up to 14 m inside compost. This is more than enough for our application since we could consider a 10 m distance acceptable without needing to put many balls in a compost pile or tunnel. Still, since other parameters like humidity and density can attenuate the signal further, if we choose a 5 m distance we will guarantee the proper operation.

As said before, these tests were realized on a compost pile in the curing stage, if the composting stage were considered, the result would be more or less the same as experimentally shown in the previous section. The attenuation of the high humidity content in the composting stage may compensated by the low density and, as such, the effect remains the same in the curing stage. Still, if we were

interested in having a larger transmission distance, we could always concatenate transmission systems developing a sensor network.

This kind of network has been implemented within the Compoball project (http://www.compoball.eu/) and its operation has been demonstrated for distances until 4 m in conditions of high humidity content.

In front of so many imbecils with opinion card,
wise men don't talk.

— Pepe Rubianes, comedian

4

HUMIDITY SYSTEM

4.1 STATE OF THE ART AND PROPOSED SOLUTION

To monitor humidity during the composting process, a common way is extracting samples to analyze at a laboratory, with the economical and temporal cost it supposes. Another way of measuring the moisture content of compost is using probes as in temperature [89], but these probes cannot be continuously measuring due to the degradation that supposes to be in contact with the compost material, and their high cost [90].

There are already contact-less solutions that measure moisture content in compost through microwave attenuation [91, 92] inside capsules as in the temperature system. This may be a good solution but high frequency systems result on a considerable increase of the cost and the high water content makes transmission costly in consumption terms. Therefore using lower frequencies would be better in order to reduce consumption, as proposed during the previous chapter.

Another very extended and old solution in the contact-less measure of humidity is using coplanar capacitive electrodes [93]. This solution relies on the shape and dimensions of the electrodes to optimize the humidity measurement. The most famous shape through history for coplanar capacitive electrodes is the interdigital electrode design, the earliest example is found in the patent of N. Tesla in 1891 [94]. And its theoretical expressions for calculation of their capacitance appeared in the 20s [95]. The expanded use of coplanar interdigital electrodes was found in the 60s [96] along with other electrode shapes [97]. But their commercialization did not start until the 80s [98] and 90s [99] in the United States. Many examples, old and new, of coplanar interdigital electrodes in the measure of moisture can be found [100, 101]. And a lot of research based on their performance has been realized; as on their use as capacitive, inductive,

dielectric, piezoacoustic, chemical, biological, and microelectromechanical interdigital sensors and transducers [102]. There are also some poor research about the interdigital electrode dimensions and configurations [103, 104] and therefore an extended research on the optimization of shape and dimensions would be innovative. A part of coplanar interdigital electrodes the next more used shape is the concentric electrode. As said before this shape is not as old as interdigital but their use has been extended up to these days [105]. As in the interdigital case, there is poor research on the optimization of shape and dimensions, even though there are studies that test their sutiability for multilayered dielectrics [106, 107]. Another innovative aspect of our application is the measure of humidity from the inside of a protection. Therefore, a study of the optimization of the electrodes, when a layer of a material is put between the electrodes and a sample which moisture we want to measure, is also innovative.

method	probe	microwave attenuation	coplanar capacitive electrode
contact	direct	contactless	contactless
measure	punctual	continuous	continuous
cost	very expensive	expensive	cheap
consumption	average	very high	average

Table 20: Humidity measure method comparative

As we can see in Table 20, on a first glance we can see that the most suitable method would be using coplanar capacitivie electrodes. We cannot use probes because we need a method to measure humidity continuously; and as such, we can choose to use the microwave attenuation method or the coplanar capacitive elcetrode method.

Whether if we use the coplanar capacitive electrode or the wave attenuation method in the measure of moisture in compost, we will need to know the value of the relative permittivity of compost to be able to theoretically analyze the case. There is no study on the measure of the dielectric constant of compost, which makes it a very innovative work. There is, though, a very rough and not rigorous study on the measure of humidity in front of the dielectric constant of compost taking into account the salt content, the density and the temperature changes [76].

4.1.1 *Proposed solution*

We want to obtain a method to measure humidity from the inside of a protection, from which the state of the art has shown two possibilities: coplanar capacitive electrodes or wave attenuation.

Humidity monitoring through the measure of wave attenuation inside compost consists of a node transmitting a signal to a receiving node where this one calculates the humidity with the attenuation of the wave in front of the distance between the nodes. This scenario does not have a clear theoretical background due to its complexity, but we can use simulation programs to theoretically analyze it. One of the problems of this method is the need to know the location of the balls to calculate the distance between them, which is very complex. Another way to know the distance between nodes would be using two or more training signals at different frequencies which will be differently attenuated and therefore the distance can be calculated. The problem of this solution is the need of a bigger transmission system, which is not only a problem in terms of dimensions but also would imply an even higher power consumption. There is a general problem with this method and that is the lost balls due to the action of the compost turner, as said in section 2.4.1; if there are balls outside the compost pile the calculation of the distance becomes wrong and hence the method cannot be used. Furthermore, as show in the previous chapter, the orientation of the antenna in the communication system is critical if we want to transmit between two nodes.

The humidity monitoring through the use of coplanar capacitive electrodes consists of a pair of electrodes inside a ball emitting an electric field that is affected by the material it goes through (Fig. 59). Although coplanar capacitive electrodes do have theoretical models, the scenario results more complex and thus these models cannot be used. Hence, a simulation software should be used to theoretically analyze this method, just like in the previous one. In this case, there is no problem with the location of the balls: if it is inside the pile it will measure, if not, it will not; there is nothing else about it. But the greatest advantage of this method has in front of the previous one is power consumption; we are developing an autonomous system and, as such, this factor is critical.

Therefore we will develop a humidity sensor system based on the changes of a pair of coplanar capacitive electrodes placed inside a capsule. The humidity system will have the same specifications of the temperature system (Chapter 2) but with the change that the maximum required accuracy of this system will be of a ± 5

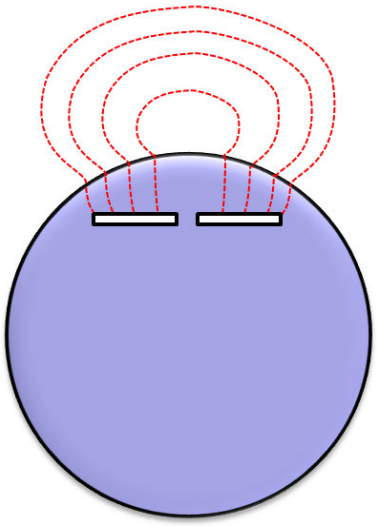

Figure 59: Coplanar capacitive electrode

% of relative humidity. The reason behind that is because current commercial humidity sensors are accurate within a $\pm$ 2 % to $\pm$5 % margin[108, 109], which will give a very good idea of what the humidity level is in the environment. And thus, if our system fulfills a maximum 5 % RH accuracy it will be more than enough for the detection of non desired moisture levels in compost.

4.2 COMPOST RELATIVE PERMITTIVITY

As said at the beginning, in order to theoretically optimize the design of coplanar capacitive electrodes we need to know how the value of the relative permittivity changes in compost. To measure the relative permittivity of a material, it has to be put between two capacitive electrodes. The generic equation for capacitive electrodes is [110]

$$C = \varepsilon \cdot K_c \cdot \Gamma \tag{4.1}$$

where C is the capacitance between the electrodes, ε is the absolute permittivity of the material between the electrodes, K_c is the capacitive corner effect (also known as edge effect) and Γ is the geometric factor.

A real capacitor is finite in size. Thus, the electric field lines at the edge of the plates are not straight lines, and the field is not contained entirely between the plates. This is known as corner effects, and the non-uniform fields near the edge are called the fringing fields [111]. However, to avoid complex calculations, in what follows, we shall ignore such effects and assume an idealized situation, where field lines between the plates are straight lines, and zero outside. Further information regarding the corner effect modeling can be found in [112, 113].

4.2.1 *Parallel plate capacitor*

The simplest form of a capacitor is two parallel flat conductive plates separated by a dielectric material [114]. As such, its evaluation is well-known and has been widely studied. That is the reason why we started using that kind of capacitor to evaluate compost relative permittivity.

Parallel plate theoretical model

The capacitance (C) of a parallel plate capacitor is also known as the capacitance between two horizontal flat conductors [110]. In the limit where the plates are infinitely large, the system has planar symmetry and we can calculate the electric field everywhere using Gauss's law described as

$$C = \varepsilon \frac{A}{d} \tag{4.2}$$

where A is the area of the plate and d is the distance between the plates.

We want to find the relative permittivity of the material (ε_r) and our horizontal flat conductors are rectangular ($A = l \cdot h$), therefore the equation is expressed as

$$\varepsilon_r = \frac{C \cdot d}{l \cdot h \cdot \varepsilon_0} \tag{4.3}$$

where ε_0 is the vacuum permittivity ($\varepsilon_0 \approx 8.85... \cdot 10^{-12}\,F \cdot m^{-1}$), l is the length of the plate and h is its height.

Experimental setup

The parallel plate capacitor consisted on two copper rectangular board in parallel separated by four nylon screws. The plates were 20 cm long and 15.5 cm high with a separation of 2.7 cm between them. For the measure of impedance, the capacitor was connected to a 4294A *Hewlett Packard* Impedance Analyzer as seen in Fig. 60.

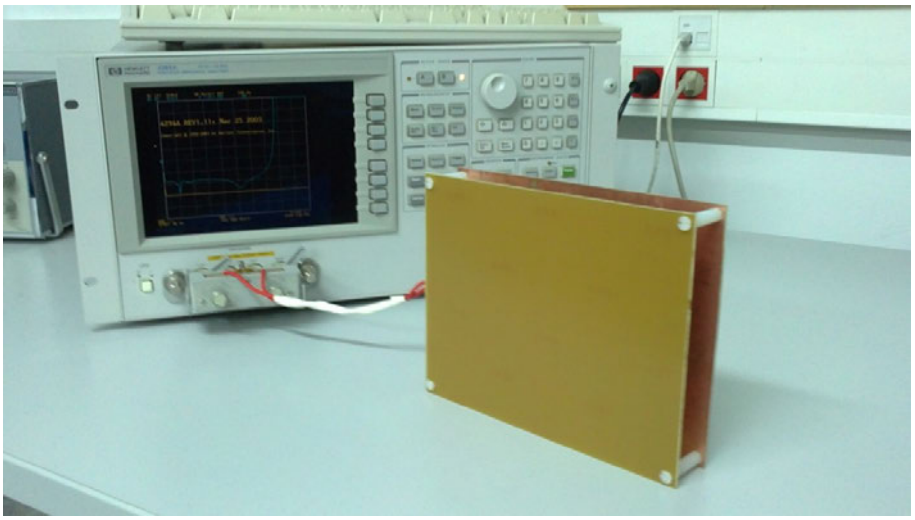

Figure 60: Experimental setup

The compost for the tests was gotten from active composters, mostly in the decomposition stage, located at the backyard of the *Escola Superior d'Agricultura de Barcelona* (ESAB) from the *Parc Mediterrani de la Tecnologia* (PMT). The samples of compost were put into metallic trays and were transported inside a portable fridge.

Once the measure of the impedance is gotten, then the electrical equivalent model is approximated, in order to get the capacitance change due to the dielectric between the plates.

Results and discussion

We needed to find the electrical equivalent model for the measure of capacitance of the parallel plates with compost. With the theoretical electric model we can extract the values of the components (including the capacitance due to the dielectric between the plates) of the model that suit it to the experimental result. We have done that by taking the experimental data and introducing it to a *Matlab R2011a* algorithm that found the values that got the nearest theoretical impedance module to the experimental one.

For that we started from the basic model which corresponds to the parallel plates with air. The corresponding model is an RC parallel or serial (in this case we applied the parallel one) with the inductive effect of the cables (serial inductances), as is demonstrated in Fig. 61. Values for the equivalent theoretical parallel resistance, parallel capacitance and cable inductance are $R_p = 29.10$ k˙, $C_p = 18.64$ pF, $L = 0.19$ —H respectively.

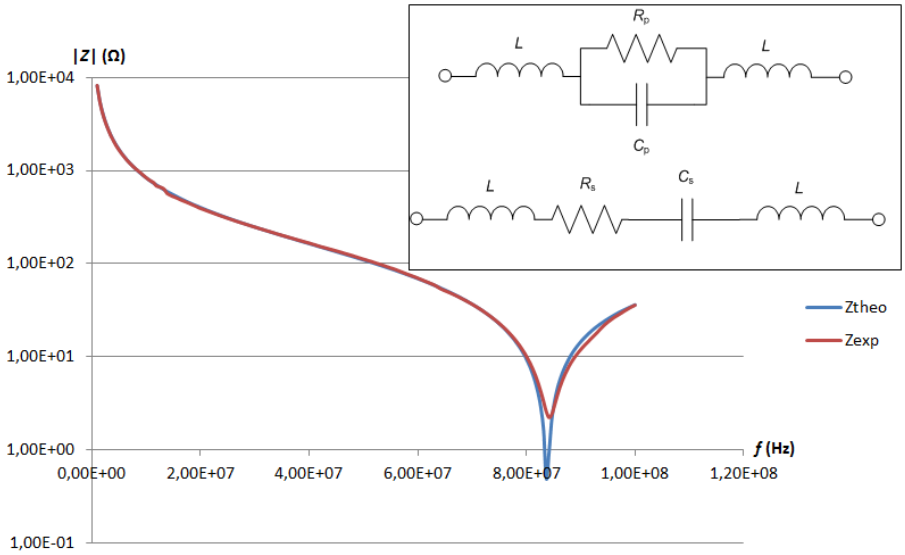

Figure 61: Electric equivalent model of the parallel plates with air

We applied this electric model to the plates filled with compost and we obtained that the RC serial model does not suit our configuration whilst the RC parallel model suits high frequencies (Fig. 62 with $R = 39.17$ ˙, $C = 0.14$ nF, $L = 0.19$ —H), except for some disturbances in the measure at the highest frequencies. The mechanism responsible for the dispersion is equivalent to a complex impedance with a phase angle [115] which depends on the kind of dielectric we are testing.

If we obtain the average uncertainty between the theoretical model and the experimental one we get a 7.70 % and a maximum of 182.50 %.

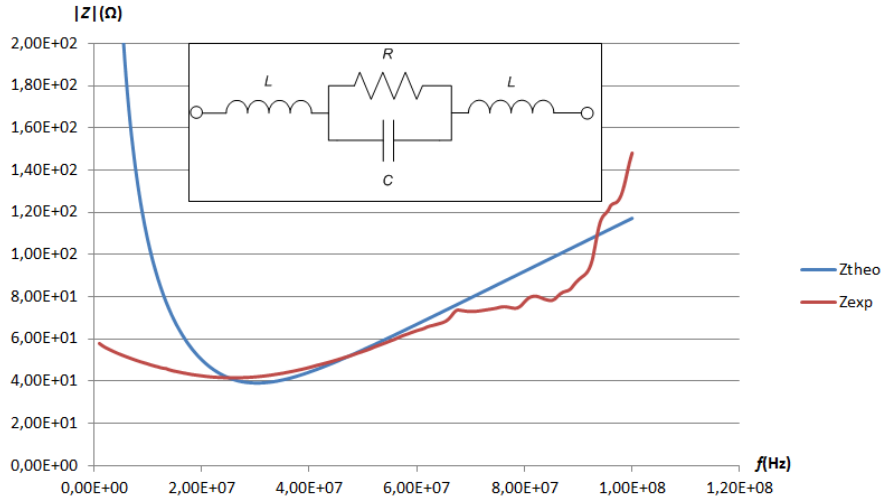

Figure 62: Electric equivalent model of the parallel plates with compost

The behavior of the configuration gives the idea that the parallel plates filled with compost create a virtual capacitance to ground. If we apply a T model to our configuration we obtain Fig. 63, with R = 21 ˙, C = 10 nF, L = 96.80 nH, C_i = 10 pF. As we can see this model suits better to the experimental impedance. However, there is an effect at low frequencies that seems to correspond to a serial resistance.

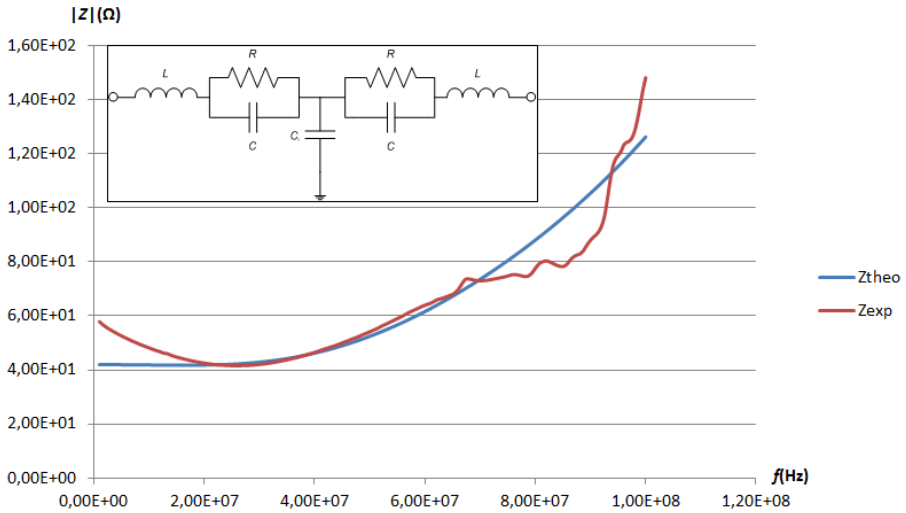

Figure 63: T electric model of the parallel plates with compost

If we add serial resistances to the T model we obtain Fig. 64, with $R_1 = 9.5$ ˙, $R_2 = 15$ ˙, $C = 0.3$ nF, $L = 96.80$ nH, $C_i = 5$ fF. The effect at lower frequencies is not entirely erased and the disturbances at frequencies over 70 MHz are something to really worry about. Also, from 30 MHz we can see the inductive effect of the cables.

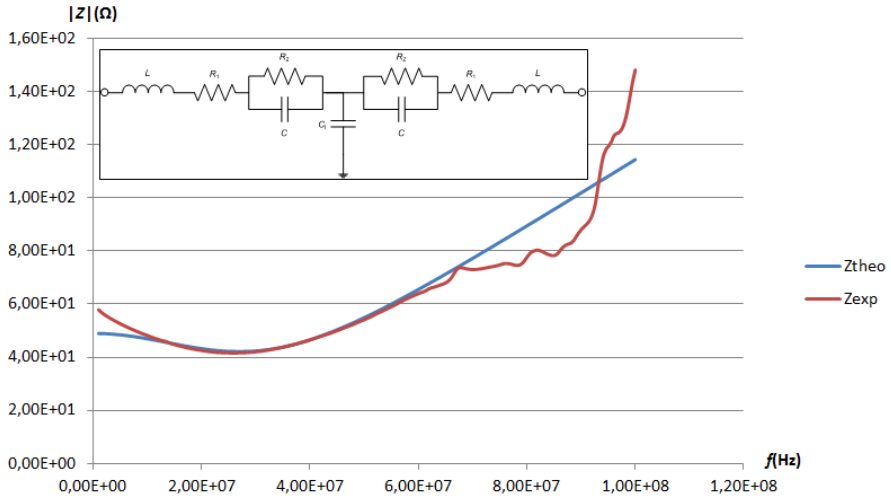

Figure 64: T with serial resistance equivalent model of the parallel plates with compost

The average unceratinty in this case results 2.07 % and the maximum 22.77 %.

The measure of impedance with parallel plates leads to a very complex equivalent electric model which does not guarantee the proper measure of the relative permittivity of compost in function of the relative humidity. The corner effect is represented as an inductive effect at high frequency (capacitance to ground) and some losses (serial resistance). Ultimately, the combination of the inductance of cables, the corner effect and the geometry factor affect the measure in a very complex way. Another setup would be needed in order to avoid this issues and to properly measure permittivity.

Still, this setup allowed measuring the frequency behavior of the impedance module in function of temperature, humidity and density.

IMPEDANCE FREQUENCY BEHAVIOR IN FUNCTION OF TEMPERATURE In this test we took a sample of compost at a high temperature and we put it between the plates of the capacitor. We measured the impedance module at different times as it was cooling down in order to measure the impedance module at different temperatures, keeping the same humidity, density and salt content. Each time a

measure was taken the temperature was measured with a *Delta Ohm* 9406 Thermometer probe afterward.

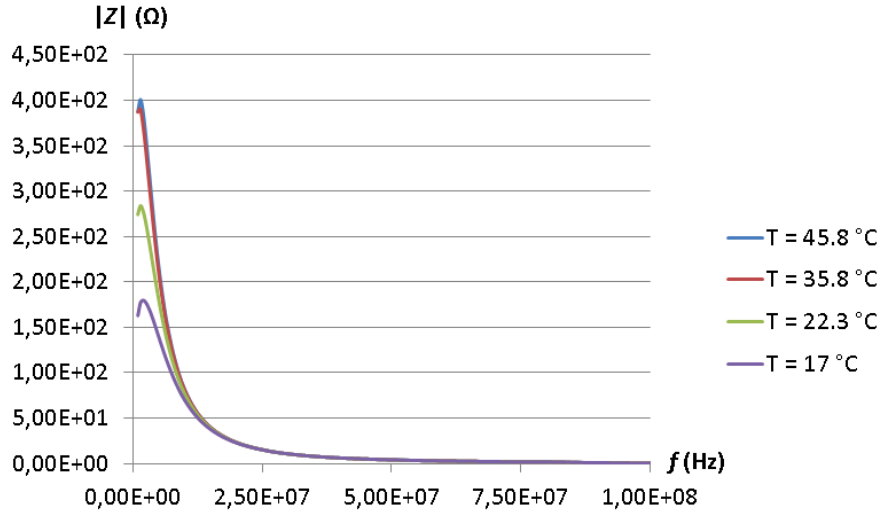

Figure 65: Impedance temperature and frequency behavior

As we can see in Fig. 65 the impedance module decreases as the temperature does. But is this true for all frequencies? What is the uncertainty that the temperature introduces between measures? If we compare the 45.8ºC case to the other three we obtain Fig. 66.

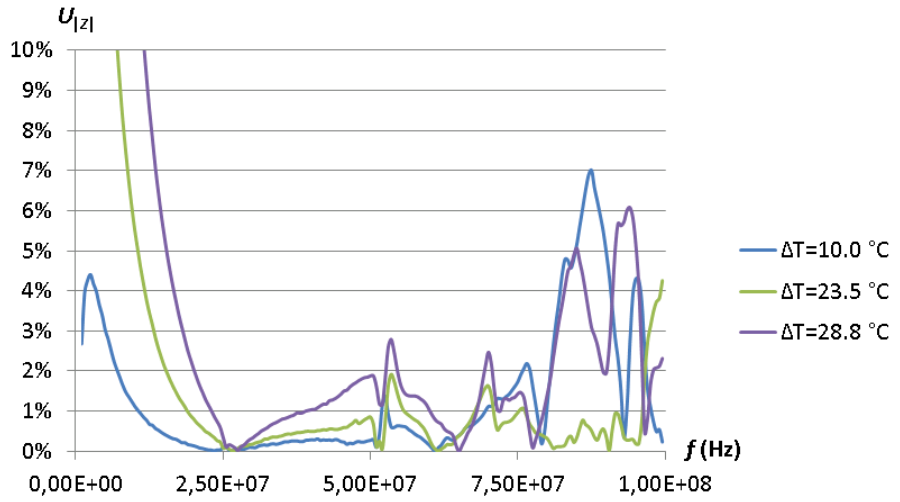

Figure 66: Error temperature and frequency behavior

As can be seen, the highest uncertainties appear at the lower frequencies. Also we can see that from 25 MHz on, the uncertainty is really low, taking into account that the uncertainty is not only due to the temperature, but also due to other disturbances as the

equipment uncertainty or the own disturbances of the configuration. Moreover, at frequencies above 70 MHz the value of uncertainty does not answer to the difference in temperature, mainly due to the disturbances of measuring high frequencies with this configuration and this equipment.

So it seems that to reduce the uncertainty the temperature introduces in the measure we should measure from frequencies over 25 MHz, as one would expect since the real part (temperature depending) of the impedance predominates at low frequencies. Still, we cannot be completely sure because in the test when cooling down the temperature it is possible that the humidity would have changed as well. Air is supposed to increase its humidity when cooling down due to not be able to contain the same quantity of water vapor [116].

IMPEDANCE FREQUENCY BEHAVIOR IN FUNCTION OF HUMIDITY

In this test we took a sample of compost and kept it at room temperature, the water content of the sample was varied in order to modify its humidity and the density was kept constant. In Fig. 67 we can see the change in impedance in function of the frequency for three variations in humidity.

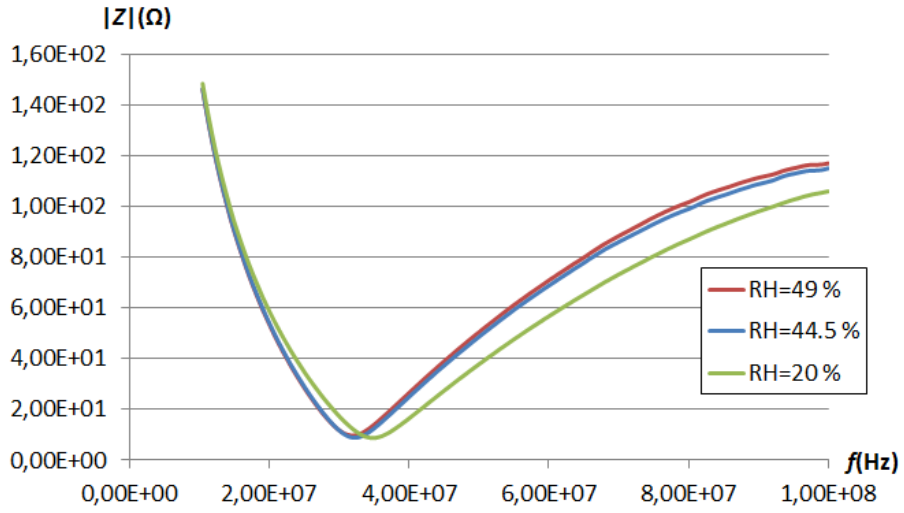

Figure 67: Impedance humidity and frequency behavior

As we can see the variation for a small increase in humidity (from 44.5 % to 49 %) is translated as small variation in the impedance change (and small capacitance change: 265 pF to 300 pF) and for a high increase (from 20 % to 44.5 %) there is a much higher variation in the impedance change (and bigger capacitance change: 85 pF to 265 pF). Also, we can understand that the change in humidity is higher as the frequency increases. This is somewhat logical since the

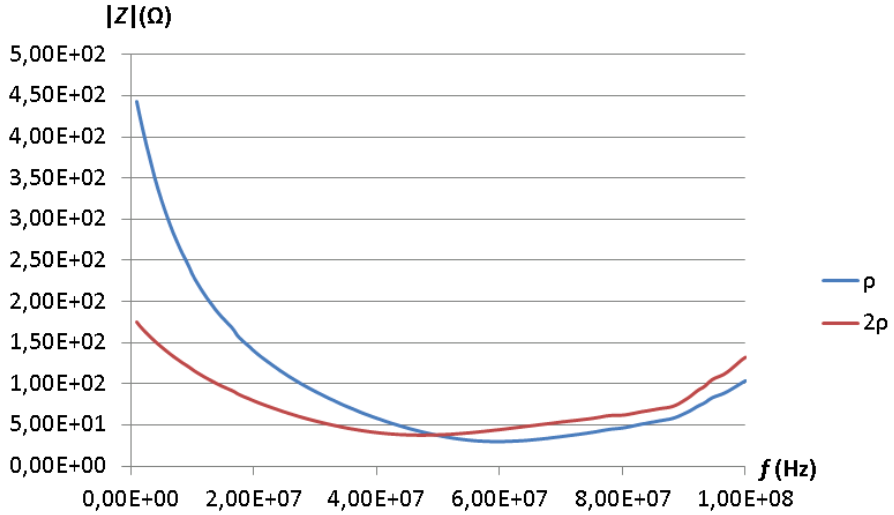

Figure 68: Impedance density and frequency behavior

imaginary part (relative permittivity depending) of the impedance predominates at high frequencies. Temperature affects lower frequencies and humidity affects higher frequencies, hence we can measure for a frequency band in the higher frequencies.

IMPEDANCE FREQUENCY BEHAVIOR IN FUNCTION OF DENSITY

In the following test we measured the impedance of a sample of compost with a first measure distributing half of a tray between the plates and a second one compacting the whole tray between them. This way, we measured the variation of the impedance module when doubling the density of compost, whilst keeping temperature, humidity and salt content constants.

As we can see in Fig. 68 the effect of changing the density in compost modifies the whole frequency spectrum. This is expected since density affects both relative permittivity and thermal conductivity when change per se.

4.2.2 *concentric cylinder capacitor*

To improve the measure of the impedance of compost a concentric cylinder capacitor is suggested. Two concentric cylinder allow decreasing the distance between electrodes and, thus, reducing the corner factor. The length of both cylinders is to be much larger than the separation of the cylinders, so that corner effects can be neglected. Furthermore, a cylinder only has two sides in contact with the outside and, as such, the corner factor is halved and the parasite capacitance to ground is also reduced.

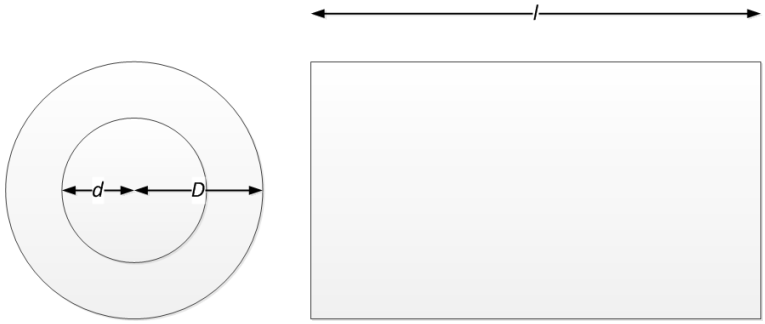

Figure 69: Cylinder dimensions

Concentric cylinder theoretical model

For a cylindrical geometry, the capacitance (C) is usually stated as a capacitance per unit length [117]. The charge resides on the outer surface of the inner conductor and the inner wall of the outer conductor. The capacitance expression is

$$\frac{C}{l} = \frac{2\pi\varepsilon}{\ln\left(\frac{D}{d}\right)} \tag{4.4}$$

where ε is the absolute permittivity of the material between the cylinders, l is the length of the cylinders, D is the radius of the outer cylinder and d is the radius of the inner cylinder (Fig. 69).

Since we are interested in the value of the relative permittivity (ε_r), the expression results

$$\varepsilon_r = \frac{C \cdot \ln\left(\frac{D}{d}\right)}{l \cdot 2\pi\varepsilon_0} \tag{4.5}$$

Measurement methodology

From the experience measuring with the parallel plate capacitor, we decided to develop a measurement methodology (Fig. 70) to avoid any interference of any non desired parameter. We want to measure Humidity changes and so we will keep temperature, salt content and density constants during the measurements. We will start by taking a big sample of compost which will be mixed with a lot of water in order to increase its humidity as much as possible. As follows we will pour the mix between the cylinder electrodes and next we will weigh the electrode filled and write down the result. Then we will do the measurement and take a sample of the mix to measure its humidity with the *AND* ML-50 Moisture Analyzer. While the

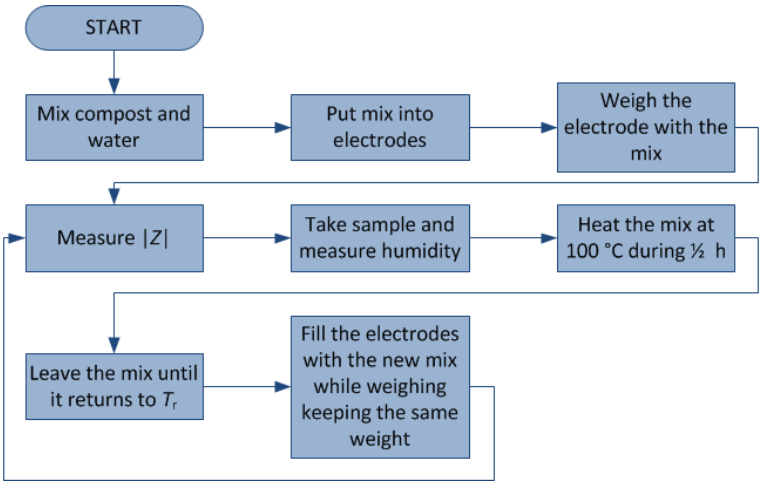

Figure 70: Compost dielectric characterization method

humidity is being measured and the measurement has been made we will heat the mix into a *FCH* climatic chamber at 100°C during 30 min to decrease its humidity without modifying the salt content. Once the mix is at room temperature (T_r) we will fill the electrodes with the mix again while weighing at the same time, trying to keep the same weight of the previous test (this way we keep the same density) and we can repeat the process again.

Experimental setup

The test capacitor consisted on two aluminum concentric cylinders with a 15 cm length and a diameter of 4.4 cm for the bigger and 1.7 cm for the smaller. The two cylinders were glued to a 5 cm edge polystyrene platform as shown in Fig. 71.

Also, the capacitor was connected to the 4294A *Hewlett Packard* Impedance Analyzer with an *Agilent* 4294A Impedance calibrated probe to reduce the effect of cables. Still, the measurement of compost, from 25 MHz to 100 MHz (extracted from the results in the parallel plate configuration), suffered of inductive masking and so two 220 pF capacitor were used in serial to move this effect and have a clear view of the capacitive measurement.

With this setup, we understand the equivalent electric model as a simply RC parallel with an inductance and a 220 pF capacitance in serial for each connection (Fig. 72). The ground capacitance we found in the previous electrodes still exists, but it is so small that we can not consider it.

In Fig. 73 we can see how this electric model is successfully applied to an experimental test (for a relative humidity of 44.7 %) with theoretical values of R = 24.80 ˙, C = 26.50 nF, L = 0.13 —H. The

Figure 71: Experimental setup

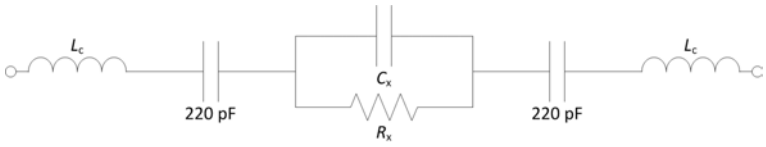

Figure 72: Experimental setup equivalent electric model

model does not adjust completely due to the higher disturbances at higher frequencies

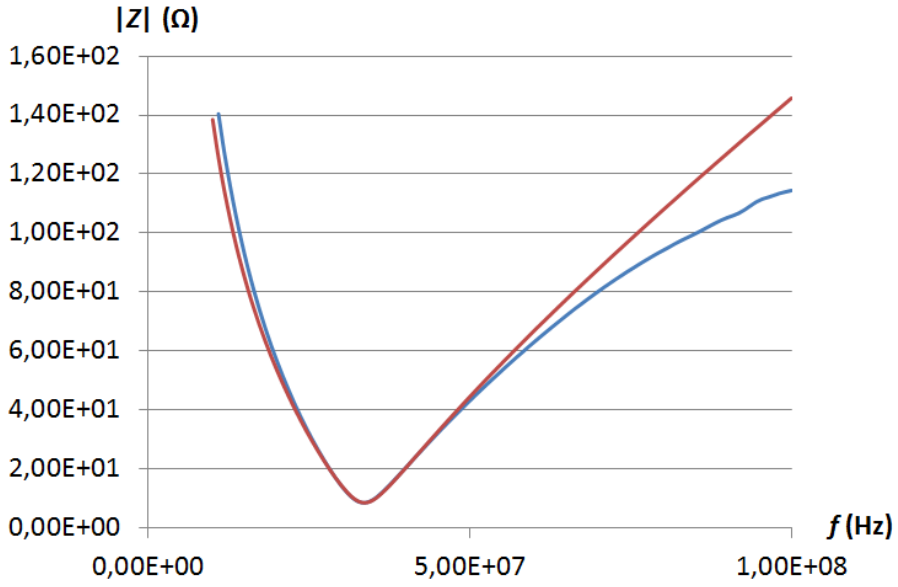

Figure 73: Theoretical model applied to experimental test

The average uncertainty between the theoretical model and the experimental results is 1.84 % and the maximum is 21.50 %. As we can see we obtain not only a better uncertainty than the equivalent theoretical model for the parallel plate, but also a better uncertainty than the complex theoretical model in the parallel plate.

Results and discussion

The value of the capacitance was measured for two cases of density and a variation of the humidity for each case. As in the previous configuration the capacitance was found by introducing the experimental data to a *Matlab R2011a* algorithm that found the values that got the nearest theoretical impedance module (from the model of Fig. 72) to the experimental one. With the values of capacitance, the dimensions of the capacitor and Equation 4.5 we were able to determine the relative permittivity of compost in function of its relative humidity for two cases of density (Fig. 74).

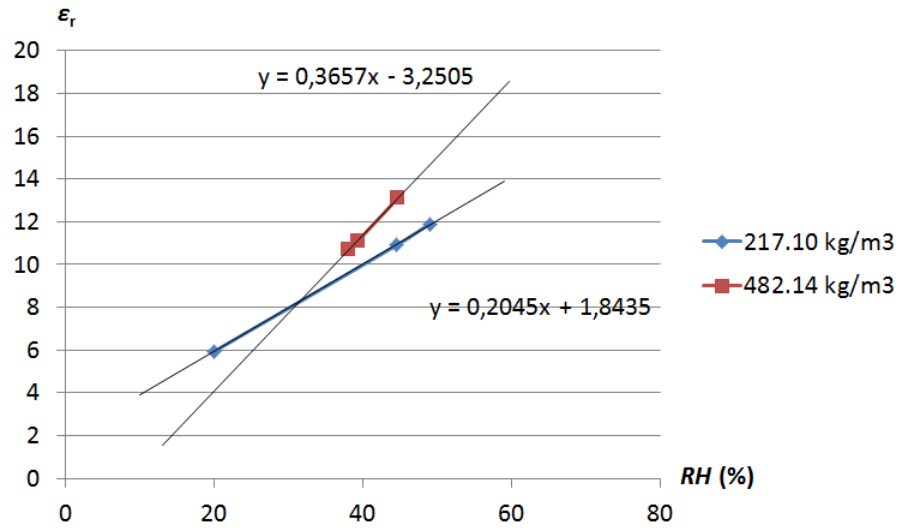

Figure 74: Relative permittivity of compost in function of the relative humidity

As we can see the relation between the two variables is linear with a variation of the gain and the offset. If we extrapolate how the relation humidity/permittivity varies in function of the density we obtain:

$$\varepsilon_r = (6.13 \cdot 10^{-4}\rho + 7.14 \cdot 10^{-2})RH - 1.92 \cdot 10^{-2} \cdot \rho + 6.02 \quad (4.6)$$

where ρ is the density of compost and *RH* is its relative humidity.

$RH \setminus \rho$	100 kg/m^3	800 kg/m^3
30 %	8.08	7.50
80 %	14.71	35.59

Table 21: Theoretical relative permittivity in function of the composting process ranges of humidity and density

If we consider the ranges of humidity and density for the composting process we obtain Table 21. As we can see the relative permittivity increases proportionally to humidity, and for high values of humidity the same happen with density; but for low values of humidity the relative permittivity decreases when density increases.

When calculating the relative humidity of compost using the capacitive coplanar electrodes we obtain the capacitance from the electrodes with the corresponding conditioning circuit. As follows, the relative permittivity can be calculated with Equation 4.1, considering k_c negligible and calculating Γ with a calibration of the electrodes used. Then, taking into account that the density is time variant and can be estimated with the time the composting process has been active, we can calculate the relative humidity with Equation 4.6.

4.3 COPLANAR ELECTRODE STUDY AND DESIGN

In the following sections we will study the effect of shape and dimensions of concentric and interdigital coplanar electrodes on the nominal capacitance, the capacitance change and the capacitance change over the nominal capacitance. We will also optimize the shape and dimensions of the coplanar electrodes applied to the measure of permittivity changes of compost from inside a protection. The optimized electrodes will be simulated in front of disturbances as is the effect of the presence of the circuitry, air and water bags as a source of noise.

4.4 SINGLE-LAYER COPLANAR CAPACITIVE ELECTRODES

Sensors based in coplanar capacitive electrodes are widespread among the most commonly used. Recent advances in such fields as nondestructive testing (NDT), microelectromechanical systems (MEMS), telecommunications, chemical sensing, piezoacoustics, and biotechnology involve coplanar capacitive electrodes in very different ways [102].

The most famous shape through history for coplanar capacitive electrodes is the interdigital electrode design, the earliest example is found in the patent of N. Tesla in 1891 [94]. And its theoretical expressions for the calculation of their capacitance appeared in the 20s [95]. The extensive use of coplanar interdigital electrodes was found in the 60s [96] along with other electrode shapes [97]. But their commercialization did not start until the 80s [98] and 90s [99] in the United States. Many examples, old and new, of coplanar interdigital electrodes in the measure of moisture can be found [100, 101]. And lot of research based on their performance has been realized [76]. There are also some research about the interdigital electrode dimensions and configurations [103, 104] very limited by their specific use and difficult replication. Therefore, an extended research on the specific optimization of shape and dimensions would be innovative. A part of coplanar interdigital electrodes the next more used shape is the concentric electrode. As said before this shape is not as old as interdigital but their use has been extended up to these days [105]. Their advantages and disadvantages compared to the interdigital are not really analyzed in the bibliography. As in the interdigital case, there is poor research on the specific optimization of shape and dimensions and so it is something else to take into account.

In this chapter we will present an optimization of the shape and dimensions of interdigital and concentric coplanar capacitive electrodes, and the differences from using one or the other. As follows, the general problem is described. Subsequently, a research of the theoretical models found in the state of the art are analyzed. Then different configurations for interdigital and concentric coplanar electrodes are simulated to see the behavior in function of the dimensions and shape. Then, those configurations were experimentally tested and some conclusions and design recommendations were finally extracted.

4.4.1 *General problem description*

Capacitive electrodes are used to measure changes in the relative permittivity of a material. This parameter can give information about other magnitudes like humidity, density, temperature and salt content of the material.

There are many influencing parameters when measuring with capacitive electrodes. We can see two if we take a look at the generic equation for any capacitive electrode [110]

$$C = \varepsilon \cdot K_c \cdot \Gamma \tag{4.7}$$

C is the capacitance between the electrodes and ε is the absolute permittivity of the material between the electrodes. The first nuisance parameter is K_c, which is the capacitive corner effect. This effect varies in function of the geometry, as we can say it strongly decreases in cylindrical electrodes and it disappears in spherical electrodes. On the other hand we find Γ, which is the geometric factor that may have a great uncertainty when trying to theoretically model the electrodes. Apart, some other uncertainty sources may be the material properties, the thermal noise in the measuring circuit and the effect of the electromagnetic compatibility, between others.

When designing a capacitive transducer for the measure or detection of a magnitude we rely on the specifications of our system. There are many applications in which we need to have a minimum value of capacity for our conditioning system to be able to measure it, and as such we should be careful with the **nominal capacitance** value of the transducer. Moreover sometimes we are measuring almost perfect materials that have no problems with its material composition uncertainty; in those cases we are interested in the sensitivity of the transducer in terms of **capacitive change**.

Normally, the material we are measuring is not perfect and we have to deal with this material property uncertainty; therefore we would be interested in maximizing the sensitivity as **capacitance change over nominal capacitance**. According to Equation 4.1, this value would be constant regardless of the type of electrodes we use, but this equation answers to a system with a single dielectric, and as such is not applicable here. Compost is a very heterogeneous material composed by many different dielectrics (but mainly categorized as organic matter, water and air), we can estimate what the relative permittivity integration of these dielectrics equals to but we cannot extract this uncertainty as a multiplying geometric factor or a corner effect.

4.4.2 *Theoretical models*

An approximate expression for the capacitance of an interdigital structure (see Fig. 75) was derived in the 1970s and later reported in [118]. The capacitance C between the drive and sense electrodes immersed in an infinitely thick layer of resin, as shown in [102], is

$$C = \frac{4\sqrt{2}\,(N-1)\,l_{teeth}}{\pi^2}\left[\varepsilon_{resin} + \varepsilon_{sub} + \frac{\pi T}{l_s}\varepsilon_{ox}\right] \tag{4.8}$$

where N is the number of teeth of the electrodes, l_{teeth} is the length of the teeth, ε_{resin} is the dielectric permittivity of the material under test (in this case resin), ε_{sub} is the dielectric permittivity of the substrate under the electrodes, T is the oxide layer thickness, l_s is the inter-electrode separation and ε_{ox} is the dielectric permittivity of the material that holds the electrodes (oxide in this case).

This is an approximate model, which can predict the capacitance values for equal (or closed, based on an error function) teeth and gap width, and with an infinite top air layer. The limitation of that model consists on not taking into account the effect of the lines to which the teeth of the electrodes are attached to and the corner effects. As such any minor change in these lines or the thickness of the electrode may affect the result.

That model was modified by Hobdell [119] in 1979 introducing a loss term into Alley's theory, and by Esfandiari et al. [120] in 1983, which incorporates the influence of the metallization thickness into the total value of the capacitance. The complexity of the model keeps increasing the closer to reality it comes. One of the most accurate analytical evaluations appeared in 2004 [121] basing its model into a single semi-infinite layer capacitance using an equivalent electric

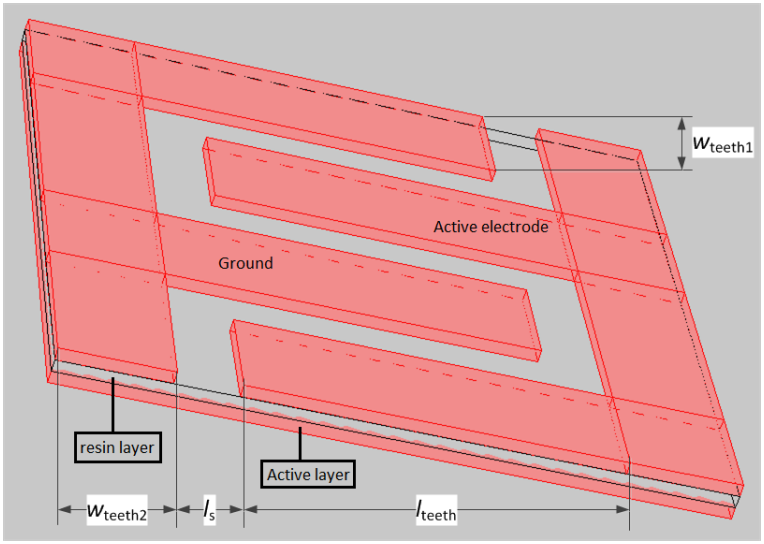

Figure 75: 3D Interdigital electrodes

circuit. For symmetry reasons, the capacitance is evaluated as a function of two types of capacitance: (1) C_I—being half the capacitance of one interior teeth relative to the ground potential and (2) C_E—the capacitance of one outer teeth relative to the ground plane next to it.

$$C = (N-3)\frac{C_I}{2} + 2\frac{C_I C_E}{C_I + C_E}, \quad N > 3 \tag{4.9}$$

where N is the number of teeth. The calculation of C_E and C_I includes complex calculations as complete elliptic integrals of first kind, and does not take into account the influence of corner effects.

The processing of such complex theoretical models require heavy computational work that would imply spending great effort and time in something that can be easily done using simulation tools. Also, taking into account the inaccuracy of approximated calculations we decided simulating the different electrode configurations in order to have the highest accuracy with the minimum complexity. Moreover, whilst there are different theoretical models for each shape, the simulation process is the same.

In the case of concentric capacitive electrodes, the capacitance C_T between the two electrodes, can be calculated through [105]

$$C_T = \left.\frac{Q_{outer}}{V_{inner}}\right|_{V_{outer}=0} \tag{4.10}$$

where Q_{outer} is the total charge on the outer electrode, while V_{inner} and V_{outer} respectively represent the voltage on the inner and outer

electrodes. The total charge, on both inner and outer electrodes, can be found integrating over the electrode surfaces with the surface charge distribution $\sigma(\rho')$. In order to calculate the surface charge distribution, Green's functions [122] for the method of moments (MoM) [123] are used. We have to take into account that the method of moments is used in simulation tools, and hence we see that for complex theoretical models in the case of concentric capacitive electrodes the option is also simulating.

Considering all previous models we will work with simulations to fulfill our objective of finding the design optimization for interdigital and concentric electrodes.

4.4.3 *Simulation*

All the simulations were realized with *COMSOL Multiphysics* v4.2a on a computer running *Windows 7 Enterprise* with a processor *Intel Core* i7 CPU 860 @ 2.80 GHz, a RAM memory of 16 GBytes and a 64 bit OS.

In all the cases, a 2 m environment sphere was created as compost implying that the electrodes are surrounded by a very big compost mass (relative permittivity changed from 10 to 15, in other words, from a lower humidity to a higher) with a zero charge electrostatic state, along with a pair of copper coplanar electrodes (with one of them as 3 V electric potential and the other as ground) in the center and a copper active shield 1 mm under them (with 3 V of electric potential), that focuses the area affected by the electrodes to the front. The electrodes and the active shield were separated by a 1 mm layer of resin (relative permittivity of 3.1 [63]), as in the typical printed circuit plaques, with a charge conservation electrostatic state.

The area of the concentric and the interdigital electrodes is the same in all the cases; as such, the concentric electrodes are a circular plaque of radius 3 cm and the interdigital electrodes are a squared plaque of side 5.3 cm. The different configurations have been thought within these dimensions and the limit values for each dimension were tested.

The simulations had an extra fine mesh and the electrode capacitance (C) was evaluated as an integration of the active electrode surface charge density (σ) divided by the applied voltage difference across the electrodes (ΔV)[124], similarly to what we saw in equation 4.10

$$C = \int \frac{\sigma}{\Delta V} dA \tag{4.11}$$

The capacitance of electrodes could also be calculated as the integration of the ground electrode surface charge density divided by the voltage or as the global evaluation of the total stored electric energy (W_e) divided by the voltage difference across the electrodes ΔV[125]

$$C = \frac{2 \cdot W_e}{\Delta V^2} \tag{4.12}$$

The problem of the integration of the ground electrode and the global evaluation is that they include the electromagnetic fields going from the active shield to ground and therefore the result would not purely be the effect of the sensing electrode to the ground electrode.

From the capacitance value, there will be three variables analyzed: the nominal capacitance (C_1 and C_2, that are the capacitance values of the electrode for a relative permittivity of 10 and 15 respectively), the capacitance change and the capacitance change over the nominal capacitance. The nominal capacitance value is interesting for applications needing a minimum value of capacitance. The capacitance change ($\triangle C$) is interesting for applications in which the predominant disturbance is the noise of the system, which does not change in function of the permittivity and is defined as the difference between C_1 to C_2. And the capacitance change over the nominal capacitance ($\triangle C/C_1$) is interesting for applications in which the predominant disturbance is the inaccuracy due to the heterogeneity of the material.

Concentric electrodes

The concentric electrodes (Fig. 76) consisted of an active circular electrode of radius r_a and thickness 1 mm, surrounded by a ground ring electrode of outer radius of 3 cm, inner radius $r_{g,i}$ and thickness 1 mm. The resin layer and the active shield were 6 cm radius circles with 1 mm thickness.

The simulations were realized in order to see the performance of the electrodes when varying the separation between electrodes or the size of one electrode respect to the others. As follows, the nominal capacitance of the electrodes, their capacitance change and their capacitance change over the nominal capacitance are calculated in function of the separation between electrodes and the size of the active electrode radius.

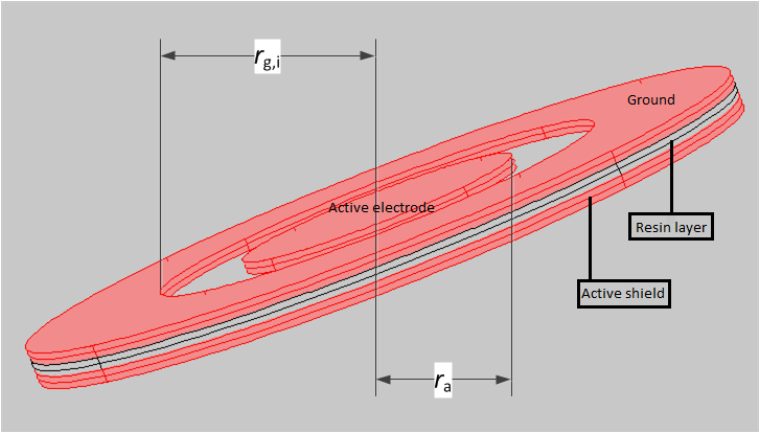

Figure 76: 3D Concentric electrodes

SEPARATION BETWEEN ELECTRODES (l_{sep}) In this case we simulated the change in capacitance in function of the separation between electrodes ($l_{sep} = r_{g,i} - r_a$). The size of both electrodes was equally reduced as the separation increased. Their start values for $l_{sep} = 0.3$ cm were $r_a = 1.35$ cm and $r_{g,i} = 1.65$ cm. The subsequent iterations followed by increasing l_{sep} by 0.2 cm, and reducing r_a and $r_{g,i}$ by 0.1 cm. The penultimate value was $l_{sep} = 1.7$ cm and then a jump is made with a final simulation with $l_{sep} = 2.8$ cm.

From Fig. 77 we obtain that if you want to increase the nominal value of capacitance you need to reduce the separation between electrodes. This is logical since what we are doing is increasing the size of the electrodes.

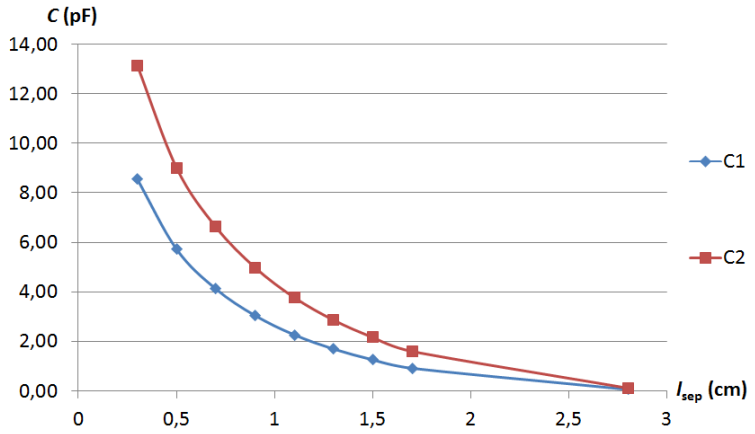

Figure 77: Nominal Capacitance change in function of l_{sep}

In Fig. 78 we see that the smaller the separation between electrodes, the bigger is the capacitance change. Still, we can see that the improvement is faster in the nominal capacitance than in the capacitance change. This effect determines the capacitance change

over the nominal capacitance (Fig. 79) where we see that if you want to maximize the capacitance change over the nominal capacitance you have to increase the separation. This case, corresponds to the electromagnetic waves that find their way from the active electrode to the ground electrode through the resin layer. When we increase the separation between electrodes the waves of the active shield become more present between the active and the ground electrode, and thus, the waves of the active electrode cannot go through the layer of resin and have to go through the compost.

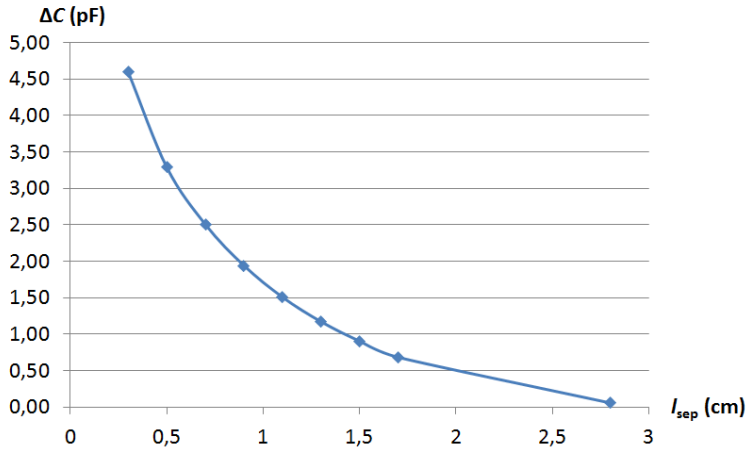

Figure 78: Capacitance change in function of l_{sep}

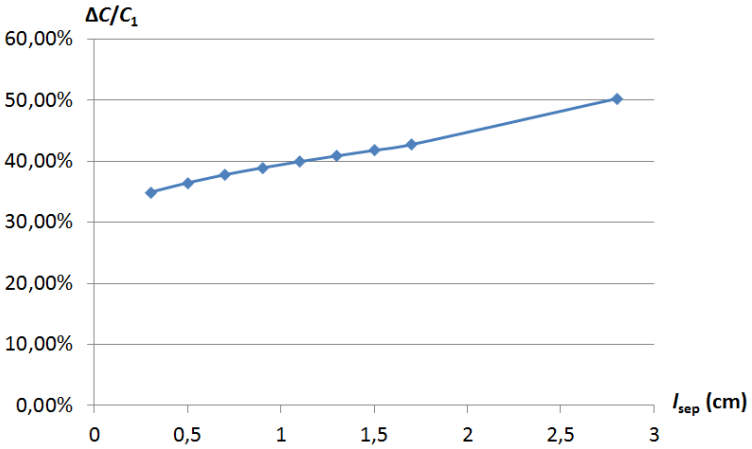

Figure 79: Capacitance change over Nominal Capacitance in function of l_{sep}

ACTIVE ELECTRODE VS GROUND ELECTRODE In these simulations we measured the change in capacitance in function of the size of the active electrode. The separation between electrodes was fixed as $l_s = 0.26$ cm and the start values were $r_a = 0.3$ cm and

$r_{g,i} = 2.55$ cm. The next iterations followed by increasing r_a by 0.3 cm and decreasing $r_{g,i}$ by 0.3 cm. The last value is $r_a = 2.4$ cm.

As we can see in Fig. 80 the bigger the area of the active electrode the higher capacitance and in Fig. 81 the bigger the capacitance change.

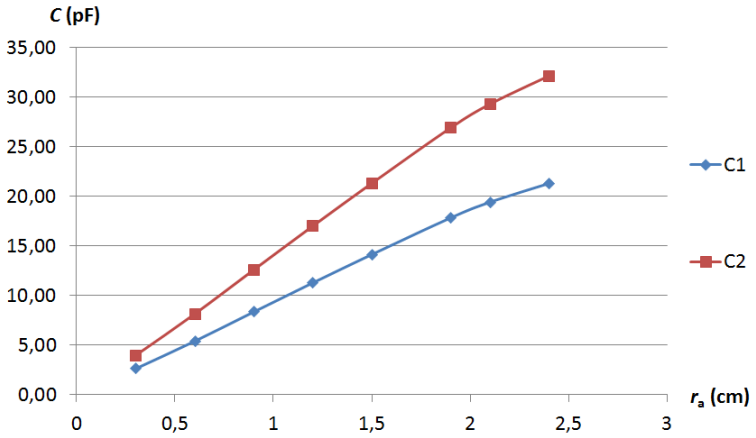

Figure 80: Nominal Capacitance in function of r_a

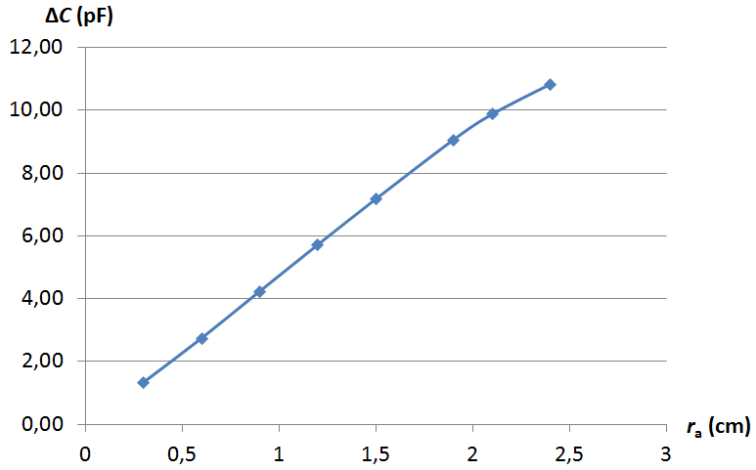

Figure 81: Capacitance change in function of r_a

If we increase the active area maintaining the same separation the number of waves passing through compost is bigger, and since the resin layer effect is kept the same, the capacitance change increases. However, the number of waves does not mind for the capacitance change over the nominal capacitance (Fig. 82) since the effect of the resin layer is still the same. As such, it does not matter how much we increase the area of the active electrode keeping the same separation, that this value will remain the same.

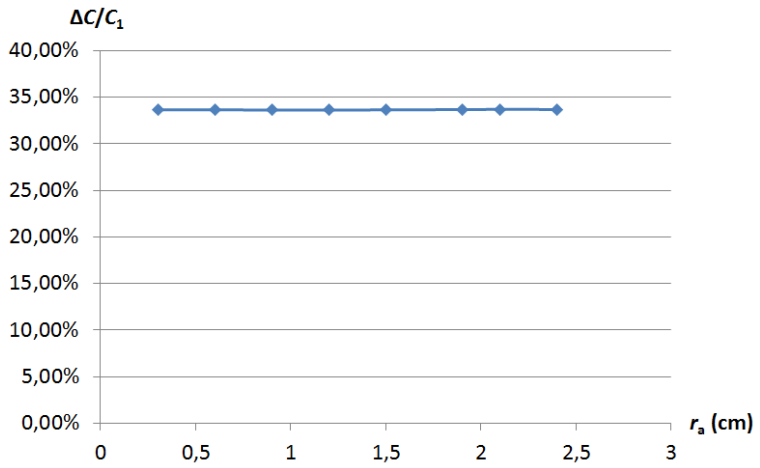

Figure 82: Capacitance change over Nominal Capacitance in function of r_a

THEORETICAL MODEL We can consider that the geometric factor on the capacitance of the electrodes behaves as a Taylor series for each dimension since the behavior per dimensions is not periodic nor complex. As such, we obtain the following equation:

$$C = \varepsilon \cdot K_c \cdot \sum_{n=0}^{\infty} \left(\frac{a_n}{l_s^n} \right) \cdot \sum_{m=0}^{\infty} (b_m \cdot r_a^m) \tag{4.13}$$

If we consider an order 4 (if we take a lower order the error increases and if we take a higher order the error does not improve significantly) and try to get the coeficients with the results from the simulations the folowing is obtained:

n	a_n	b_n
1	$-4.74 \cdot 10^{-4}$	$1.00 \cdot 10^{-10}$
2	$1.67 \cdot 10^{-5}$	$4.41 \cdot 10^{-7}$
3	$-8.51 \cdot 10^{-8}$	$1.39 \cdot 10^{-5}$
4	$1.49 \cdot 10^{-10}$	$-4.56 \cdot 10^{-4}$

Table 22: Coeficient result

With these coeficients and applying Equation (4.13) we obtain the following percentual difference between the simulation value and the theoretical model value, in function of the size of the active electrode and the separation between electrodes.

As we can see the average difference in both cases is more or less around 6 %. It is true that the variation on the separation between electrodes is bigger, this is mainly because when calculating the

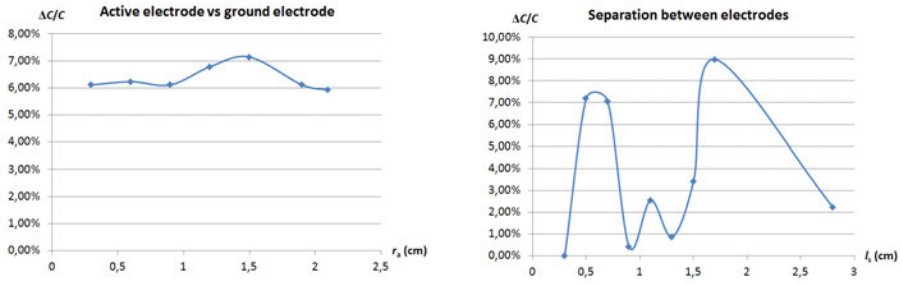

Figure 83: Difference between the concentric simulation and the theoretical model capacitance

coeficients we took as a reference the active electrode vs ground electrode case. If we had taken the separation between electrode case as the reference the opposite would happen.

This error is in line of the current state of the art, where we can find coplanar parallel sensors with a relative error between the theoretical and experimental model inferior to 7.5% [126], or a smaller error for a capacitive cylindric model with more than 3 % error[127].

Interdigital electrodes

The interdigital electrodes (Fig. 75) are two pair of diagonally mirrored electrodes of thickness 1 mm and separated l_s, consisting of a main branch of a width w_{teeth1} and a height of 5.3 cm. From the main branch, a certain number of teeth of length l_{teeth} and width w_{teeth1} grow.

The resin layer and the active shield were 5.3 cm length squares with 1 mm thickness. The reason to choose 5.3 cm of length is to have a similar area to the 6 cm radius concentric electrodes in order to be able to compare them.

The simulations were realized in order to see the performance of the electrodes when varying the separation between electrodes, the length of the teeth and the number of teeth of the electrodes.

As follows, the nominal capacitance of the electrodes, their capacitance change and their capacitance change over the nominal capacitance are calculated in function of the separation between electrodes, the teeth length and the number of teeth.

SEPARATION BETWEEN ELECTRODES (l_s) In this case we simulated the change in capacitance in function of the separation between electrodes (l_s) with 2 teeth per electrode. The size of both electrodes was equally reduced in height and width as the separation increased. The initial values were $l_s = 0.3$ cm, $w_{teeth1} = 1.1$ cm, $w_{teeth2} = 1.1$ cm and $l_{teeth} = 2.8$ cm. In each iteration l_s was increased 0.2 cm, w_{teeth1}

and w_{teeth2} were reduced 0.15 cm, and l_{teeth} was increased 0.1 cm. The last iteration was $l_s = 1.7$ cm.

As in the concentric electrodes, the bigger the separation the lower the nominal capacitance, since the electrode area is being reduced (Fig. 84).

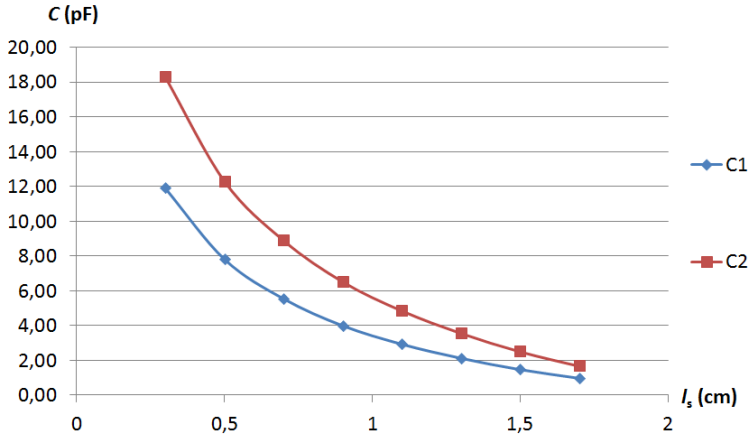

Figure 84: Nominal Capacitance in function of l_{sep}

Also, the same happens to the capacitance change (Fig. 85) but at a lower rate.

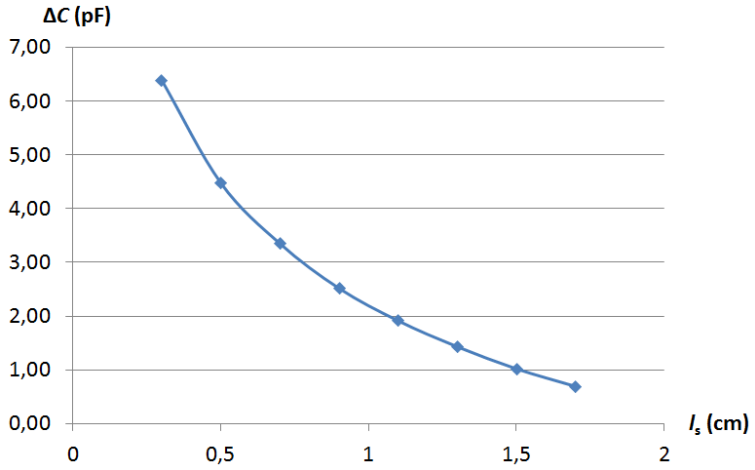

Figure 85: Capacitance change in function of l_{sep}

And as such, the capacitance change over the nominal capacitance improves as the separation increases (Fig. 86). The same effect as the concentric electrodes and for the same reason.

TEETH LENGTH (l_{teeth}) In this case we simulated the change in capacitance in function of the length of the teeth (l_{teeth}) maintaining w_{teeth1} and l_s constant and modifying the width of the main branches.

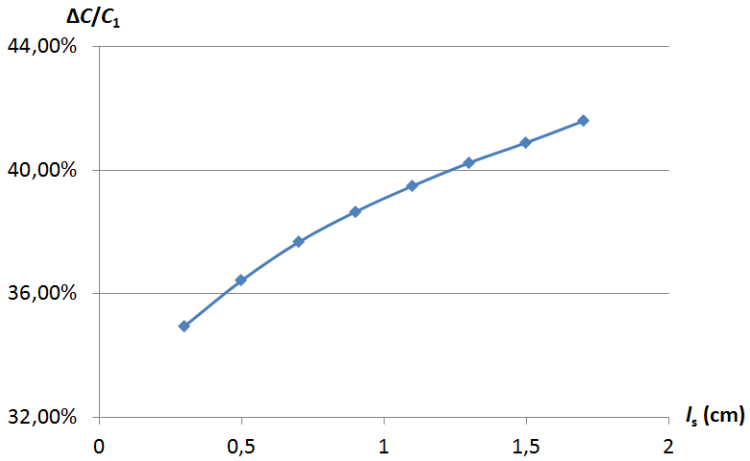

Figure 86: Capacitance change over Nominal Capacitance in function of l_{sep}

The initial values were $l_{teeth} = 0$ cm, $w_{teeth1} = 0.05$ cm, $w_{teeth2} = 1.8$ cm, $l_s = 1.6$ cm and 2 teeth per electrode. In the next iteration l_{teeth} was increased and w_{teeth2} decreased, both by 0.4 cm. The following iterations l_{teeth} was increased and w_{teeth2} decreased, both by 1 cm.

Fig. 87 shows the increase of capacitance when the length of the teeth is decreased, due to the increase of the main branches and hence in the electrode area.

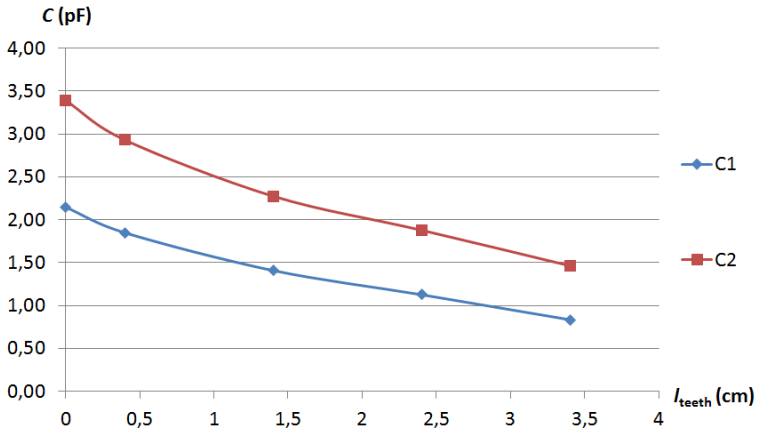

Figure 87: Nominal Capacitance in function of l_{teeth}

For the same reason the capacitance change also increases when the length of the teeth is reduced (Fig. 88) but at a slower rate.

Because of that, the capacitance change over the nominal capacitance increases as the length of the teeth does (Fig. 89).

The reason for that is that as we increase the length of the teeth the main branches w_{teeth2} is decreased, and therefore the separation between the two branches is increased. When the two main

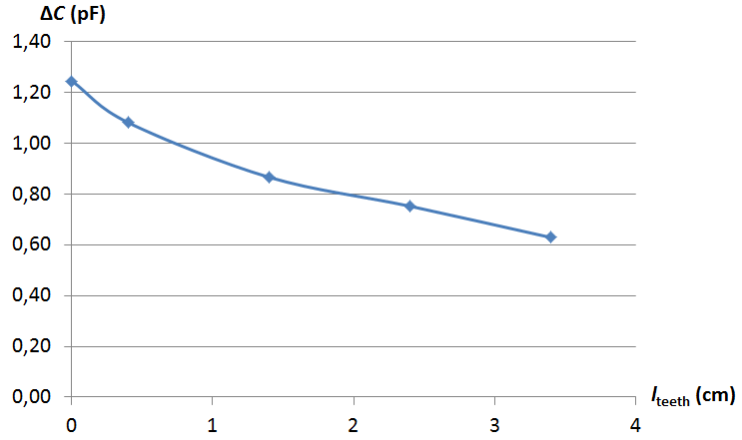

Figure 88: Capacitance change in function of l_{teeth}

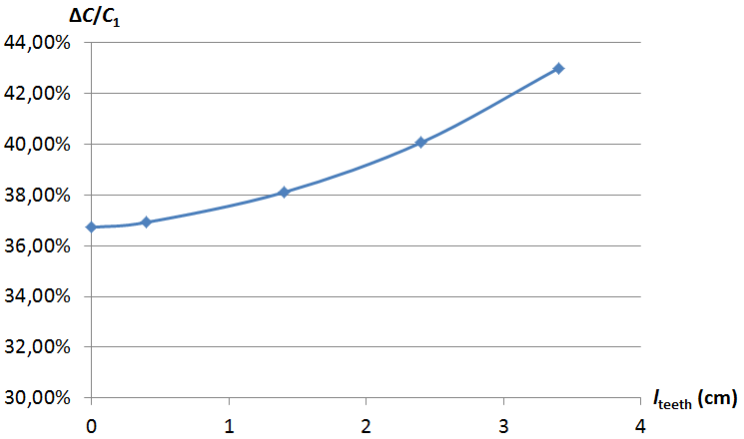

Figure 89: Capacitance change over Nominal Capacitance in function of l_{teeth}

branches are more separated the electromagnetic waves expand and the number of waves filtering through the resin is decreased.

NUMBER OF TEETH (n) In this case we simulated the change in capacitance in function of the number of teeth (N) maintaining l_{teeth}, l_s and w_{teeth2} constant and modifying the width of the teeth w_{teeth1}.

The initial values were $N = 2$, $l_s = 1.7$ cm, $l_{teeth} = 3.7$ cm, $w_{teeth1} = 2.45$ cm and $w_{teeth2} = 1.20$ cm. In each iteration the number of teeth was increased by one and w_{teeth1} evolved as $w_{teeth1} = (5.3 - l_s \cdot (N-1))/N$.

Although the area of the electrodes is smaller the more teeth there are, in Fig. 90 we see that the more teeth the higher the capacitance.

This can be explained as the increase of interaction between electrodes when the number of teeth is increased, and hence the elec-

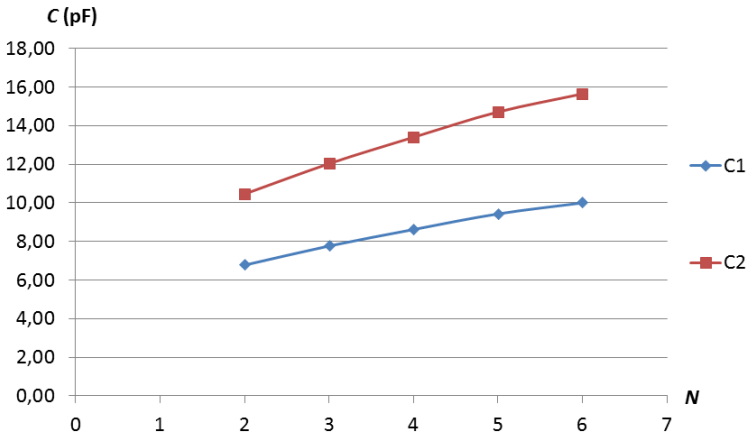

Figure 90: Nominal Capacitance in function of N

tromagnetic waves travel a smaller distance between electrodes and are less attenuated by the environment. Also, since the interaction is increased, the number of waves is increased and as such the sensitivity to changes in permittivity is increased as shown in Fig. 91 and 92.

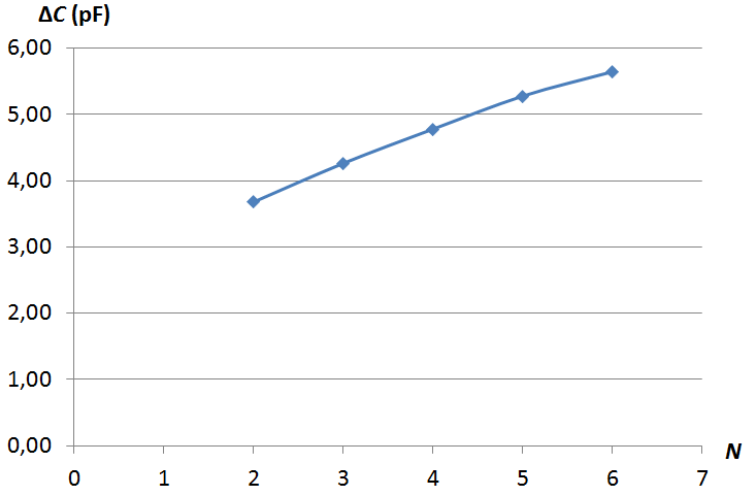

Figure 91: Capacitance change in function of N

THEORETICAL MODEL If we consider that the geometric factor on the capacitance of the electrodes behaves as a Taylor series for each dimension we obtain the following equation:

$$C = \varepsilon \cdot K_c \cdot \sum_{n=0}^{\infty} \left(\frac{x_n}{l_s^n} \right) \cdot \sum_{m=0}^{\infty} \left(y_m \cdot l_{teeth}^m \right) \cdot \sum_{l=0}^{\infty} \left(z_l \cdot \#_{teeth}^l \right) \quad (4.14)$$

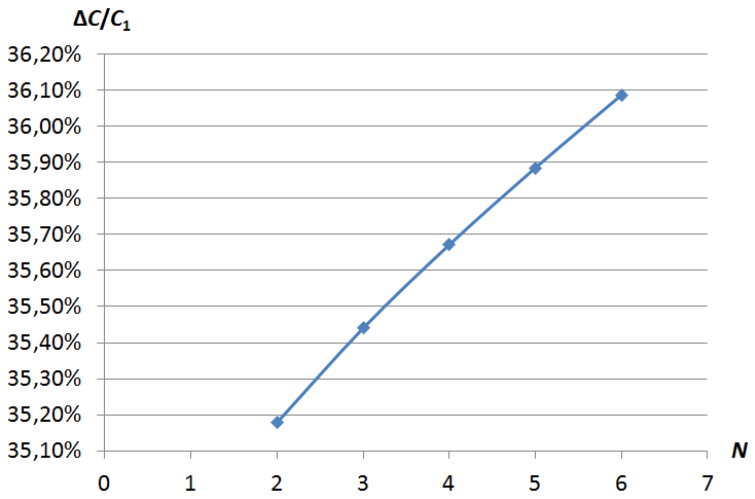

Figure 92: Capacitance change over Nominal Capacitance in function of N

This equation can be compared to Equation (4.8), where the first term can be compared to the Taylor series in function of the length of the teeth and the number of teeth, but we additionally introduce the separation between teeth. The second term in Equation (4.8) introduces a series of relative permitivities for different dielectrics, in our case we consider that the additional materials from the electrodes can be neglected and use a unitary relative permitivity that may or may not be a composition of many dielectrics with the predominant relative permitivity of the material under test.

If we again consider an order 4 and try to get the coeficients with the results from the simulations the folowing is obtained:

n, m, l	x_n	y_m	z_l
1	$-3.15 \cdot 10^{10}$	$1.00 \cdot 10^{-7}$	$1.00 \cdot 10^{-5}$
2	$6.08 \cdot 10^{8}$	$1.64 \cdot 10^{-5}$	$2.05 \cdot 10^{-5}$
3	$2.80 \cdot 10^{6}$	$-9.07 \cdot 10^{-4}$	$7.65 \cdot 10^{-7}$
4	$-6.80 \cdot 10^{3}$	$2.35 \cdot 10^{-2}$	$-1.86 \cdot 10^{-7}$

Table 23: Coeficient result

With these coeficients and applying Equation (4.14) we obtain the following percentual difference between the simulation value and the theoretical model value, in function of the separation between electrodes, the length of the teeth and the number of teeth.

The variable that is affected the most by the error in the theoretical model is the length of the teeth. This is again mainly because we taken as a reference the case of the number of teeth. If the case of the length of the teeth had been the reference the error would had

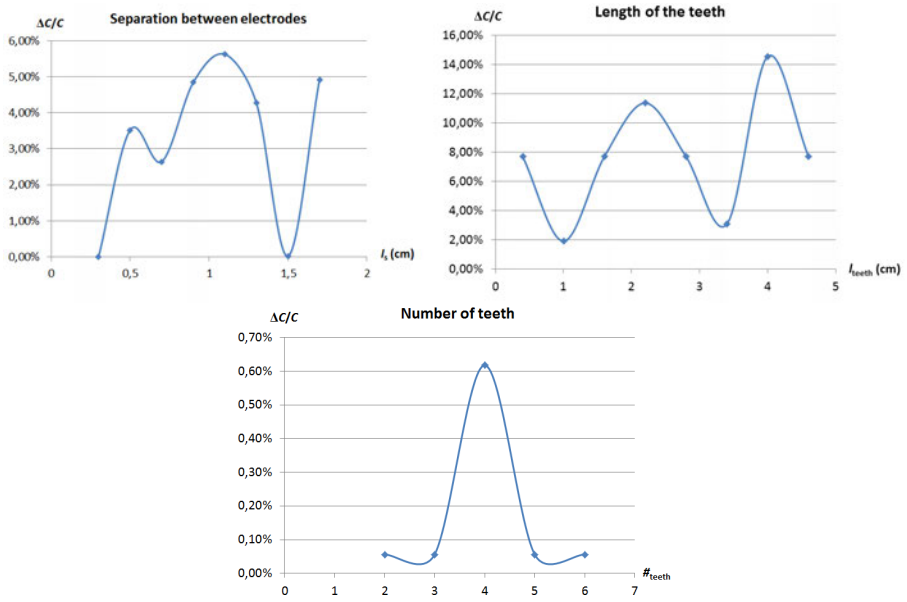

Figure 93: Difference between the interdigital simulation and the theoretical model capacitance

been reduced whilst increasing on the other two cases at the same time. Nevertheless, taking the number of teeth as a reference gives the best overall result.

4.4.4 *Experimental results*

To verify the results obtained from the simulations an experiment was set up. Some electrodes were designed and built based on the design changes of the simulations. The electrode output consisted of an SMA connector to be able to connect it directly to a *Agilent* 42941A Impedance probe for the *Hewlett Packard* 4294A Impedance Analyzer.

The range chosen for the measure of capacitance (C_p: parallel capacitance model) was $f = [30, 40]$ MHz due to inductive effects caused by a parasitic effect of a capacitance to ground. Also this range is useful to minimize the effect of temperature and maximize the effect of humidity in the measure of the impedance[76], from which the analyzer extracts the capacitance. An average was realized from the samples between these two frequencies.

The compost used for the experimental test was obtained from a pile of compost in the curing stage located at the *Parc Mediterrani de la Tecnologia* (PMT) from Castelldefels (Spain) with a 525 kg/m^3 density. This level of density is considered to be from the curing stage and, as such, is considered to be a bad scenario for the measure of capacitance. Still, working with compost in the latest stage is more

comfortable for experimental purposes and more easy to manipulate its characteristics as well. Still, if we obtain positive results with this kind of compost then we can say it will work for earlier compost.

The measure which corresponds to C_1 had a relative humidity of 40.4 %, and the second measure which corresponds to C_2 had a relative humidity of 51.1 %, trying to approximately emulate the permittivity values of the simulation. The measures of humidity were obtained using the *AND* ML-50 Moisture Analyzer.

The dimensions of the compost layer were 6 cm high, 12.7 wide and 22.5 long, contained on a PVC *RS* box.

We will measure these capacitances and apply to them the theoretical model to check the theoretical relation between relative permittivities ($\varepsilon_1/\varepsilon_2$).

Concentric electrodes

The coplanar concentric electrodes (Fig. 94) were designed to measure the changes when modifying the separation between electrodes and the proportion between the sensing and the ground electrode.

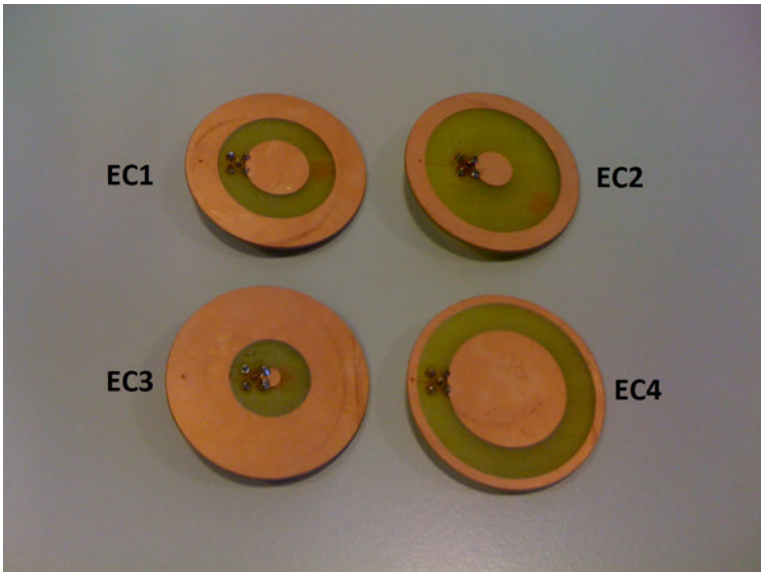

Figure 94: Experimental concentric electrodes

The dimensions of electrodes EC1 and EC2 were $r_a = 1.05$ cm, $r_{g,i} = 1.95$ cm and $r_a = 0.65$ cm, $r_{g,i} = 2.35$ cm, respectively. The separation was 0.9 cm for EC1 and 1.7 cm for EC2. The performance of the nominal capacitance of the electrodes, their capacitance change and their capacitance change over the nominal capacitance in function of the separation between electrodes can be seen in Table 24.

If we now apply the theoretical model we obtain Table 25.

l_{sep}	C_1 (pF)	C_2 (pF)	$\triangle C$ (pF)	$\triangle C/C_1$ (%)
0.9 cm	7.49	13.30	5.81	77.60
1.7 cm	6.78	12.20	5.42	80.00
$l_{sep} \uparrow$	$\downarrow$	$\downarrow$	$\downarrow$	$\uparrow$

Table 24: Concentric electrodes experimental performance in function of l_{sep}

l_{sep}	C_1 (pF)	$\varepsilon_1 \cdot k_c$	C_2 (pF)	$\varepsilon_2 \cdot k_c$	$\varepsilon_1/\varepsilon_2$
0.9 cm	7.49	2.45	13.30	4.35	0.56
1.7 cm	6.78	8.15	12.20	14.70	0.56

Table 25: Theoretical model applied to the experimental performance in function of l_{sep}

The dimensions of electrodes EC3 and EC4 were $l_{sep} = 0.9$ cm, $r_{g,i} = 1.05$ cm and $l_{sep} = 0.9$ cm, $r_{g,i} = 1.8$ cm, respectively. The radius of the sensing electrode was 0.3 cm for EC3 and 1.8 cm for EC4. The performance of the nominal capacitance of the electrodes, their capacitance change and their capacitance change over the nominal capacitance in function of the active electrode radius can be seen in Table 26.

r_a	C_1 (pF)	C_2 (pF)	$\triangle C$ (pF)	$\triangle C/C_1$ (%)
0.3 cm	8.27	10.60	2.37	28.70
1.8 cm	8.69	11.20	2.49	28.70
$r_a \uparrow$	$\uparrow$	$\uparrow$	$\uparrow$	=

Table 26: Concentric electrodes experimental performance in function of r_a

If we now apply the theoretical model we obtain Table 27.

r_a	C_1 (pF)	$\varepsilon_1 \cdot k_c$	C_2 (pF)	$\varepsilon_2 \cdot k_c$	$\varepsilon_1/\varepsilon_2$
0.3 cm	8.27	2.95	10.60	3.78	0.78
1.8 cm	8.69	0.46	11.20	0.59	0.78

Table 27: Theoretical model applied to the experimental performance in function of r_a

As can be seen the behavior of modifying the separation or the proportion in the sizes between the sensing and the ground electrodes, is the same as seen in the simulations. The nominal capacitance is

higher in the experimental case since the density of the compost is much higher, hence the slope of the humidity/permittivity line is higher the higher the density.

We can also see that for each case the relation $\varepsilon_1/\varepsilon_2$ from the theoretical model is fulfilled, but when comparing both cases there is a difference in the relation. Let's analyze the interdigital electrodes to see if this difference is consistent or isolated.

Interdigital electrodes

The coplanar interdigital electrodes (Fig. 95) were designed to measure the changes when modifying the separation between electrodes, the length of their teeth and the number of teeth.

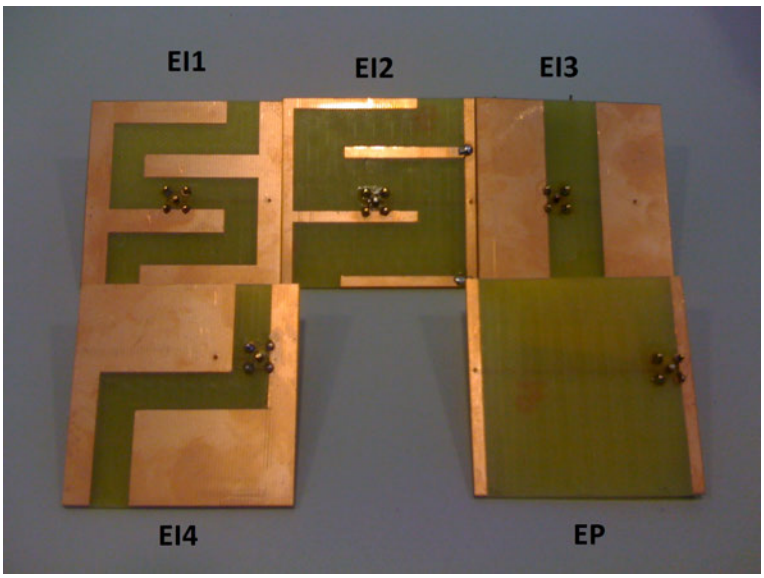

Figure 95: Experimental interdigital electrodes

The dimensions of electrodes EI1 and EI2 were $w_{teeth_1} = 0.65$ cm, $w_{teeth_2} = 0.65$ cm, $l_{teeth} = 3.1$ cm and $w_{teeth_1} = 0.3$ cm, $w_{teeth_2} = 0.3$ cm, $l_{teeth} = 3.4$ cm, respectively. The separation was 0.9 cm for EI1 and 1.5 cm for EI2. The performance of the nominal capacitance of the electrodes, their capacitance change and their capacitance change over the nominal capacitance in function of the separation between electrodes can be seen in Table 28.

If we now apply the theoretical model we obtain Table 29.

The dimensions of electrodes EI3 were $w_{teeth_2} = 1.9$ cm, $l_s = 1.5$ cm. The length of the teeth was 0 cm for EI3 and 3.4 cm for EI2. The performance of the nominal capacitance of the electrodes, their capacitance change and their capacitance change over the nominal capacitance in function of the teeth length can be seen in Table 30.

If we now apply the theoretical model we obtain Table 31.

l_s	C_1 (pF)	C_2 (pF)	$\triangle C$ (pF)	$\triangle C/C_1$ (%)
0.9 cm	6.99	12.10	5.14	73.60
1.5 cm	5.28	9.43	4.14	78.40
$l_s \uparrow$	$\downarrow$	$\downarrow$	$\downarrow$	$\uparrow$

Table 28: Interdigital electrodes experimental performance in function of l_s

l_s	C_1 (pF)	$\varepsilon_1 \cdot k_c$	C_2 (pF)	$\varepsilon_2 \cdot k_c$	$\varepsilon_1/\varepsilon_2$
0.9 cm	6.99	1.84	12.10	3.19	0.58
1.5 cm	5.28	3.59	9.43	6.41	0.56

Table 29: Theoretical model applied to the experimental performance in function of l_s

l_{teeth}	C_1 (pF)	C_2 (pF)	$\triangle C$ (pF)	$\triangle C/C_1$ (%)
0 cm	6.37	9.47	3.11	48.80
3.5 cm	5.28	9.43	4.14	78.40
$l_{teeth} \uparrow$	$\downarrow$	$\downarrow$	$\downarrow$	$\uparrow$

Table 30: Interdigital electrodes experimental performance in function of l_{teeth}

l_{teeth}	C_1 (pF)	$\varepsilon_1 \cdot k_c$	C_2 (pF)	$\varepsilon_2 \cdot k_c$	$\varepsilon_1/\varepsilon_2$
0 cm	6.37	28.3	9.47	42.1	0.67
3.5 cm	5.28	4.42	9.43	7.90	0.56

Table 31: Theoretical model applied to the experimental performance in function of l_{teeth}

The dimensions of EI4 were $l_{teeth} = 3.1$ cm, $w_{teeth1} = 2.2$ cm, $w_{teeth2} = 0.65$ cm, $l_s = 0.9$ cm. The number of teeth was 2 for EI4 and 4 for EI1. The performance of the nominal capacitance of the electrodes, their capacitance change and their capacitance change over the nominal capacitance in function of the number of teeth can be seen in Table 32.

If we now apply the theoretical model we obtain Table 33.

The same behavior as in the simulations is confirmed.

As for the application of the theoretical model we see that case to case there is a difference in the $\varepsilon_1/\varepsilon_2$ relation.

$\#_{teeth}$	C_1 (pF)	C_2 (pF)	$\triangle C$ (pF)	$\triangle C/C_1$ (%)
2	6.79	10.40	3.58	52.80
4	6.99	12.10	5.14	73.60
$\#_{teeth} \uparrow$	$\uparrow$	$\uparrow$	$\uparrow$	$\uparrow$

Table 32: Interdigital electrodes experimental performance in function of $\#_{teeth}$

$\#_{teeth}$	C_1 (pF)	$\varepsilon_1 \cdot k_c$	C_2 (pF)	$\varepsilon_2 \cdot k_c$	$\varepsilon_1/\varepsilon_2$
2	6.79	1.00	10.40	1.53	0.65
4	6.99	0.81	12.10	1.40	0.58

Table 33: Theoretical model applied to the experimental performance in function of $\#_{teeth}$

4.4.5 *Conclusions*

We have successfully simulated and tested experimentally the behavior of nominal capacitance, capacitance change and capacitance change over capacitance, when modifying dimensions in interdigital and concentric coplanar electrodes.

To check the consistency of our theoretical models, we have applied them to the experimental results and have obtained the relation $\varepsilon_1/\varepsilon_2$ for all cases. This relation should be the same value and the application of the theoretical model will give us an idea of how good this model is for real experiments. In Figure 96 we show the histogram for the values obtained of the $\varepsilon_1/\varepsilon_2$ relation.

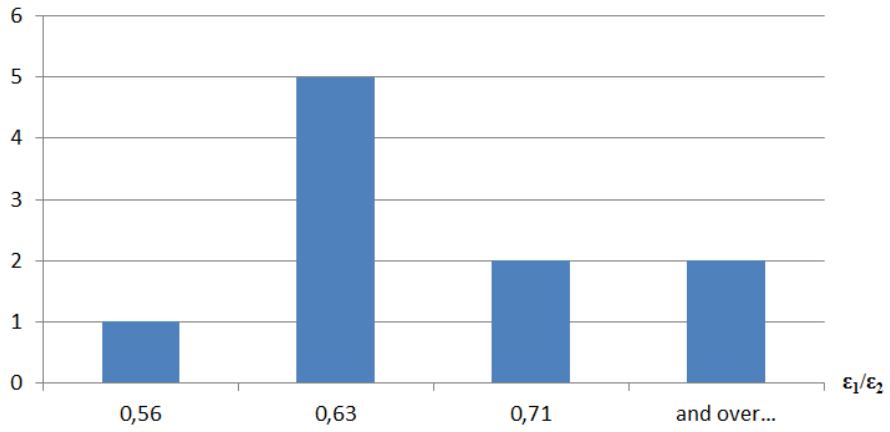

Figure 96: Histogram of the $\varepsilon_1/\varepsilon_2$ relation of the theoretical model applied to all the experimental cases

The average of the values is around 0.63 and the standard deviation 0.08. If we calculate the standard error of the mean we obtain 2.82 % which gives us a good feeling of the consistency of the theoretical model when using it on our theoretical models for concentric and interdigital electrodes.

On the other hand, the following recommendations for the design of electrodes where obtained from the behavior of the electrodes:

If we were interested in **an application that needs a minimum value of capacitance** and/or **an application in which the predominant disturbance is the noise of the system** (is not affected by the uncertainty in the material composition), we can use concentric electrodes to have the biggest nominal capacitance (C) and/or the biggest sensitivity ($\triangle C$) respectively. For both cases we need to decrease the separation between electrodes and to make the sensing electrode much bigger than the ground electrode.

If we were interested in **avoiding corner effects**, regardless of the nominal capacitance (C) and the sensitivity ($\triangle C$), we should use concentric electrodes maximizing the relative sensitivity ($\triangle C/C_1$), increasing the separation as much as possible.

Since we are interested in **an application in which the predominant disturbance is the inaccuracy due to the heterogeneity of the material**, we will use interdigital electrodes to have the biggest relative sensitivity ($\triangle C/C_1$). In that case we need to increase the separation between electrodes, the length of the teeth and the number of teeth.

If we were able to **choose the size of the electrodes**, then we should have chosen to make them as big as possible, not only to increase their nominal capacitance (C), but also their sensitivity ($\triangle C$).

Also we could have played and **mix characteristics** of electrodes by designing hybrids electrodes, e.g. a concentric interdigital electrode to avoid corner effects and to increase the relative sensitivity as much as possible.

4.5 MULTILAYER COPLANAR CAPACITIVE ELECTRODES

Dielectric materials play an extensive role in both industrial applications and scientific research areas. Due to the need of electric component miniaturization in modern integrated circuit industry, there are palpable needs for dielectric measurements of low-loss thin materials [105].

One important and practical field of material dielectric property characterization is dielectrometry, which derives the complex permit-

tivity of a test-piece from the measured sensor capacitance. Sensors based in coplanar capacitive electrodes are widespread among the most commonly used. Recent advances in such fields as nondestructive testing (NDT), microelectromechanical systems (MEMS), telecommunications, chemical sensing, piezoacoustics, and biotechnology involve coplanar capacitive electrodes in very different ways [76].

The most famous shape through history for coplanar capacitive electrodes is the interdigital electrode design, the earliest example is found in the patent of N. Tesla in 1891 [94]. And its theoretical expressions for the calculation of their capacitance appeared in the 20s [95]. A part of coplanar interdigital electrodes the next more used shape is the concentric electrode. As said before this shape is not as old as interdigital but their use has been extended up to these days [105]. Their advantages and disadvantages compared to the interdigital are not really analyzed in the bibliography. As in the interdigital case, there is poor research on the specific optimization of shape and dimensions and so it is something else to take into account.

Most of the analysis involving the use of this sensors do not take into account the heterogeneity of the dielectric materials or the use of thin protective layers. Full wave analysis of interdigital capacitors on heterogeneous or multilayer substrates is a complex computational problem [9]. But multilayered models have been studied for many years looking for the optimal theoretical model [10, 11].

Similarly to the previous section, we will present an optimization of the shape and dimensions of interdigital and concentric coplanar capacitive electrodes but, in this case, using a multilayer dielectric. As follows, a research of the theoretical models found in the state of the art are analyzed. Then different configurations for interdigital and concentric coplanar electrodes are simulated to see the behavior in function of the dimensions and shape. Then, those configurations were experimentally tested and some conclusions and design recommendations were finally extracted.

4.5.1 *Theoretical models*

The available analytical solutions [12, 13] are limited to homogeneous substrates and equal finger and slot widths. Lately, simple

formulas have been proposed for IDC with a dielectric layer on top of thin conducting strips [11].

$$C = 2\varepsilon_0\varepsilon_e \left[\frac{K(k_3)}{K(k_3')} + \frac{K(k_4)}{K(k_4')} \right] \tag{4.15}$$

where ε_0 is the relative permittivity of the air, ε_e is the effective permittivity of the multilayer, and $K(k_3)$ is the complete elliptic integrals of k_3 (dependent on the physical dimensions from region 3 of the electrodes), $K(k_4)$ of k_4 region 4 (dependent on the physical dimensions from region 4 of the electrodes), $k_3' = \sqrt{1-k_3^2}$ and $k_4' = \sqrt{1-k_4^2}$.

These formulas do not take into account the fringing field of the finger ends, and lead to higher capacitances in comparison with the widely used formulas [12, 13].

The processing of such complex theoretical models require heavy computational work that would imply spending great effort and time in something that can be easily done using simulation tools. Also, taking into account the inaccuracy of approximated calculations we decided simulating the different electrode configurations in order to have the highest accuracy with the minimum complexity. Moreover, whilst there are different theoretical models for each shape, the simulation process is the same.

In the case of concentric capacitive electrodes, the transcapacitance C_T between the two electrodes, can be calculated through [105]

$$C_T = \left. \frac{Q_{outer}}{V_{inner}} \right|_{V_{outer}=0} \tag{4.16}$$

where Q_{outer} is the total charge on the outer electrode, while V_{inner} and V_{outer} respectively represent the voltage on the inner and outer electrodes. The total charge, on both inner and outer electrodes, can be found integrating over the electrode surfaces with the surface charge distribution $\sigma(\rho')$. In order to calculate the surface charge distribution, Green's functions [6] for the method of moments (MoM) [7] are used. We have to take into account that the method of moments is used in simulation tools, and hence we see that for complex theoretical models in the case of concentric capacitive electrodes the option is also simulating. On the other hand the voltage V_{inner} is obtained discretizing an integral equation using weighting functions in each of the N dielectric layers.

Considering all previous models we will work with simulations to fulfill our objective of finding the design optimization for interdigital and concentric electrodes.

4.5.2 *Simulation*

The same technical specifications were used as previously for all simulations

Concentric electrodes inside ball

The concentric electrodes consisted of an active circular electrode of radius r_a and width 1 mm, surrounded by a ground ring electrode of outer radius of 3 cm, inner radius $r_{g,i}$ and width 1 mm. The resin layer and the active shield were 6 cm radius circles with 1 mm width.

The electrodes were surrounded by a 9 cm diameter polyurethane sphere (relative permittivity of 3.3 [63]). This sphere was plain on an extreme cutting off a 1/4 part of the total area, and the electrode was placed 3 mm under this plane cut inside the polyurethane protection (Fig. 97).

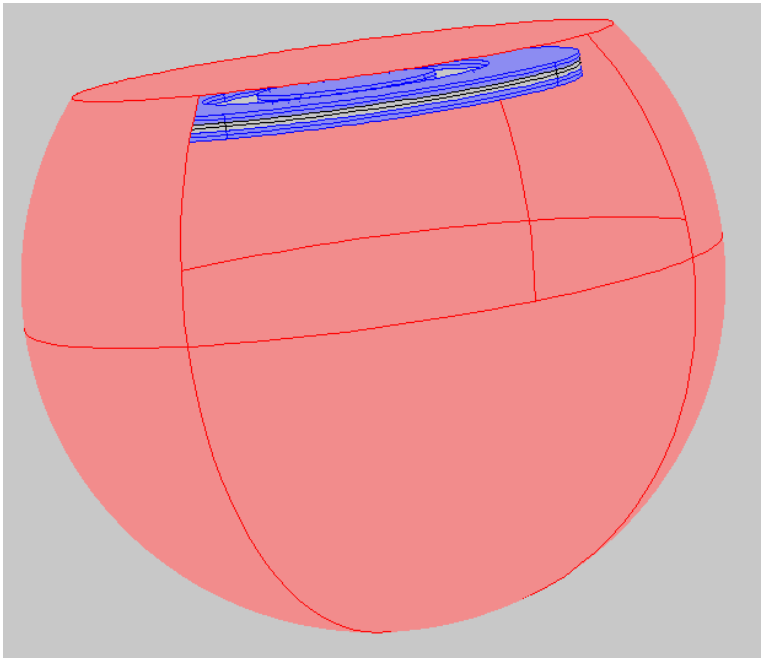

Figure 97: 3D Concentric electrodes inside ball

The simulations were realized in order to see the performance of the electrodes when varying the separation between electrodes or the size of one electrode respect to the others.

SEPARATION BETWEEN ELECTRODES (l_{sep}) In this case we simulated the change in capacitance in function of the separation between electrodes ($l_{sep} = r_{g,i} - r_a$). The size of both electrodes was equally reduced as the separation increased. Their start values for $l_{sep} = 0.3$ cm were $r_a = 1.35$ cm and $r_{g,i} = 1.35$ cm. The subsequent iterations followed by increasing l_{sep} by 0.2 cm, and reducing r_a and $r_{g,i}$ by 0.1 cm. The penultimate value was $l_{sep} = 1.7$ cm and then a jump is made with a final simulation with $l_{sep} = 2.8$ cm.

From Fig. 98 we obtain that if you want to increase the nominal value of capacitance you need to reduce the separation between electrodes. This is logical since what we are doing is increasing the size of the electrodes.

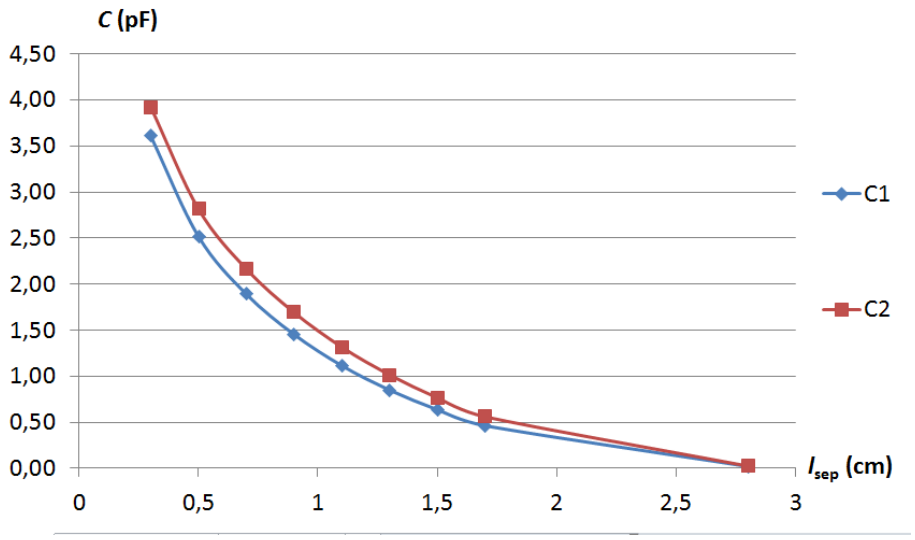

Figure 98: Nominal Capacitance change in function of l_{sep}

In Fig. 99 we see that the smaller the separation between electrodes, the bigger is the capacitance change.

And from Fig. 100 we see that if you want to maximize the capacitance change over the nominal capacitance you have to increase the separation. If the electrodes are too close from each other, the electromagnetic waves concentrate inside the layer of polyurethane and the layer of resin and hence we lose sensitivity.

There is a moment in which we cannot improve anymore and the increasing of the separation becomes harmful. This may come from the moment no electromagnetic field remains inside the polyurethane layer, and thus if we increase the separation we reduce the size of the electrodes and have the same effect as in Fig. 98 and 99.

ACTIVE ELECTRODE VS GROUND ELECTRODE In these simulations we measured the change in capacitance in function of the

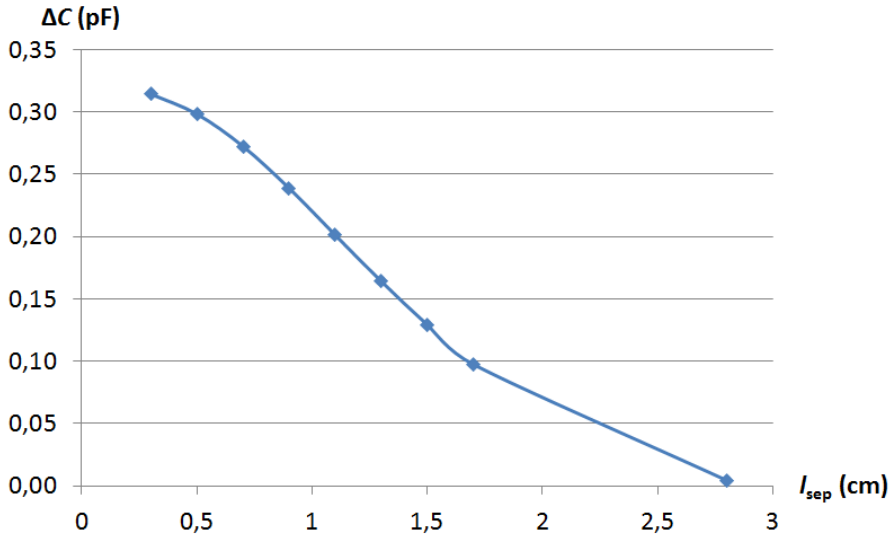

Figure 99: Capacitance change in function of l_{sep}

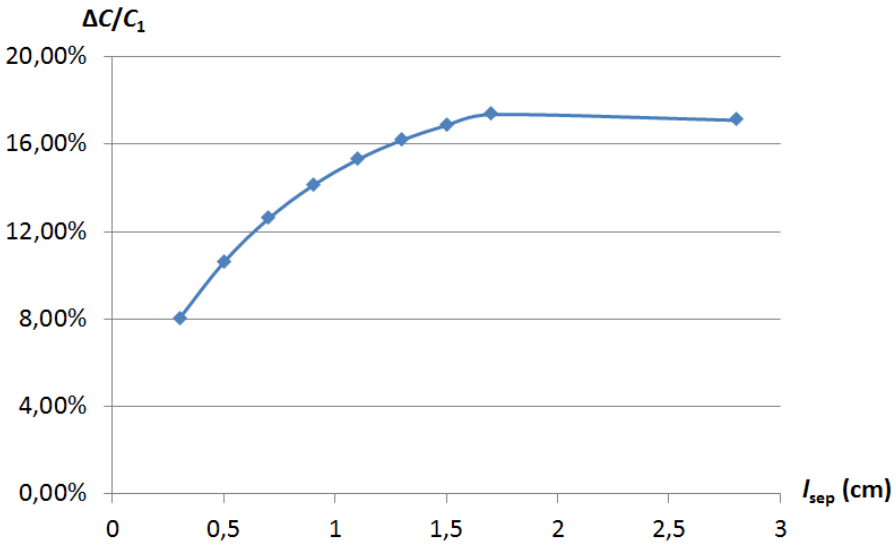

Figure 100: Capacitance change over Nominal Capacitance in function of l_{sep}

size of the active electrode. The separation between electrodes was fixed as $l_{sep} = 0.15$ cm and the start values were $r_a = 0.3$ cm and $r_{g,i} = 2.55$ cm. The next iterations followed by increasing r_a by 0.3 cm and decreasing $r_{g,i}$ by 0.3 cm. The last value is $r_a = 2.4$ cm.

As we can see in Fig. 101 the bigger the area of the active electrode the higher the capacitance. If we increase the active area maintaining the same separation the number of waves passing through compost is bigger, and since the resin layer effect is kept the same, the capacitance change increases.

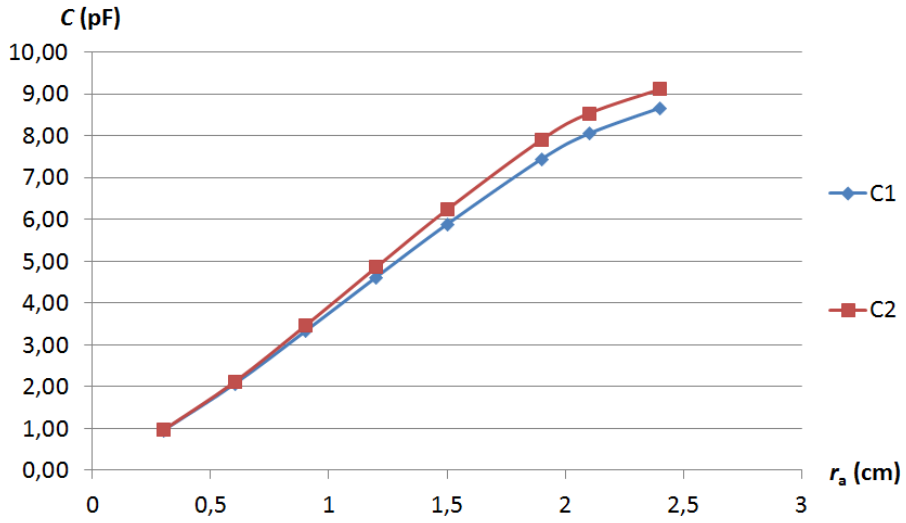

Figure 101: Nominal Capacitance in function of r_a

The same happens with the capacitance change (Fig. 102) except for some values in which the ground electrode must so small that the waves need to find other ways into it as around the protection.

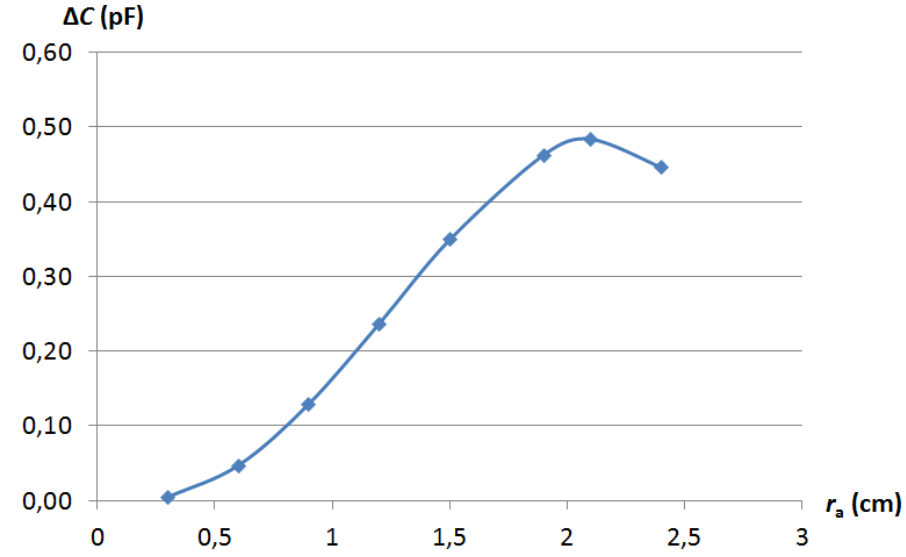

Figure 102: Capacitance change in function of r_a

The nominal capacitance over the capacitance change also increases as the area of the active electrode does (Fig. 103). This may be due to the increase of electromagnetic waves that are not confined inside the protection as the active electrode increases. Also, in the same way as in the capacitance change at the end the effect of increasing the active electrode is counterproductive.

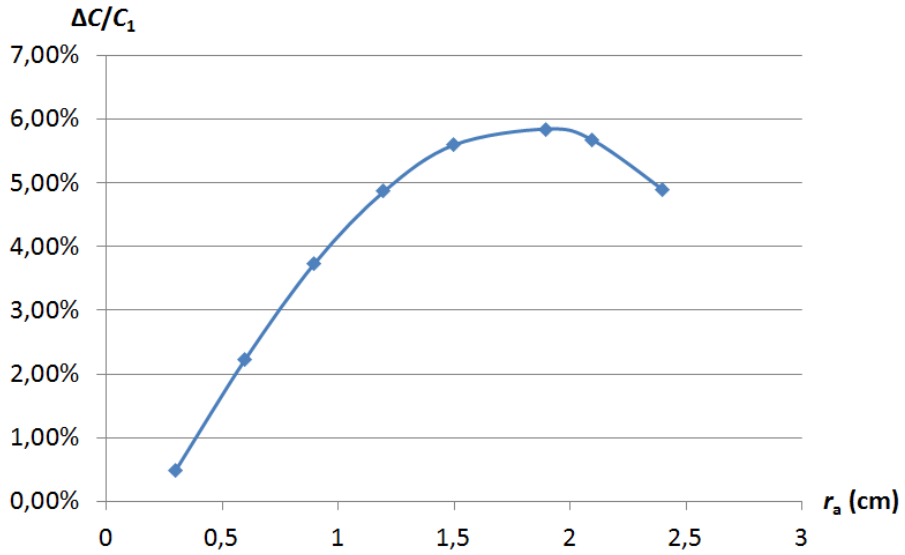

Figure 103: Capacitance change over Nominal Capacitance in function of r_a

Interdigital electrodes inside ball

The interdigital electrodes are two pair of diagonally mirrored electrodes of thickness 1 mm and separated l_s, consisting of a main branch of a width w_{teeth1} and a height of 5.3 cm. From the main branch, two teeth of length l_{teeth} and width w_{teeth1} grow.

The resin layer and the active shield were 5.3 cm length squares with 1 mm width. The reason to choose 5.3 cm of length is to have a similar area to the 6 cm radius concentric electrodes in order to be able to compare them.

The simulations were realized in order to see the performance of the electrodes when varying the separation between electrodes, the length of the teeth and the number of teeth of the electrodes.

In the same way as in the concentric electrodes, the interdigital electrodes were simulated inside a polyurethane protection (Fig. 104) to see how the optimization changes.

SEPARATION BETWEEN ELECTRODES (l_s) In this case we simulated the change in capacitance in function of the separation between electrodes (l_s). The size of both electrodes was equally reduced in height and width as the separation increased. The initial values were $l_s = 0.3$ cm, $w_{teeth1} = 1.1$ cm, $w_{teeth2} = 1.1$ cm and $l_{teeth} = 2.8$ cm. In each iteration l_s was increased 0.2 cm, w_{teeth1} and w_{teeth2} were reduced 0.15 cm and l_{teeth} was increased by 0.1 cm. The last iteration was $l_s = 1.7$ cm.

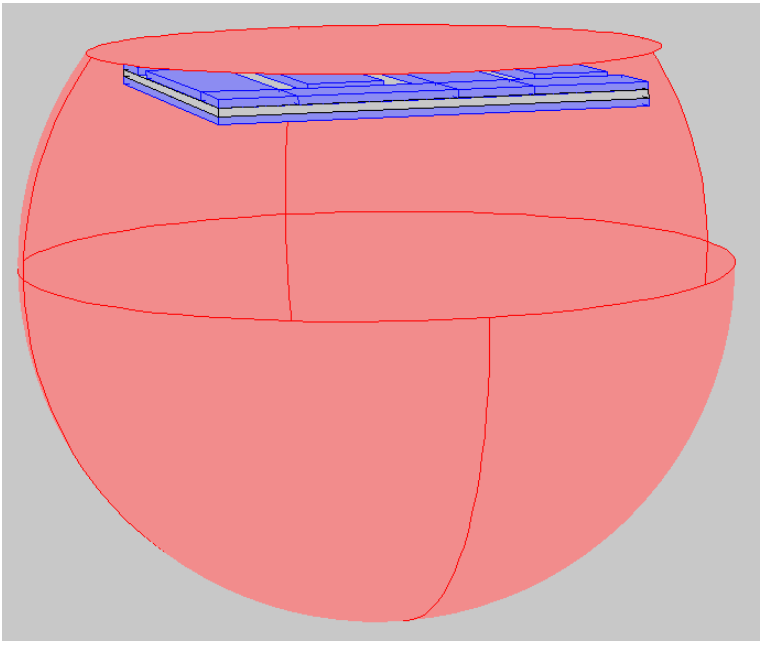

Figure 104: 3D Interdigital electrodes inside ball

As always, the bigger the separation the lower the nominal capacitance due to the reduction of area (Fig. 105).

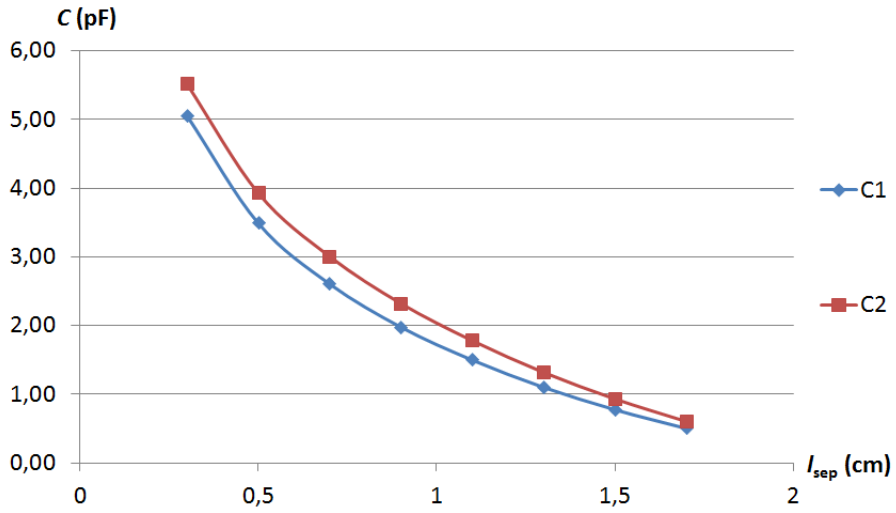

Figure 105: Nominal Capacitance in function of l_{sep}

Also, the same happens to the capacitance change (Fig. 106) but at a lower rate.

The capacitance change over the nominal capacitance improves as the separation increases (Fig. 107). The effect of the resin layer and the polyurethane layer diminishes as the electromagnetic fields expand through the compost when the separation is increased.

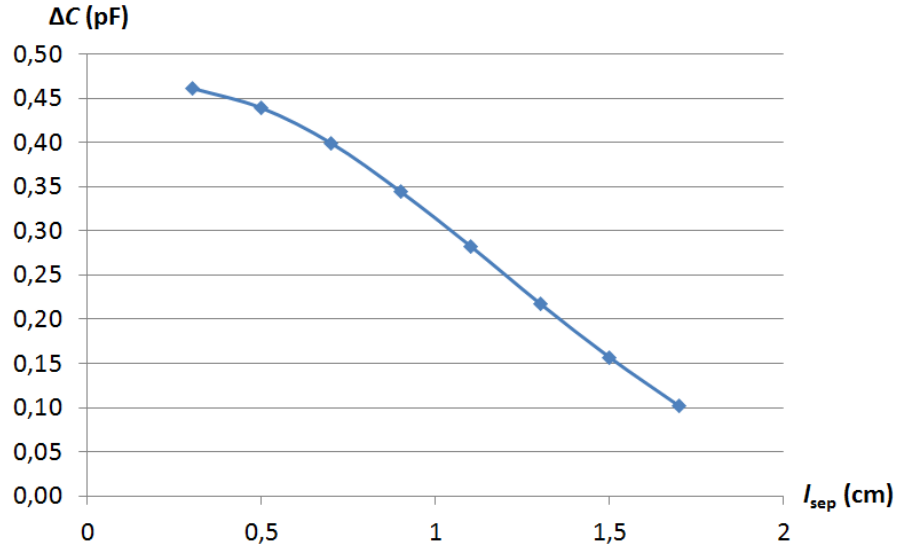

Figure 106: Capacitance change in function of l_{sep}

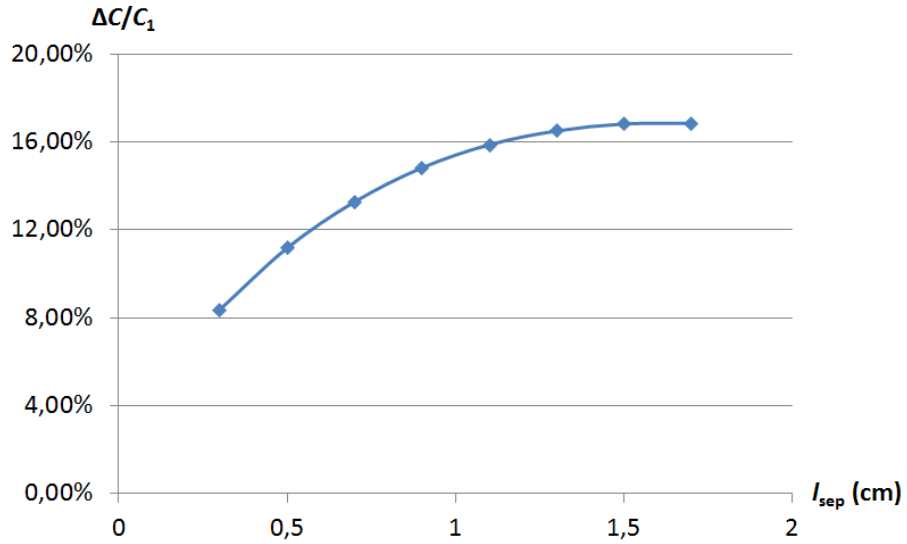

Figure 107: Capacitance change over Nominal Capacitance in function of l_{sep}

TEETH LENGTH (l_{teeth}) In this case we simulated the change in capacitance in function of the length of the teeth (l_{teeth}) maintaining w_{teeth1} and l_s constant and modifying the width of the main branches.

The initial values were $l_{teeth} = 0$ cm, $w_{teeth1} = 0.05$ cm, $w_{teeth2} = 1.8$ cm and $l_s = 1.7$ cm. In the next iteration l_{teeth} was increased and w_{teeth2} decreased, both by 0.4 cm. The following iterations l_{teeth} was increased and w_{teeth2} decreased, both by 1 cm.

Fig. 108 shows the increase of capacitance when the length of the teeth is decreased, due to the increase of the main branches and hence in the electrode area.

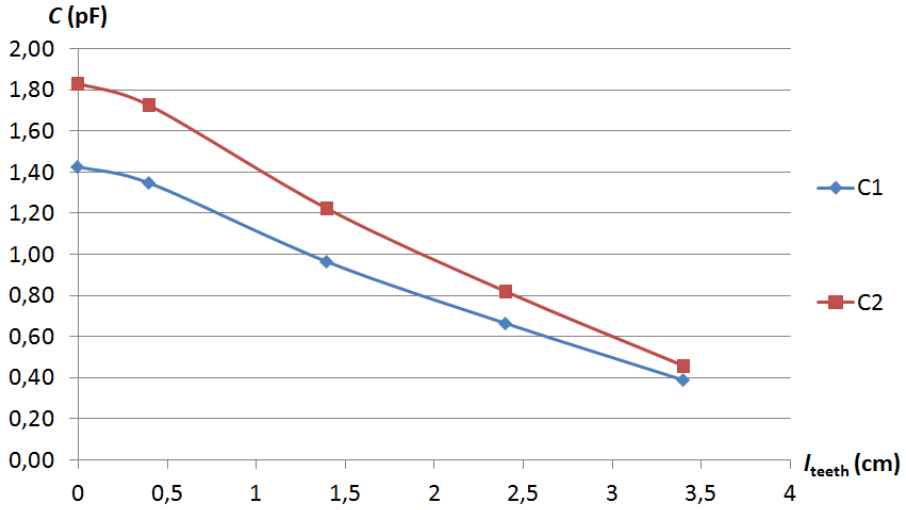

Figure 108: Nominal Capacitance in function of l_{teeth}

For the same reason the capacitance change also increases when the length of the teeth is reduced (Fig. 109).

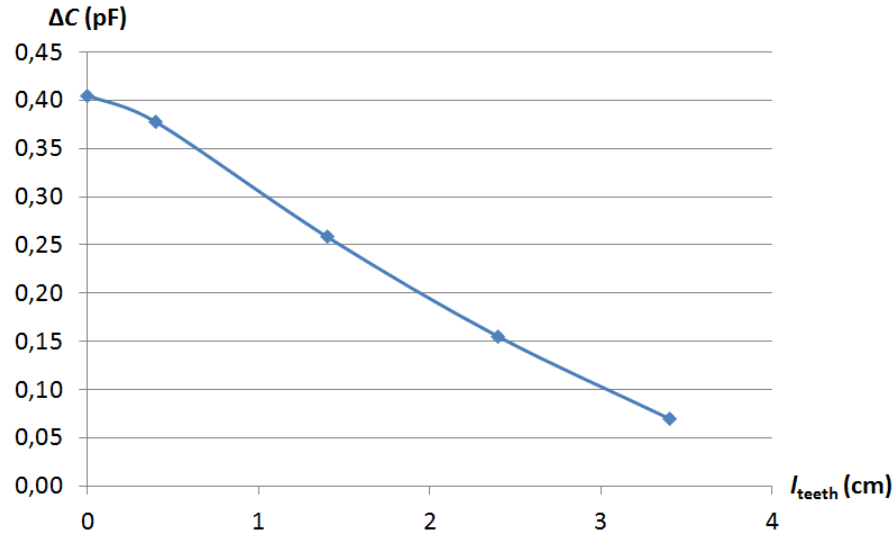

Figure 109: Capacitance change in function of l_{teeth}

The difference appears when looking at the nominal capacitance over the capacitance change (Fig. 110) where it decreases as the teeth length increases. The decrease in the width of the main branches makes the electromagnetic waves to look for other ways around the protection to arrive to ground electrode.

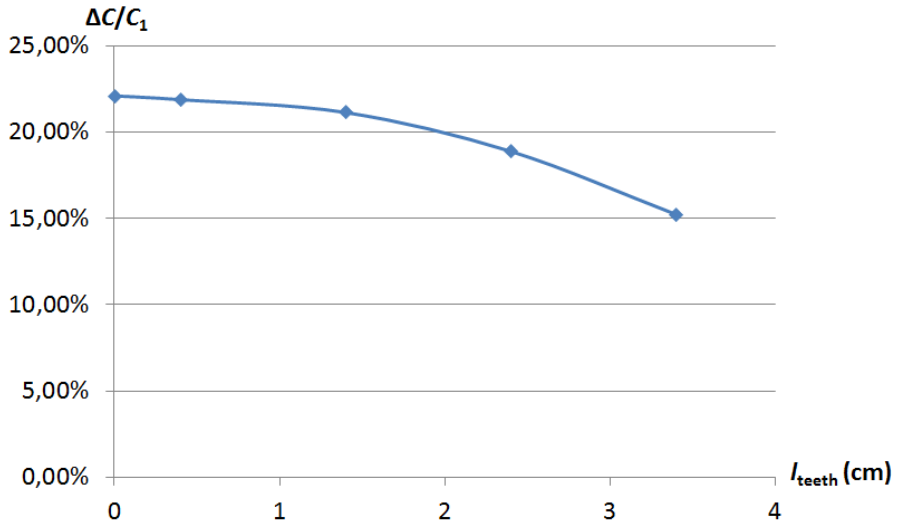

Figure 110: Capacitance change over Nominal Capacitance in function of l_{teeth}

NUMBER OF TEETH (n) In this case we simulated the change in capacitance in function of the number of teeth (N) maintaining l_{teeth}, l_s and w_{teeth2} constant and modifying the width of the teeth w_{teeth1}.

The initial values were $N = 2$, $l_s = 0.4$ cm, $l_{teeth} = 3.7$ cm, $w_{teeth1} = 2.45$ cm and $w_{teeth2} = 1.20$ cm. In each iteration the number of teeth was increased by one and w_{teeth1} evolved as $w_{teeth1} = (5.3 - l_s \cdot (N - 1))/N$.

Although the area of the electrodes is smaller the more teeth there are, in Fig. 111 we see that the more teeth the higher the capacitance. This can be explained as the increase of interaction between electrodes when the number of teeth is increased, and hence the electromagnetic waves travel a smaller distance between electrodes and are less attenuated by the environment.

The difference appears when looking at the change in capacitance and the change in capacitance over the nominal capacitance in Fig. 112 and Fig. 113 respectively, that decrease the more teeth there are.

Since the distance the electromagnetic waves travel decreases the more teeth there are, the more the waves are confined into the protection, and so the sensitivity to changes decreases.

Coplanar parallel electrodes inside ball

For the measuring of permittivity changes in compost from the inside of a protection we have seen that interdigital electrodes have higher values of capacitance change and capacitance over capacitance change (Table 34) than concentric electrodes. And the opposite happens for the nominal capacitance.

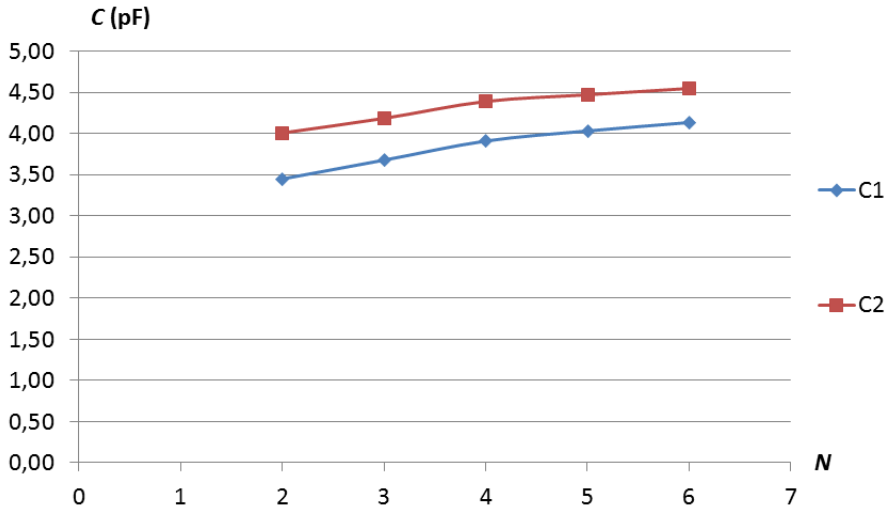

Figure 111: Nominal Capacitance in function of N

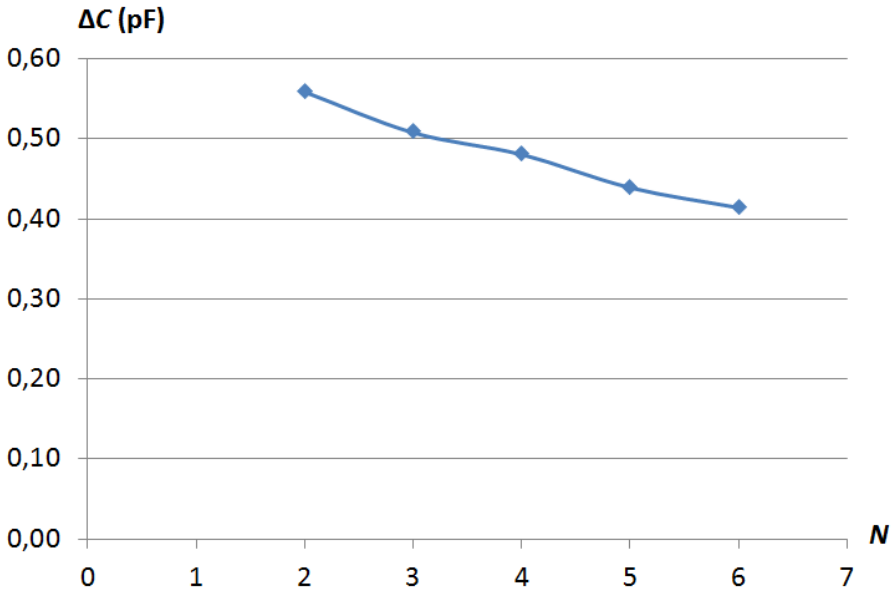

Figure 112: Capacitance change in function of N

Maximum values	Concentric	Interdigital
Nominal Capacitance	9 pF	5.5 pF
Capacitance change	0.49 pF	0.55 pF
Nominal Capacitance over Capacitance change	0.17	0.22

Table 34: Interdigital vs Concentric electrode performance

If we were not interested in the value of the nominal capacitance, we would have to choose the interdigital shape when the separation

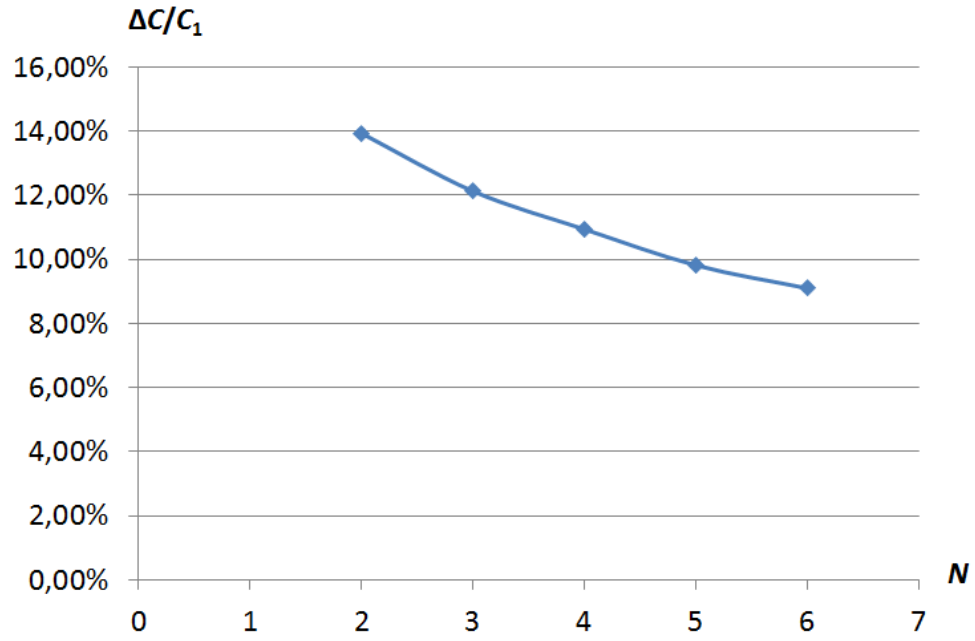

Figure 113: Capacitance change over Nominal Capacitance in function of N

is the biggest, the length of the teeth are the shortest, and the number of teeth is the minimum. Hence, the resulting electrode configuration would be coplanar parallel electrodes with a high separation.

We simulated the effect of the separation on parallel electrodes when measuring the nominal capacitance, the capacitance change and the capacitance change over the nominal capacitance and we obtained Fig. 114, 115 and 116.

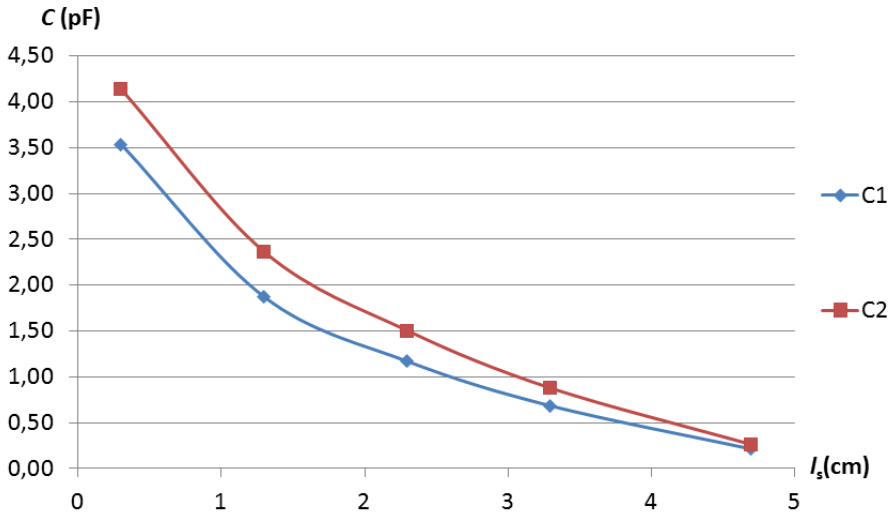

Figure 114: Nominal Capacitance in function of l_{sep}

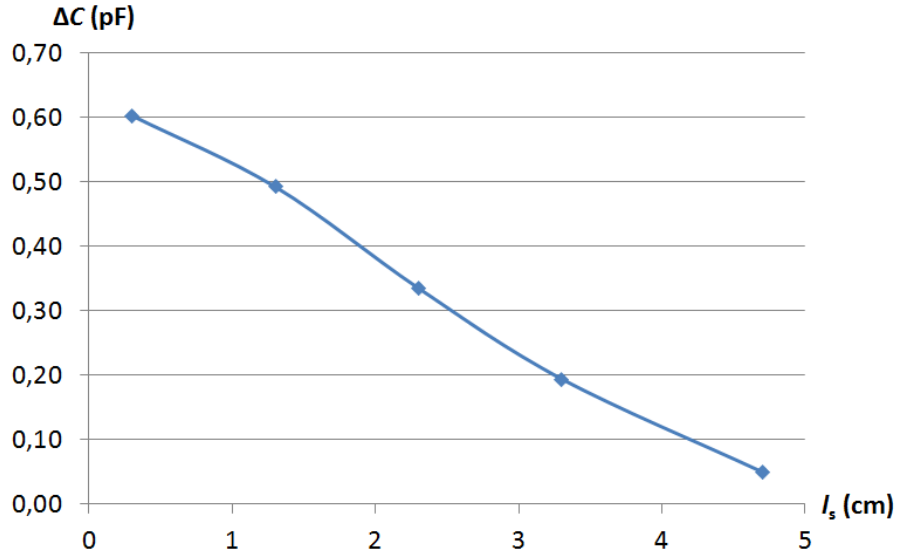

Figure 115: Capacitance change in function of l_{sep}

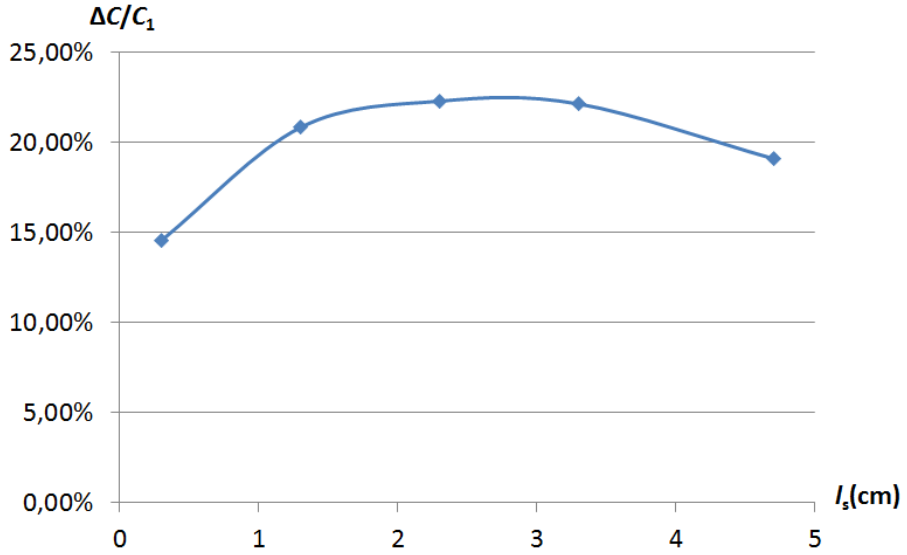

Figure 116: Capacitance change over Nominal Capacitance in function of l_{sep}

As we can see the more separated the less nominal capacitance and capacitance change as was obtained from previous configurations. In the case of capacitance change over nominal capacitance we see that this coefficient improves as the separation is increased until a moment in which it improves no more and starts decreasing. This effect comes from the point in which the electrode size is so small that waves have to look for other ways out of the compost environment to reach ground.

4.5.3 *Experimental results*

To verify the results obtained from the simulations an experiment was set up. Some electrodes were designed and built based on the design changes of the simulations. The electrode output consisted of an SMA connector to be able to connect it directly to a *Agilent* 42941A Impedance probe for the *Hewlett Packard* 4294A Impedance Analyzer, as can be seen in Fig. 117.

Figure 117: Experimental setup

The same exact setup and characteristics as in the single layer case was used. The only difference has been that a polyurethane layer was placed between the compost and the electrodes. That layer was circular, 3 mm thick and had a 4 cm radius. We did not consider the whole protection shown in the simulations since the active guard under the electrodes prevents waves from propagating backwards.

Concentric electrodes

The coplanar concentric electrodes (Fig. 118) were designed to measure the changes when modifying the separation between electrodes and the proportion between the sensing and the ground electrode.

The dimensions of electrodes EC1 and EC2 were $r_a = 1.05$ cm, $r_{g,i} = 1.05$ cm and $r_a = 0.65$ cm, $r_{g,i} = 0.65$ cm, respectively. The separation was 0.9 cm for EC1 and 1.7 cm for EC2. Their performance can be seen in Table 35.

The dimensions of electrodes EC3 and EC4 were $l_{sep} = 0.9$ cm, $r_{g,i} = 1.05$ cm and $l_{sep} = 0.9$ cm, $r_{g,i} = 1.8$ cm, respectively. The

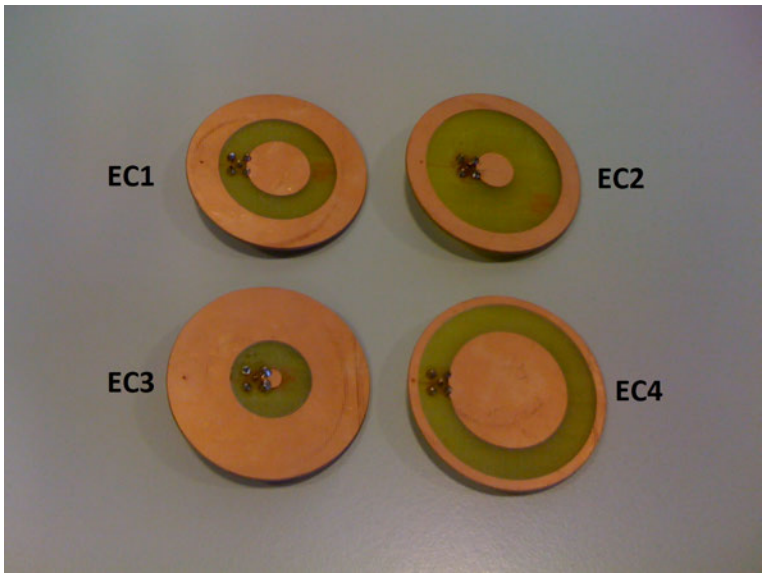

Figure 118: Experimental concentric electrodes

l_{sep}	C_1 (pF)	C_2 (pF)	$\triangle C$ (pF)	$\triangle C/C_1$ (%)
0.9 cm	6.97	8.17	1.20	17.20
1.7 cm	6.49	7.64	1.15	17.60
$l_{sep} \uparrow$	$\downarrow$	$\downarrow$	$\downarrow$	$\uparrow$

Table 35: Concentric electrodes experimental performance in function of l_{sep}

radius of the sensing electrode was 0.3 cm for EC3 and 1.8 cm for EC4. Their performance can be seen in Table 36.

r_a	C_1 (pF)	C_2 (pF)	$\triangle C$ (pF)	$\triangle C/C_1$ (%)
0.3 cm	7.94	1.02	2.29	28.8
1.8 cm	7.98	1.06	2.66	33.3
$r_a \uparrow$	$\uparrow$	$\uparrow$	$\uparrow$	$\uparrow$

Table 36: Concentric electrodes experimental performance in function of r_a

As can be seen the behavior of modifying the separation or the proportion in the sizes between the sensing and the ground electrodes, is the same as seen in the simulations. The nominal capacitance is higher in the experimental case since the density of the compost is much higher, hence the slope of the humidity/permittivity line is higher the higher the density.

Interdigital electrodes

The coplanar interdigital electrodes (Fig. 119) were designed to measure the changes when modifying the separation between electrodes, the length of their teeth and the number of teeth.

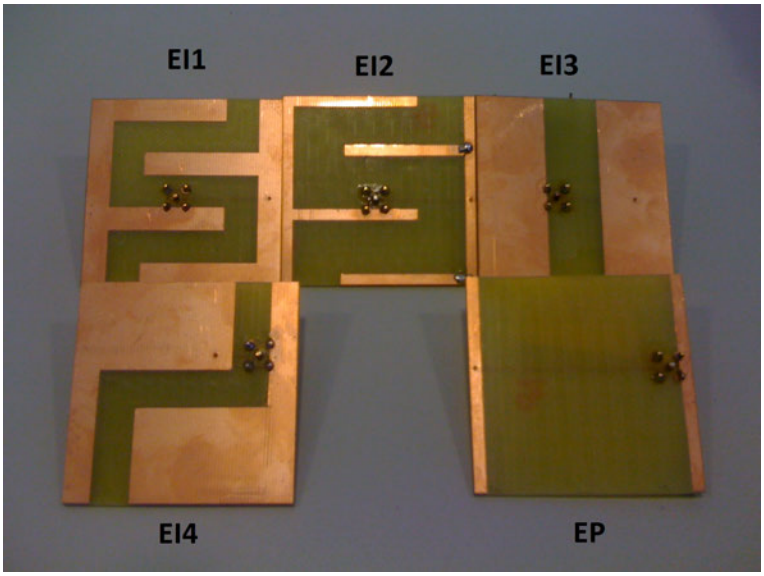

Figure 119: Experimental interdigital electrodes

The dimensions of electrodes EI1 and EI2 were $w_{teeth1} = 0.65$ cm, $w_{teeth2} = 0.65$ cm, $l_{teeth} = 3.1$ cm and $w_{teeth1} = 0.3$ cm, $w_{teeth2} = 0.3$ cm, $l_{teeth} = 3.4$ cm, respectively. The separation was 0.9 cm for EI1 and 1.5 cm for EI2. Their performance can be seen in Table 37.

l_s	C_1 (pF)	C_2 (pF)	$\triangle C$ (pF)	$\triangle C/C_1$ (%)
0.9 cm	6.89	7.48	0.59	8.55
1.5 cm	6.07	6.59	0.52	8.58
$l_s \uparrow$	$\downarrow$	$\downarrow$	$\downarrow$	$\uparrow$

Table 37: Interdigital electrodes experimental performance in function of l_s

The dimensions of electrodes EI3 were $w_{teeth2} = 1.9$ cm, $l_s = 1.5$ cm. The length of the teeth was 0 cm for EI3 and 3.4 cm for EI2. Their performance can be seen in Table 38.

The dimensions of EI4 were $l_{teeth} = 3.1$ cm, $w_{teeth1} = 2.2$ cm, $w_{teeth2} = 0.65$ cm, $l_s = 0.9$ cm. The number of teeth was 2 for EI4 and 4 for EI1. Their performance can be seen in Table 39.

Again the same behavior as in the simulations is confirmed.

l_{teeth}	C_1 (pF)	C_2 (pF)	$\triangle C$ (pF)	$\triangle C/C_1$ (%)
0 cm	6.04	9.47	3.43	56.80
3.5 cm	5.72	6.47	0.75	13.20
$l_{teeth} \uparrow$	$\downarrow$	$\downarrow$	$\downarrow$	$\downarrow$

Table 38: Interdigital electrodes experimental performance in function of l_{teeth}

$\#_{teeth}$	C_1 (pF)	C_2 (pF)	$\triangle C$ (pF)	$\triangle C/C_1$ (%)
2	6.25	7.40	1.15	18.40
4	6.31	7.44	1.13	17.80
$\#_{teeth} \uparrow$	$\uparrow$	$\uparrow$	$\downarrow$	$\downarrow$

Table 39: Interdigital electrodes experimental performance in function of $\#_{teeth}$

Coplanar parallel electrodes with polyurethane layer

The coplanar parallel electrodes chosen were also designed to corroborate the results obtained in the simulations, when varying the separation between electrodes. The dimensions of EP were $w_{teeth2} = 0.3$ cm, $l_s = 4.7$ cm. The separation for EI3 was 0.9 cm and for EP 4.7 cm. Their performance can be seen in 40.

l_s	C_1 (pF)	C_2 (pF)	$\triangle C$ (pF)	$\triangle C/C_1$ (%)
0.9 cm	5.58	6.63	1.05	18.80
4.7 cm	4.99	6.00	1.01	20.20
$l_s \uparrow$	$\downarrow$	$\downarrow$	$\downarrow$	$\uparrow$

Table 40: Parallel electrodes experimental performance in function of l_s

Finally, the last electrode experimental behavior also corresponded the one found in the simulations.

4.5.4 *Conclusions*

We have successfully simulated and tested experimentally the behavior of nominal capacitance, capacitance change and capacitance change over capacitance, when modifying dimensions in interdigital and concentric coplanar electrodes for multilayer dielectrics. The following recommendations for the design of electrodes where extracted:

We could use concentric electrodes to have the biggest nominal capacitance and the sensitivity ($\triangle C$) when the predominant disturbance is the noise of the system and also to avoid corner effects. If we wanted them for the first thing then we need to decrease the separation and to increase the sensing electrode as much as possible. If we wanted them only for the second reason then, to increase the sensitivity when the error depends on the relative permittivity, we need to increase the separation and the sensing electrode, avoiding the limit cases which produce the opposite effect.

We will use parallel electrodes to have the biggest relative sensitivity ($\triangle C/C_1$) since the the predominant disturbance is the inaccuracy due to the heterogeneity of the material. To do so we need to increase the separation as much as possible without reaching the limits. Also we have to be careful since these electrode design is the one with the lowest nominal capacitance.

4.6 FINAL ELECTRODE CALIBRATION

Coplanar parallel electrode have the highest sensitivity when the separation is not too big nor too small. However, as explained before, the higher the sensing sensitivity the higher the sensitivity error. We have determined that the best error-sensitivity relation appears when the separation is as big as possible. And, although experimentally the nominal capacitance has resulted bigger than 1 pF, theoretically this value can be smaller[1]. As such, it has been determined that the suitable electrodes for our application would be the coplanar parallel electrodes with a separation of 0.9 cm.

Now we will calibrate the geometry factor of these electrodes by calibrating them.

If we calculate the relative permittivity of $C_1 = 5.58$ pF with equation (4.6) and then we calculate the calibration factor ($K_c \cdot \Gamma$) with Equation 4.1 we obtain a value of 0.0437.

If we do the same for $C_2 = 6.63$ pF we obtain a calibration factor of 0.0383. As we can see the difference between the two calibrated factors is considerably big (a 12.36 % difference). This is normal due to what we said at the beginning of the chapter, compost is a very heterogeneous material and Equation 4.1 answers to a single dielectric. To this we can add the error in the calculation of humidity with the moisture analyzer. As said in the first chapter, current commercial humidity sensors are accurate within a 5-10% margin,

1 We have to take into account that the compost used in the experimental setup was much more dense than the supposed in the simulations which would be translated as a relative permittivity of around 20.

and as such their measure may have caused the calibration factor to vary between a 5 and 10 %.

In our case, to reduce the uncertainty, we can average the calibration factor to obtain a better reference. Obviously, with more samples the calibration factor uncertainty could be reduced more. A part, we should do a calibration curve dependent on the humidity level.

4.7 ELECTRODE DESIGN CONCLUSION

We have obtained a theoretical model for the calculation of the capacitance for concentric and interdigital electrodes. This model can be used to calculate the relative permitivity of a material in contact with the elctrodes. If a protective layer is put between the electrodes and the material under test then the theoretical model would measure the permittivity of both materials.

The theoretical model can be used to see what kind of concentric or interdigital electrode would be more suitable for a specific application. Nevertheless, some recommendations for the design of electrodes have been extrapolated in function of their application:

If the electrodes will be in direct contact with the dielectric under test

You can use concentric electrodes to have the biggest nominal capacitance and the biggest sensitivity when the noise does not change in function of the relative permittivity, and to avoid corner effects. Whether you are interested on one of their advantages or all of them, you have to take into account that if you want to have the highest sensitivity you need to decrease the separation between electrodes and to make the sensing electrode much bigger than the ground electrode. In the case you want the highest sensitivity when the noise depends on the relative permittivity, you need to increase the separation as much as possible.

You can use interdigital electrodes to have the biggest sensitivity when the noise changes in function of the relative permittivity. In that case you need to increase the separation between electrodes, the length of the teeth and the number of teeth.

If the electrodes have a protective layer

You can use concentric electrodes to have the biggest sensitivity when the noise does not change in function of the relative permittivity, and to avoid corner effects. If you want them for the first thing then you need to decrease the separation and to increase the sensing

electrode as much as possible. If you want them only for the second reason then, to increase the sensitivity when the error depends on the relative permittivity, you need to increase the separation and the sensing electrode, avoiding the limit cases which produce the opposite effect.

You can use parallel electrodes to have the biggest sensitivity when the noise changes in function of the relative permittivity. To do so yo need to increase the separation as much as possible without reaching the limits. Also yo have to be careful since these electrode design is the one with the lowest nominal capacitance.

Others

If you can change the size of the electrodes then choose to make them bigger, not only to increase their nominal capacitance, but also their sensitivity. Also if you want to mix characteristics of electrodes you could design hybrids electrodes, e.g. a concentric interdigital electrode to avoid corner effects and to increase the sensitivity as much as possible when the electrode is not in direct contact with the dielectric under test.

It's more fun to arrive a conclusion than to justify it.

— Malcolm Forbes, pulbisher

5 CONCLUSIONS

Along the development of this thesis compost has been proved to be a very complex material for monitoring, study and characterization. As follows we will detail conclusions for the different objectives of the project and for the overall thesis.

First of all, a temperature system has been developed embedded into a protective material able to measure and record temperature, to operate inside a compost pile (or whichever enclosure we were using) for at least two months recording samples every half an hour. We found that the protective material delayed the thermal conductivity and the measured temperature followed the compost temperature with a first order delay. To compensate this effect an algorithm implementable in microcontrollers was developed to calculate the the tendency of the first order (this method allows the final value to be found in 65 % of the time required using the first-order system generic equation for an error lower than 0.1 %, or 59 % of the time for an error lower than 1 %). To be able to have an autonomous system we applied different techniques for consumption saving; one of them was the direct sensor-to-microcontroller interface which we proved to consume much less than classic conditioning at the cost of some resolution. At the end, our system was able to successfully measure through an experiment on a compost pile for two months (although it could have last longer).

Secondly, the wireless communication in compost was studied to remotely send the measures to the operator without any intervention in the monitoring system.We saw that the attenuation in compost was bigger than in air or soil, and that it increased with the frequency. Still, we found that for lower bands (under 500 MHz) the communications were possible for distances around 10 m. We decided to use the 433 MHz free band for the transmission in compost mainly for its good relation attenuation/consumption and because of the availability of transmitting devices at this frequency band. We developed experiments to see what was the attenuation of 433 MHz antennas, inside of the protective capsule, in function of the

distance. We saw that the protective layer detuned the antenna and displaced the design frequency which we propose that could be compensated through a tuning circuit connected to the antenna. We also saw that the attenuation of compost was inversely proportional to the distance elevated to 3. Some tests based on our study were realized inside a compost pile and proved that a distance of 3 to 4 m allowed a proper transmission of information through compost.

Finally, the optimal method of measure of the humidity of compost from the inside of a protective capsule was studied. We developed a humidity sensor system based on the changes of a pair of coplanar capacitive electrodes placed inside a capsule which allowed a local measure of humidity with a low consumption. Before, though, we characterized the relative permittivity of compost to see how humidity, density, temperature and salt content affected. We found that impedance measures of compost with capacitive electrodes at frequencies from 25 MHz to 100 MHz allowed neglecting the effect of temperature and salt content. At the end we extracted an equation which described the relative permittivity of compost in function of its humidity and density.

Regarding the shape and dimensions of the coplanar capacitive electrodes we simulated different cases for **concentric** and **interdigital** electrodes. The results of the simulations were modeled and an equation for each type was obtained. The simulations and the equations were compared to some lab experiments and their acceptable use for experimental cases was demonstrated. Together with the equations some recommendations were defined to help design an optimum electrode in function of the disturbance sources. In our case, since we have a protective capsule and our main disturbance is the uncertainty of the material under measure we would use parallel coplanar electrodes increasing the separation as much as possible without reaching the limits.

APPENDIX

A

TEMPERATURE SYSTEM COMPONENT SELECTION

As follows we will explain the rest of the components of the architecture, their options and their justifications.

A.1 MICROCONTROLLER

In order to manage and control any kind of system a brain is needed. This brain is not required to be complex, and for autonomous systems as our application they can be as simple as a microcontroller. A microcontroller (also microcontroller unit, MCU or µC) is a small computer on a single integrated circuit consisting of a relatively simple CPU combined with support functions such as a crystal oscillator, timers, watchdog, serial and analogue I/O, etc [128].

There are many microcontroller manufacturers, but the most important ones are *Atmel Corporation*, *Microchip Technology* and *Texas Instruments*. Focusing on the main manufacturers increases the availability of the products, technical support disposal and the possibility of obtaining samples.

Our microcontroller should have a flash memory over 8 kbits in order to be able to implement an algorithm for controlling and managing the whole system. This number was found from the experience on the design of a previous temperature system, in which an 8 kbit capacity was needed to implement its algorithm[129].

To be able to download and upload data between the microcontroller and a computer, a serial UART is needed. A part, in order to communicate with the real time clock and the EEPROM devices an i2C bus interface is required. I2C uses the typical master-slave architecture of the microcontroller systems. Unlike the CAN bus interfaces, the i2C consumption is lower and its transmission speed is bigger.

As will be explained in the sensor conditioning section, in order to use the direct sensor-to-microcontroller interface, as the signal conditioning method, an external interruption port with an Schmitt trigger integrated is needed. Nowadays, all new microcontrollers do have this feature, but when searching it is important to make it sure.

When looking for the specifications we need within the *Atmel* products we found many MCU fulfilling them. The lowest prize was

5.55 € (1 unit. *Farnell*) and *Atmel* MCUs are well known for their powerful and efficient C compilers.

As for the *Microchip* MCUs, according to its parametric search, there was just one microcontroller that had the desired specifications: the PIC18F6393. Its prize was 4.64 € (1 unit. *Farnell*) and did not specify about external interruption ports with integrated Schmitt Trigger. *Microchip* also has good C compilers but worse than *Atmel*.

As *Atmel*, *Texas Instruments* (*TI*) has many MCUs fulfilling our specifications and the lowest prize is 4.32 € (1 unit. *Farnell*). *TI* has the worst C compilers from the three main manufacturers, but its MCUs have great control over the sleep mode. They have different sleep modes and it is possible to wholly control what is active each time. Besides they have different clock options, meaning that the internal clock can be used for non accurate functions and external clocks (which can be greatly divisible) for accurate functions.

Since *TI* has the lowest prize and it can minimize the system consumption with the features previously described we will choose to work with this MCU family. As follows, in Table 41 we can see the *TI* MCUs that fulfill our specifications:

Part Number	Max Speed (MHz)	Standby Current (ÂµA)	Active Current (mA/MHz)	Op Amps	Price (US$) 1ku
MSP430F155	8	1.1	0.33	0	4.95
MSP430F2252	16	0.5	0.27	0	2.20
MSP430F2254	16	0.5	0.27	2	2.40
MSP430F2350	16	0.7	0.27	0	2.20
MSP430F4152	8	0.9	0.22	0	1.90

Table 41: *Texas Instruments* MCUs comparative

As we can see the first device, the MSP430F155, is really expensive compared to the other ones and, besides, its consumption is much higher, therefore it is discarded.

The last one, the MSP430F4152, has the lowest price, but it has a lower speed than the rest and its standby current is higher. It is true that it has a lower active current, but since we will try to leave the system sleeping the maximum possible time we are more interested on a lower standby current.

The three left have a similar prize, but the MSP430F2350 has a higher standby consumption. The other two have exactly the same characteristics except for the prize, the MSP430F2252 is slightly

cheaper, and that the MSP430F2254 has two internal operational amplifiers. The prize is too similar and it is possible that the internal operational amplifiers may become useful; therefore we decided to initially use the **MSP430F2254**.

A.2 SENSOR

Resistance Temperature Detector (RTD), thermocouple, thermistor, and Integrated Circuit (IC) sensors are all useful temperature measurement options, with thermistors and IC sensors relegated to narrower temperature ranges than RTDs and thermocouples.

RTDs provide higher accuracy because platinum is more stable than most of the materials used in thermistors, thermocouples, and IC sensors. RTDs, thermistors, and IC sensors use standard instrumentation wire to connect to the measurement or control equipment. Thermocouples, on the other hand, require special thermocouple extension wire.

Thermocouples are generally less expensive than RTDs, but are competitive with thermistors and IC sensors in some applications. They are more durable in high-vibration or mechanical shock applications, and are usable for measuring high temperatures. Because the different types of thermocouples are standardized, they can be easily replaced when necessary.

Thermistors provide higher resolution than RTDs or thermocouples, and generally cost less. Their lower temperature range and nonlinearity limit their ability to work over large temperature excursions. Their low mass and small size give them quick response to temperature changes. The lack of standard resistance vs. temperature curves can cause difficulty in replacing sensors when needed.

IC and RTDs are linear sensors with a low prize, and an easy conditioning. For our application we need to have a good accuracy level and IC temperature sensors do not fulfill this. Thermocouples have an even better accuracy than RTDs, but their special wire requirements make them unsuitable for our setup. In Table 42 it is possible to see some mayor commercial examples for each type of temperature sensor. The RTD temperature chosen for our application is the Pt1000 which, besides, will allow using some new conditioning methods.

A.3 REAL-TIME-CLOCK (RTC)

To keep the track of the current time when the measurements or different operations are realized, a Real-time-clock (RTC) is needed.

Sensor	Pt1000	PRC 100	LM35	BTC-1
Type	RTD	Thermistor	IC	Thermocouple
Manufacturer	*Labfacility*	*Tektronix*	*National*	*TC-OMEGA*
Supply Voltage (V)	-	5 to 12	4 to 20	-
Temperature range (°C)	-50 to 500	-40 to 150	-55 to 150	-100 to 400
Accuracy (°C)	±0.1	±0.1	±0.5	±0.05
Prize (€)	7.53	10.31	0.81	7.65

Table 42: Commercial Temperature sensors

The main RTC manufacturers are *Epson Toyocom Corporation*, *Intersil Corporation*, *Maxim Integrated Products*, *Micro Crystal AG*, *NXP Semiconductors* and *STMicroelectronics N.V.*.

For our system we need an RTC controlled through an i2C bus interface and it should be able to work at temperatures over 70 °C. Also, it should have a minimum voltage supply of 3 V in order to agree with our selected microcontroller requirements and its prize and current consumption must be the lowest.

From all the listed manufacturers the more economical ones were *STMicroelectronics*, *NXP*, *Intersil* and *Maxim*, as can be seen in Table 43.

Epson	*Intersil*	*Maxim*	*Micro Crystal*	*NXP*	*STM*
4 €	2.07 €	2.27 €	10.52 €	1.84 €	1.38 €

Table 43: Minimal prize within the RTC fulfilling the specified requirements (data according to *Farnell*)

If we compare the devices with the better relation current consumption-prize of each of these manufacturers, we obtain Table 44.

As can be seen, the cheapest device is the PCF8563T of *NXP Semiconductors*; moreover it is the one with the lowest standby current supply. The system will be designed in order to be sleeping the maximum possible time, therefore the current supply that will rule will be the standby current. Thus the selected RTC was the **PCF8563T**.

Manufacturer	*Intersil*	*Maxim*	*NXP*	*STM*
Name	ISL1220IUZ	DS1371U	PCF8563T	M41T00S
Voltage range (V)	[2.7, 5.5]	[1.7, 5.5]	[1.8, 5.5]	[2.7, 5.5]
Active current supply (µA)	120	150	800	300
Standby current supply (µA)	5	70	1.7	70
Op. temperature range (°C)	[-40, 85]	[-40, 85]	[-40, 85]	[-40, 85]
Prize (€) (*Farnell*)	2.07	2.27	1.84	1.98

Table 44: Comparative of the different manufacturer RTC devices

A.4 ELECTRICALLY ERASABLE PROGRAMMABLE READ-ONLY MEMORY (EEPROM)

In order to have a record of the measurements, as a backup or as a monitoring report, an Electrically Erasable Programmable Read-Only Memory (EEPROM) is needed.

The main EEPROM manufacturers are *Atmel Corporation*, *ON Semiconductor*, *Microchip Technology* and *STMicroelectronics N.V.*.

As for the RTC, we need an EEPROM controlled through an i2C bus interface, able to work over 70 °C, with a minimum voltage supply of 3 V and its prize and current consumption must be the lowest.

As for the capacity we can take the following example of storage. Let us suppose that we take temperature samples once each hour (the minimum stated in Chapter 2) during two months (composting process duration). The information stored each time is the following: N_x, N_{c1}, N_{c2}, day, month, year, hours, minutes and seconds. N_x, N_{c1} and N_{c2} are the times of discharge of the resistances R_x (Pt1000), R_{c1} and R_{c2} (short-circuit) in the direct sensor-to-microcontroller interface (Sensor conditioning section); and each of them is a variable of 16 bits. As for the day, month, year, hours, minutes and seconds, those are 8 bits variables. Therefore each hour we store 96 bits. If we make the calculation the total information stored is:

$$96\,\frac{\text{bits}}{\text{hour}} \cdot 2\,\text{month} \cdot 30\,\frac{\text{days}}{\text{month}} \cdot 24\,\frac{\text{hours}}{\text{day}} = 138240\,\text{bits} = 135\,\text{kbits}$$

We can estimate that an EEPROM of 250 kbits or higher would be suitable for our needs.

From each of the manufacturers listed we chose the device with the best relation prize-current consumption and developed Table 45.

Manufacturer	*Atmel*	*ON*	*Microchip*	*STM*
Name	AT24C25BN	CAT24C256	24AA256	M24256
Capacity (kbits)	256	256	256	256
Voltage range (V)	[1.8, 5.5]	[1.8, 5.5]	[1.7, 5.5]	[1.7, 5.5]
Op. current (Read) (mA)	2	1	0.4	2
Op. current (Write) (mA)	3	3	3	5
Standby current supply (µA)	6	1	1	5
Op. temperature range (°C)	[-55, 125]	[-65, 150]	[-40, 85]	[-40, 85]
Prize (€) (*Farnell*)	2.21	1.86	1.72	1.37

Table 45: Comparative of the different manufacturer EEPROM devices

As we can see the device with the lowest current consumption is the 24AA256 of *Microchip Technology*. It has not the lowest prize, but the difference is extremely low. Thus the selected EEPROM was the **24AA256**.

A.5 VOLTAGE REGULATOR

The voltage regulator used was the MAX882 of *Maxim* which gives a regulated output in order to eliminate the noise in the supplying line. Also it has a shutdown feature which would allow switching off the whole circuitry, reducing the supplied current to less than 1 µA. It has a large input range (from 2.7 V to 11.5 V) and a fixed output voltage (of 3.3 or 5 V). Its temperature range goes from -40 ºC to 85 ºC and its quiescent current is of 15 µA. Finally, the best feature is the low dropout, which allows avoiding problems with the lowest usable voltage.

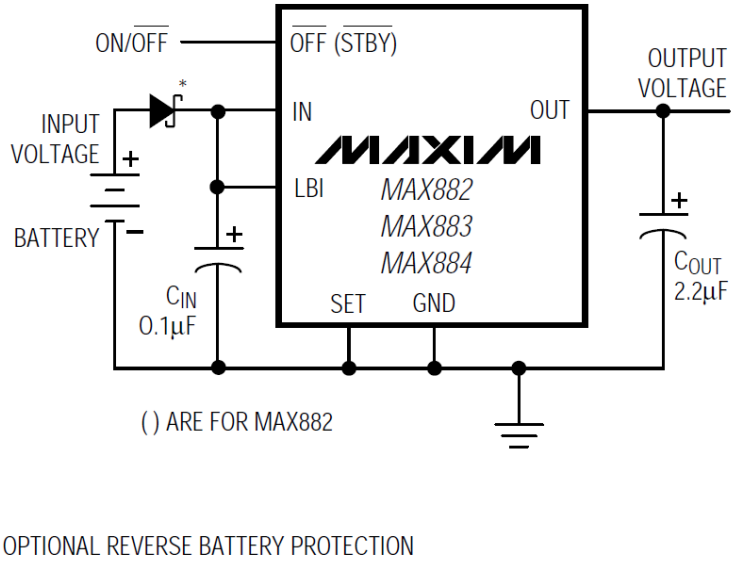

Figure 120: Voltage regulator circuit provided by the manufacturer (Taken from 5V/3.3V or Adjustable, Low-Dropout Low Iq, 200mA Linear Regulators Datasheet)

In order to supply a regulated voltage of 3.3 V we designed the voltage regulator circuit with the circuit provided by the manufacturer (Fig. 120).

A.6 BATTERIES

The batteries used were the 1/2 AA lithium thionyle, reed-less, non-rechargeable batteries provided by *RS Amidata*. These batteries stand temperatures until 85 °C, deliver 3.5 V and have a nominal capacity of 950 mAh.

The consumption of each component of the temperature system during each interval of the monitoring (1 h) can be seen in Table 46.

As can be seen, most of the devices are active during a very short time and sleeping most of the time. The ON-OFF method allows the consumption of the system to reduce a lot and even more when using more than one sleep state in the MCU.

The average consumption ($I_{s,m}$) is therefore

$$I_{s,m} = \sum_{0}^{N} \frac{I_{s,i} \cdot t_i}{t_T} \tag{A.1}$$

Device	Mode	Current (A)	Time (s)
Microcontroller	Active	5.50E-04	1.25E-03
	Low Power Mode 0	3.00E-06	3599.918755
	Low Power Mode 3	3.80E-06	0.08
EEPROM	Write	3.00E-03	2.25E-06
	Sleep	1.00E-06	3599.999998
RTC	Active	8.00E-04	2.13E-06
	Sleep	6.50E-07	3599.999998
Voltage Regulator	Always	1.50E-05	3600

Table 46: Temperature system consumption

where $I_{s,i}$ is the supplied current of component 'i', t_i is the time this 'i' component is working and t_T is total amount of time the system works.

If we calculate $I_{s,i}$ we get an average consumption of 1.97E-02 mA, which for the decomposition stage (2 months) would need a battery of 28.3 mAh. Therefore these batteries would stand more than 33 uses.

B

NEED OF PROTECTION

There are several elements within the composting process that are harmful for an electronic circuit unless protected. The pressure and machinery found during the composting process are physically harmful; the gasses and liquids generated during the composting process are chemically harmful; and the temperature and the moisture content are characteristics of the harmful environment of the composting process. Therefore, a proper protection, taking into account that its worsening cannot contaminate the composting material, is needed gathering the following characteristics.

B.1 PHYSICAL PROTECTION

Temperature during the composting process is critical, and if too high, the decomposing agents die. To decrease temperature a compost turner (Fig. 121), together with some watering, is typically used.

Figure 121: Compost turner [130]

The shovels of the compost turner turn around at a high speed oxygenating and homogenizing the organic matter mixture, not crushing it though. This movement can hit the protected circuit and hurl it away; because of this, material resistance is important. The frequency of use of the compost turner depends on the material, the

season of the year, the kind of facilities, the geographical zone, etc. During the decomposition stage (lasts between 15 days and a month) the turning frequency can vary from once per week to 6 times per week. On the other hand, during the curing stage (lasts between 1 to 4 months) the turning frequency is gradually reduced, since there is less degradable material.

In order for the circuit to be able to stand the action of the compost turner, a protection against blows is needed. And on the other hand, a protection is needed to stand the weight of the material and the pressure of the concentration of material.

B.2 CHEMICAL PROTECTION

Conditions inside composting can be aggressive due to pH and some gas release, mainly when processes are not properly controlled. Depending on the material, physical structures can be decomposed due to these conditions. On the other hand, some of these gases can affect circuits inside the protection. Ammoniac (NH_3) is the main gas controlled at composting plants. It indicates that nitrogen gas is being lost, instead of remaining on an organic way linked to carbon structures. The main problem of this gas at closed installations is that high concentrations may result toxic.

Another gas produced is CO_2, which answers to the breathing related to the aerobic bacterial activity. Moreover, there are more gasses that are produced in composting plants. When the process is not properly controlled; microbes can derive to anaerobic processes, where methane (CH_4) is the main result of the anaerobic breathing. Other toxic compounds such as hydrogen sulphide (SH_2) can emerge too.

Circuits may be affected by these gases, generated during the composting process, unless a good protection is used.

B.3 THERMAL AND HUMIDITY PROTECTION

Variation of temperature during biological transformation of organic material is a consequence of microbial activity. During composting, this degradation is developed aerobically and organic matter is transformed into carbon dioxide and water and energy loss due to chemical reactions. When complex organic molecules are broken in simpler ones, energy is released from their bonds. Generally, it is known that energetic value of carbohydrates and proteins is about 4 kcal/g, while lipids are about 9 kcal/g, but a wide range of values is considered (Table 47). In case of municipal solid waste, composition

is highly varied and heat generation is between 2.1 and 9.3 kcal/g, which can evaporate between 3 and 15 g of water [131].

Molecule	Molecular weight	kcal/g
Glucose	180	3.74
Ac. lactic	90	3.62
Ac. palmitic	256	9.37
Tripalmitine	809	9.28
Glycine	75	2.18
Methane	16	11.34
n-decane	142	13.18

Table 47: Heat generation of different molecules [132]

During composting temperature (Fig. 122) can reach really high values due to the microbial activity, but beyond certain temperature biological population can strongly decrease. A temperature increment in the thermophilic range (around 45 °C and 65 °C) can eliminate pathogens and avoid recolonization [133]. The ideal temperature range during this stage is 50 °C to 60 °C in order to maximize decomposition and cleaning of the material; when temperature goes beyond 70 °C abiotic conditions can appear.

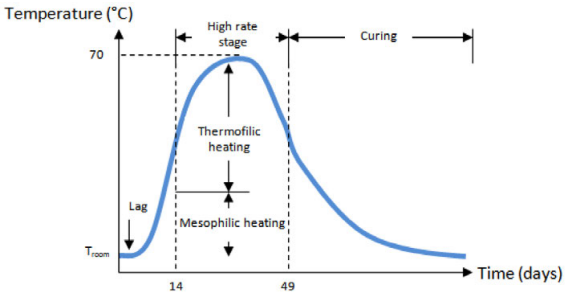

Figure 122: Composting temperature evolution [132]

Decomposition of organic matter needs a certain moisture level to guarantee microbial activity; later on, it will decrease as the process goes on (Fig. 123) due to the decrease of this microbial activity in relation to the reduction of degradable organic matter. The acceptable moisture content range goes from 50 % to 60 % [132]. Moisture going to too high values can cause anaerobic conditions

and excess of leachates and, consequently, the appearance of bad odors.

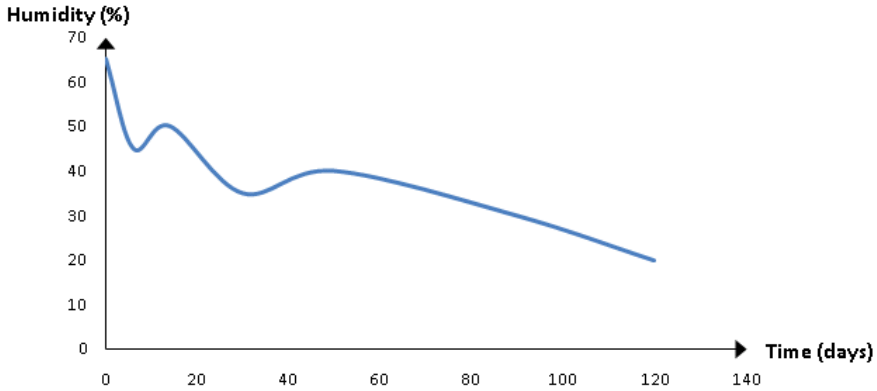

Figure 123: Composting humidity evolution

After the active composting stage the curing phase follows. In this stage the microbial activity slows down and as the process nears completion, the material approaches environment air temperature. Finished compost takes on many of the characteristics of humus, the organic fraction of soil. The material will have its volume reduced by 20 % to 60 %, its moisture content by 40 % and its weight by up to 50 % from the initial material. It can be considered that, in an adequate process, from every 100 kg of raw material at the start of the process, around 25-35 kg of compost should be obtained.

The circuitry may operate at high temperatures during the composting process, but a minimal IP 67 protection is needed to protect against the humidity level.

C

THERMAL CONDUCTIVITY

As said in the first chapter the material of the composting process is heterogeneous, and as such, the temperature incredibly varies depending on the location. Therefore, when measuring temperature from within a protective material in compost we may wonder what the effect of these heterogeneous thermal focus is over the measure.

If we look into the thermal conductivity basic concepts, we see that when two bodies with different temperatures are put into contact the one with the higher one transmits heat to the other reducing its temperature whilst the other increases its own, until they both reach a thermal equilibrium. That would be our case when introducing the circuit into a thermally homogeneous material. But we will surely have two or more thermal focus around our system when measuring inside compost. In that case we have that when putting the circuit inside the compost, it will receive the heat from all the focus and will increase its temperature until the lowest temperature of the different focus (Fig. 124). Once the circuit has reach this temperature it will behave as a thermal conductor between focus and the heat will transmit through it from the higher temperature focus to the lower ones. Thus, the circuit will end up having a distribution of temperatures within it and not a fixed one.

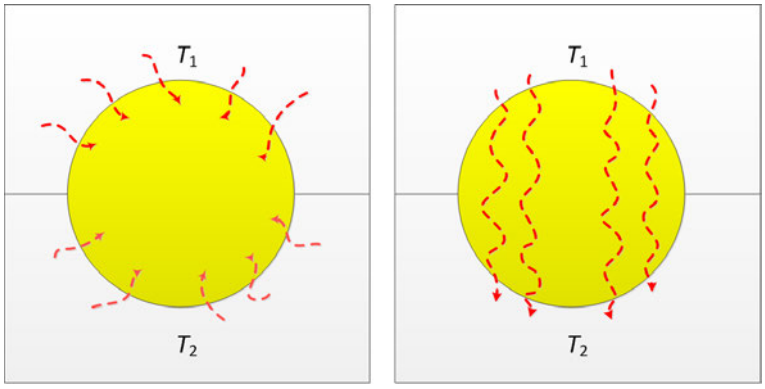

Figure 124: (left) Circuit acquiring the temperature of the focus around it. (right) circuit playing as a thermal conductor between focus.

The effect when measuring is that the measure of temperature will depend on the location of the temperature sensor inside the protection. The measure of temperature will be close to the value of the closest focus, but it will not be exact since it will be affected

by the heat transmission to or from the other focus. The sensor is placed as near from the exterior as possible in order for it to be close to the temperature value of the nearest focus.

The fact that the circuit cannot control all the focus around it stresses the need of multiple temperature sensor systems measuring at the same time inside the composting material.

BIBLIOGRAPHY

[1] Fernandez, J. "El compost, temperatura y humedad" [on-line]. *Compostodares*: [Consulted on: June the 5th of 2009]. Available at: http://www.compostadores.com/v3/castellano/articulos/detalles.asp?ArticulosID (Cited on page 2.)

[2] "Engineers and Consultants in Resource Managment. Compost Temperature" [on-line]. *Resource Recycling Systems, Inc.*: [Consulted on: June the 4th of 2009]. Available at: http://www.recycle.com/pdfs/temperature.pdf (Cited on pages xi, 2, and 3.)

[3] "El compostaje (1ª parte)" [on-line]. *infoAgro*: [Consulted on: June the 5th of 2009]. Available at: http://www.infoagro.com/abonos/compostaje.htm (Cited on pages xi, xii, 2, 3, and 68.)

[4] Stoffella, P. J. "Utilización de compost en los sistemas de cultivo hortícola". *Mundi-Prensa Libros*, 2005. ISBN 848476186X, 9788484761860. (Cited on page 2.)

[5] "Guia d'ambientalització docent de l'EUPM" [on-line]. *Escola Universitària Politècnica de Manresa* (Manresa, Spain): [Consulted on: June the 10th of 2009]. Available at: http://bibliotecnica.upc.es/e2Dambit/info/documents/GAD/Eupm (Cited on pages 3 and 67.)

[6] "Food and Rural Development Compost Temperature Measurement: Livestock Manure" [on-line]. *Alberta Government* (Alberta, Cannada): Agdex 400/27, 2005, updated on May the 1st of 2005 [Consulted on: June the 10th of 2009] Avaliable at: http://www1.agric.gov.ab.ca/$department/deptdocs.nsf/all/agdex9928 (Cited on pages 3, 4, 6, and 128.)

[7] Mason, I. G. "Mathematical modelling of the composting process: A review". *Waste Management*, Vol. 26, pp. 3-21, 2006 (Cited on pages 4 and 128.)

[8] "Thermometers, Clocks & Hygrometers" [on-line]. *Gempler's*: [Consulted on: June the 5th of 2009] Available at: http://www.gemplers.com/thermometers-clocks (Cited on page 4.)

[9] Department of Crop and Soil Sciences. "Monitoring the Composting Process" [on-line]. *Cornell University* (Ithaca, New York): [Consulted on: June the 2nd of 2009]. Available at: http://www.css.cornell.edu/compost/monitor/monitoring.html (Cited on pages 4 and 127.)

[10] Barth, J. "Biological waste treatment in europe - technical and market developments". EU Biowaste Treatment. *INFORMA Compost Consultants*. (Cited on pages 4 and 127.)

[11] "Compost Monitoring". *National Defense Center for Energy and Environment*. DoD Executive Agent. Office of the Assistant, Secretary of the Army (Installations and Environment). (Cited on pages 4, 127, and 128.)

[12] DEFRA GUIDANCE Document. September 2008. [Consulted on: August the 10th of 2010] Available at: http://www.defra.gov.uk/animalh/byprods/pdf/guidance0908.pdf (Cited on pages 4, 127, and 128.)

[13] Brinton, W. F. "Compost quality standards & guidelines". *Woods End Research Laboratory* (USA). (Cited on pages 5, 71, 127, and 128.)

[14] Viera, W.; Bernal, G. "Determinación de la calidad microbiológica del compost para la producción ecológica de cultivos en la región interandina". *Seminario Nacional de Investigacion en Agricultura Organica*. 29-30 de septiembre del 2003. (Cited on page 5.)

[15] Michigan State University, Department of Chemistry. "Polymers" [on-line]. *Michigan State University* (Michigan, USA): [Consulted on: June the 5th of 2009]. Available at. http://www.cem.msu.edu/~reusch/VirtualText/polymers.htm (Cited on page 5.)

[16] Textos Científicos. "Policloruro de vinilo - PVC" [on-line]. *Textos científicos*: [Consulted on: June the 5th of 2009]. Available at: http://www.textoscientificos.com/polimeros/pvc (Cited on page 5.)

[17] Lenau, T. "PET (polyethylene terephthalate)" [on-line]. *Design inSite* (Denmark): [Consulted on: June the 5th of 2009]. Available at: http://www.designinsite.dk/htmsider/m0011.htm (Cited on page 5.)

[18] Polymer Processing. "Polystyrene" [on-line]. *PolymerProcessing.com* (USA): [Consulted on: June the 5th of 2009]. Available at: http://www.polymerprocessing.com/polymers/PS.html (Cited on page 5.)

[19] wiseGEEK. "What is Polypropylene?" [on-line]. *wiseGEEK* (USA): [Consulted on: June the 5th of 2009]. Available at: http://www.wisegeek.com/what-is-polypropylene.htm (Cited on page 5.)

[20] San Diego Plastics. "Polyurethane" [on-line]. *San Diego Plastics Inc.* (San Diego, USA): [Consulted on: June the 5th of 2009]. Available at: http://www.sdplastics.com/polyuret.html (Cited on page 5.)

[21] AZOM. "Silicone Rubber" [on-line]. *AZOM*^{TM} (Warriewood, Australia): [Consulted on: June the 5th of 2009]. Available at: http://www.azom.com/details.asp?ArticleID=920 (Cited on pages 6 and 24.)

[22] Waters, D. A.; Abulula, H. H. "Using bat-modelled sonar as a navigational tool in virtual environments". *Int. J. Hum.-Comput. Stud.* 65, 10 (Oct. 2007), 873-886. (Cited on page 6.)

[23] Yang, C.; Bagchi, S.; Chappell, W. J., "Location tracking with directional antennas in wireless sensor networks", *Microwave Symposium Digest, 2005 IEEE MTT-S International* , vol., no., pp. 4 pp.-, 12-17 June 2005 (Cited on page 6.)

[24] Metrocompost S.A. "Tecnología desarrollada para el proceso de compostaje". *Metrocompost*: [Consulted on: June the 8th of 2009]. Available at: http://www.metrocompost.com/es/computunel.htm (Cited on page 6.)

[25] Ontario Ministry of environment. "Interim guidelines for the production and use of aerobic compost in ontario" *Ministry of environment* (Ontario, Canada): [Consulted on: 8th of June of 2009]. Available at: http://www.ene.gov.on.ca/envision/gp/1749e01.htm (Cited on page 6.)

[26] Blackwood, K. R. "Temperature monitoring apparatus and method in a composting system through which organic matter is moved to effect composting". Patent US 5049486. 1991. (Cited on page 9.)

[27] Hammer, J. "Process for compost of biomass and industrial sludge, including products produced by said process". Patent: WO 051772. 2002 (Cited on page 9.)

[28] Reotemp Instruments. "Composting products" [on-line]. *REOTEMP Instrument Corporation* (San Diego, USA): [Consulted on: June the 2nd of 2009]. Available at: http://www.reotemp.com/composting_products.html (Cited on page 9.)

[29] Yeong, K. M.; Ha, Y. J. "Apparatus for automatic and continuous measurement of temperature, moisture content and oxygen concentration in aerobic composting tank, and for control of air-blower and mixer". KR20030073954. 2003. (Cited on page 9.)

[30] Gemini Datalogger. "Wireless measure systems" [on-line]. *Gemini Datalogger Corporation* (West Sussex, UK): [Consulted on: June the 2nd of 2009]. Available at: www.geminidataloggers.com (Cited on page 9.)

[31] Morris, T. "Mechanical aerobic composter". Patent: US4042219. 1977. (Cited on page 9.)

[32] Oolun, M.K.; Jahmeerbacus, M.I.; Soyjaudah, K.M.S.; Bhurtun, C. "A micro-controller based intelligent

controller for a composting plant", *Africon Conference in Africa, 2002. IEEE AFRICON.* 6th , vol.1, no., pp. 101-104 vol.1, 2-4 Oct. 2002. (Cited on page 9.)

[33] Casas, O.; Rillo, F. I. "Method for reducing response time in sensor measurement," *Review of Scientific Instruments*, 80, 085102 (2009). (Cited on pages 9, 10, and 43.)

[34] Sifuentes, E. "Sensor autónomo para detectar vehículos estáticos". PhD Thesis report. Universitat Politècnica de Catalunya (UPC). Departament d'enginyeria electrònica. Barcelona, 2010. (Cited on page 10.)

[35] Reverter, F.; Pallàs-Areny, R. "Direct Sensor-to-Microcontroller Interface Circuits: Design and Characterisation". 1st ed. Barcelona: *Marcombo*, 2005. ISBN 84-267- 1380-7. (Cited on page 10.)

[36] Sinha, A.; Chandrakasan, A. "Dynamic Power Management in Wireless Sensor Networks". *IEEE Design and Test of Computers*, Vol. 18, pp.62-74, 2001. (Cited on page 10.)

[37] T. M. Wendt and L. M. Reindl, "Wake-Up Methods to Extend Battery Life Time of Wireless Sensor Nodes", IEEE Instrumentation and Measurement Technology Conference Proceedings, May 2008, pp. 1407 - 1412. (Cited on page 12.)

[38] D. Macii, A. Ageev, A. Somov, "Power consumption reduction in Wireless Sensor Networks through optimal synchronization", IEEE Instrumentation and Measurement Technology Conference, May 2009, pp. 1346 - 1351. (Cited on page 12.)

[39] S. Jayapal, R. Huang, S. Ramachandran, R. Bhutada and Y. Manoli, "Optimization of Electronic Power Consumption in Wireless Sensor Nodes", Proceedings of the 8th Euromicro Conference on Digital System Design, September 2005, pp. 165 - 169. (Cited on page 12.)

[40] Burr-Brown Products from Texas Instruments, *MSC1210: Precision Analog-to-Digital Converter (ADC) with 8051 Microcontroller and Flash Memory*,

SBAS203J datasheet, January 2008. (Cited on page 13.)

[41] Analog Devices, *AD7745/AD7746: 24-Bit Capacitance-to-Digital Converter with Temperature Sensor*, 2005. (Cited on page 13.)

[42] F. Reverter and O. Casas, "Interfacing Differential Capacitive Sensors to Microcontrollers: A Direct Approach", IEEE Transactions on Instrumentation and Measurement, October 2010, pp. 2763 - 2769. (Cited on page 13.)

[43] F. Reverter and O. Casas, "Interfacing Differential Resistive Sensors to. Microcontrollers: A Direct Approach", IEEE Transactions on Instrumentation and Measurement, October 2009, pp. 3405 - 3410. (Cited on pages 13, 22, and 24.)

[44] E. Sifuentes, O. Casas, F. Reverter, R. Pallàs, "Direct interface circuit to linearise resistive sensor bridges", Sensors and Actuators A: Physical, vol. 147, pp. 210-215, 2008. (Cited on page 13.)

[45] O. Skerl, M. Lippert, S. Paule and G. Czygan, "Impedance sensor for assessing cardiac hemodynamics", IEEE Sensors, October 2008, pp. 1096 - 1099. (Cited on page 13.)

[46] J. Min, S. Park, C. Yun and B. Song, "Development of multi-functional wireless impedance sensor nodes for structural health monitoring", Sensors and Smart Structures Technologies for Civil, Mechanical, and Aerospace Systems, 7647, 764728 (2010) (Cited on page 13.)

[47] J. Kourunena, R. Käyhköb, J. Matulab, J. Käyhköc, M. Vauhkonena and L. M. Heikkinena, "Imaging of mixing of two miscible liquids using electrical impedance tomography and linear impedance sensor", Flow Measurement and Instrumentation, December 2008, vol. 19, issue 6, pp 391-396. (Cited on page 13.)

[48] A. M. Bruneau, "An acoustic impedance sensor with two reciprocal transducers", J. ACOUST. SOC. AM.

Appril 1987, vol. 81, issue 4, pp. 1168-1178. (Cited on page 13.)

[49] H. Ban and Z. Li, "A novel capacitance sensor for fireside corrosion measurement", Rev. Sci. Instrum. 80, 115107 (2009). (Cited on page 13.)

[50] L. Yang, Y. Li, C. L. Griffis, and M. G. Johnson, "Interdigitated Microelectrode (IME) Impedance Sensor for the Detection of Viable Salmonella Typhimurium", Biosensors and Bioelectronics, May 2004, vol. 19, issue 10, pp. 1139-1147. (Cited on page 13.)

[51] National Instruments, Application Note 048, November 1997. (Cited on page 14.)

[52] A. Mezghani and J. A. Nossek, "How to choose the ADC resolution for short range low power communication?", IEEE Proceedings of International Symposium on Circuits and Systems. May 2010, pp. 1025. (Cited on pages 14 and 18.)

[53] O. Nys and R. K. Henderson,"A 19-bit low-power multibit sigma-delta ADC based on data weighted averaging", IEEE Journal of solid-state circuits, July 1997, vol. 32, no. 7, pp. 993-942. (Cited on page 14.)

[54] E. Bilhan and F. Maloberti, ""A Wide-Band 2-Path Cross-Coupled Sigma Delta ADC", IEEE Int. Symposium on Circuits and Systems, May 2008, pp. 1220-1223. (Cited on page 14.)

[55] R. Casanella and R. Pallàs-Areny, "On the design of low-power signal conditioners for resistive sensors", XIX IMEKO World Congress of Fundamental and Applied Metrology, September 2009, pp. 787-791 (Cited on page 15.)

[56] Pallàs-Areny, R; Webster, J. G. "Sensor and signal conditioning". *Wiley Inter-Science*. 2_{nd} ed. United States of America, 2001. (Cited on pages 15, 18, and 45.)

[57] R. Mancini, *Op Amp for Everyone*, Texas Instruments, August 2002. (Cited on page 18.)

[58] B.C. Baker, *Predict the Repeatability of Your ADC to the BIT*, I. Microchip Technology, 2004. (Cited on page 20.)

[59] F. Reverter and R. Pallàs-Areny, *Direct Sensor-to-Microcontroller Interface Circuits: Design and Characterisation*. 1st ed. Marcombo, 2005. (Cited on page 23.)

[60] F. Reverter, "Power Consumption in Direct Interface Circuits" IEEE Transactions on Instrumentation and Measurement, February 2013, vol. 62, no. 2, pp. 503-509. (Cited on page 23.)

[61] M. Vargas and R. Pallàs-Areny, "The seemingly paradoxical noise behavior of some active circuits" IEEE Transactions on Instrumentation and Measurement, October 1994, vol. 43, no. 5, pp. 764-767. (Cited on page 26.)

[62] Zemansky, M. W.; Dittman, R. H. "Calor y termodinámica", *Mc Graw Hill.* 6th ed. Madrid, 1990. (Cited on page 39.)

[63] MatWeb, MatWeb: Material Property Data [online]. [Consulted on: January 2012]. Available at: http://www.matweb.com/index.aspx (Cited on pages xvi, 40, 41, 42, 43, 108, and 129.)

[64] Kreith, F.; Manglik, R.; Bohn, M. "Principles of Heat Transfer, SI Edition". *Cengage Learning.* 7_{th} ed. 2010. (Cited on page 44.)

[65] Hiranaka, Y; Abe, T. "Gas dependent response in temperature transient of SnO_2 gas sensor" Solid-State Sensors and Actuators, 1991. Digest of Technical Papers, TRANSDUCERS '91., 1991 International Conference, p. 157-160, June 1991. (Cited on page 44.)

[66] Yamanaka, T.; Ishida, H.; Nakamoto, T.; Moriizumi, T. "Analysis of gas sensor transient response by visualizing instantaneous gas concentration using smoke" Sensors and Actuators A: Physical, Vol. 69, Issue 1, p. 77-81, June 1998. (Cited on page 44.)

[67] Jannot, Y.; Batsale, J.; Chausi, B. "Study of a transient non-intrusive sensor for internal temperature estimation during freezing" International Journal of Refrigeration, Vol. 27, Issue 6, p. 612-620, September 2004. (Cited on page 44.)

[68] Hudson, R.P. "Measurement of temperature" Rev. Sci. Instrum., Vol. 51, No. 7, July 1980. (Cited on page 44.)

[69] Eisinberg, A.; Fedele, G.; Frascino, D. "An analytic optimization procedure to estimate a first-order plus time delay model from step response" Control and Automation, 2008 16th Mediterranean Conference, p. 729- 734, June 2008. (Cited on page 44.)

[70] Taiwo, O. "Cheap computation of optimal reduced-order models for systems with time delay" Journal of Process Control, Vol. 9, Issue 4, August 1999. (Cited on page 44.)

[71] Bisdounis, L.; Nikolaidis, S.; Koufopavlou, O. "Analytical Transient Response and Propagation Delay Evaluation of the CMOS Inverter for Short-channel Devices" Solid-State Circuits, IEEE Journal, Vol. 33, Issue 2, p. 302-306, February 1998. (Cited on page 44.)

[72] Epstein, E. "Industrial Composting: Environmental Engineering and Facilities Management". *Boca Raton: CRC Press*. 2nd ed. USA, 2011. (Cited on page 67.)

[73] Moore, R. R. "Radio Communications in the Sea", IEE Spectrum, Vol 4, pp 42-51, November 1967. (Cited on page 67.)

[74] Chaamwe, N.; Liu, W.; Jiang, H. "Wave propagation communication models for wireless underground sensor networks", 12th IEEE International Conference on Communication Technology (ICCT), pp. 9-12, November 2010. (Cited on page 67.)

[75] Huerta, O.; López, M.; Soliva, M. "Procés de compostatge: caracterització de mostres", *Diputació de Barcelona*. 1st ed. Barcelona, 2010. (Cited on pages xii and 68.)

[76] Crespo, J. L. "Validación de varios sensores de humedad surante el proceso de compostaje", Degrea final project report. Universidad de La Laguna. Departamento de Ingeniería, Producción y Economía Agrarias. La Laguna, 2005. (Cited on pages 68, 88, 104, 120, and 127.)

[77] Al-Shamma'a, A. I.; Shaw, A.; Saman, S. "Propagation of Electromagnetic Waves at MHz Frequencies Through Seawater", IEEE Transactions on antennas and propagation, vol. 52, no. 11, November 2004. (Cited on page 68.)

[78] Badescu, A. M.; Fratu, O.; Halunga, S. V.; Marcu, I. M. "Consideration on Wave Propagation in Underground Dielectrics", 2009 Loughborough Antennas & Propagation Conference, 16-17 November 2009, Loughborough, UK . (Cited on page 69.)

[79] Liénard, M.; Degauque, P. "Natural Wave Propagation in Mine Environments", IEEE Transactions on antennas and propagation, vol. 48, no. 9, September 2000. (Cited on page 69.)

[80] Nelson, S. O. "Review and Assessment of Radio-frequency and Microwave Energy for Stored-grain Insect Control", Transactions of the ASAE, vol. 39, no. 4, p. 1475-1484. (Cited on pages 69 and 72.)

[81] Lucani, D. E.; Stojanovic, M.; Medard, M. "On the relationship between transmission power and capacity of an underwater acoustic communication channel," *OCEANS 2008 MTS/IEEE Kobe Techno-Ocean*, 1196-201, 2008. (Cited on page 69.)

[82] Green, O.; Nadimi, E. S.; Blanes-Vidal, V.; Jorgensen, R. N.; Drejer Storm, I. M. L.; Sorensen, C. G. "Monitoring and modeling temperature variations inside silage stacks using novel wireless sensor networks", Computers and Electronics in Agriculture, vol. 69, p. 149-157. (Cited on page 70.)

[83] Cuifen, L.; Jiwei, M.; Hua, F.; Ce, L.; Lei, S.; Jingjing, Y. "Wireless Monitoring System for Granary Based on 1-wire", 2010 International Conference On Computer Design and Applications (ICCDA 2010), vol. 4, p. 496-499. (Cited on page 70.)

[84] Parkinson, G.; Crutchley, D.; Green, P. M.; Antoniou, M.; Boon, M.; Green, P. N.; Green, P. R.; Sloan, R. and York, T. "Environment Monitoring in Grain", Instrumentation and Measurement Technology Conference (I2MTC), p. 939-943, Manchester, May 2010. (Cited on page 70.)

[85] Zhou, H.; Zhang, F.; Liu, J.; Zhang, F. "A Real-time Monitoring and Controlling System for Grain Storage with ZigBee Sensor Network", 5th International Conference on Wireless Communications, Networking and Mobile COmputing, 2009. WiCom '09, p. 1-4, Beijing, September 2009. (Cited on page 70.)

[86] Griffiths, D. J. "Introduction to Electrodynamics" *Prentice Hall*. 3rd ed. USA, 1998. (Cited on page 70.)

[87] von Hippel, A. R. "Dielectrics and waves"*John Wiley & Sons*, 1st ed. New York, 1954. (Cited on page 72.)

[88] Copenhagen. Status of CEPT/ERC Recommendation 70-03. "Relating to the use of short range devices (SRD)". Recommendation, 19 August 1999, p. 55. (Cited on page 81.)

[89] Rittenhouse. "Compost Moisture Meter" [on-line]. *Rittenhouse Since 1914* (Ontario, Canada): [Consulted on: June the 2nd of 2009]. Available at: http://www.rittenhouse.ca/ (Cited on page 87.)

[90] "Composter HQ. Backyard Compost Moisture Meter" [on-line]. *Backyard HQ* (Texas, USA): [Consulted on: June the 2nd of 2009]. Available at: http://www.composterhq.com/ (Cited on page 87.)

[91] Fratticcioli, E.; Dionigi, M.; Sorrentino, R. "Monitoring Moisture Content in Composting Process Using a Complex Permittivity Measurement System" , *MISA 2004 Atti del 2° Convegno Nazionale - Microonde nell'Energia e nelle Scienze Applicate*, Ancona, Italy, 6-8 October 2004, p.25. (Cited on page 87.)

[92] Fratticcioli, E.; Dionigi, M.; Valentini, F.; Sorrentino, R. "Monitoring moisture content in composting systems using a planar resonant sensor", *Instrumentation and Measurement Technology Conference, 2004.*

IMTC 04. Proceedings of the 21st IEEE , vol.1, pp. 339-342, 18-20 May 2004. (Cited on page 87.)

[93] Sheiretov, Y.; Zahn, M. "Dielectrometry measurements of moisture dynamics in oil-impregnated pressboard", Conference Record of the 1994 IEEE International Symposium on Electrical Insulation, Pittsburgh, PA USA, June 5-8, 1994, pp. 33-36. (Cited on page 87.)

[94] Tesla, N. "Electric condenser", U.S. Patent 464 667, 1891. (Cited on pages 87, 104, and 127.)

[95] Love, E. H. "Some electrostatic distributions in two dimensions", in Proc. London Mathematical Soc., vol. 22, Apr. 1923, pp. 339–369. (Cited on pages 87, 104, and 127.)

[96] Mortley, W. S. "Pulse compression by dispersive gratings on crystal quartz", Marconi Rev., no. 59, pp. 273–290, 1965. (Cited on pages 87 and 104.)

[97] Matis, I. G. "On multiparameter control of dielectric properties of laminate polymer materials", Latvijas PSR Zinatnu Akademijas Vestis Fizikas un Tehnisko, no. 6, pp. 60–67, 1966. (Cited on pages 87 and 104.)

[98] Sheppard, N. F.; Day, D. R.; Lee, H. L.; Senturia, S. D. "Microdielectrometry", Sens. Actuators, vol. 2, no. 3, pp. 263–274, July 1982. (Cited on pages 87 and 104.)

[99] Goldfine, N. J.; Washabaugh, A. P.; Dearlove, J. V.; von Guggenberg, P. A. "Imposed omega-k magnetometer and dielectrometer applications", Review of Progress in Quantitative Nondestructive Evaluation. New York: Plenum, 1993, vol. 12, pp. 1115–1122. (Cited on pages 87 and 104.)

[100] Von Guggenberg, P. A. "Applications of interdigital dielectrometry to moisture and double layer measurements in transformer insulation", Ph. D thesis report. Massachusetts Institute of Technology (MIT). Dept. of Electrical Engineering and Computer Science. USA, 1993. (Cited on pages 87 and 104.)

[101] Yang, L.; Tan, Yu.; Dong, L.; Mao, Z. "Measurement of grain moisture with a coplanar electrode capacitance probe", Journal-China Agricultural University, vol. 12; part 2, pp. 58-61. China, 2007. (Cited on pages 87 and 104.)

[102] Mamishev, A. V.; Sundara-Rajan, K.; Yang, F.; Du, Y.; Zahn, M. "Interdigital Sensors and Transducers", Proceedings of the IEEE, vol. 92, no. 5. May, 2004. (Cited on pages 88, 104, and 106.)

[103] Capone, S.; Siciliano, P.; Quaranta, F.; Rella, R.; Epifani, M.; Vasanelli, L. "Moisture inftuence and geometry effect of Au and Pt electrodes on CO sensing response of SnO2 microsensors based on sol-gel thin film", Sensors and Actuators B, no. 77, pp. 503-511, 2001. (Cited on pages 88 and 104.)

[104] Yu Li, L.; Fen Jiang, W.; Hua Xiao, S.; Fen Dong, Y.; Fang Ji, H.; Jian Li, X. "Effect of electrode configuration on capacitive humidity sensitivity of silicon nanoporous pillar array", Physica E, vol. 41, pp. 621–625, 2009. (Cited on pages 88 and 104.)

[105] Chen, T.; Bowler, N. "Analysis of a Concentric Coplanar Capacitive Sensor for Nondestructive Evaluation of Multi-layered Dielectric Structures", IEEE Transactions on Dielectrics and Electrical Insulation, Vol. 17, No. 4; August 2010. (Cited on pages 88, 104, 107, 126, 127, and 128.)

[106] Cheng, H.; Zhang, Y.; Huang, X.; Rogers, J.; Huang, Y. "Analysis of a concentric coplanar capacitor for epidermal hydration sensing", Sensors and Actuactors, pp. 149–153, August 2013. (Cited on page 88.)

[107] Chen, T. "Capacitive sensors for measuring complex permittivity of planar and cylindrical structures", Graduate Theses and Dissertations, Iowa State University, 2012. (Cited on page 88.)

[108] Indoor Health Products. "Relative Humidity Sensor Buying Guide" [on-line]. *Indoor Health Products, Inc*: [Consulted on: January the 24th of 2012] Available at: http://www.indoorhealthproducts.com/humidity-sensors-buying.htm (Cited on page 90.)

[109] Veris Industries. "Humidity" [on-line]. *Veris Industries Inc:* [Consulted on November the 2nd of 2014] Available at: http://www.veris.com/Category/Humidity.aspx (Cited on page 90.)

[110] Walker, C. S. "Capacitance, Inductance, and Crosstalk Analysis". Artech House Micro-wave Library. USA, 1990. (Cited on pages 91 and 105.)

[111] Study Guide. "Chapter 5. Capacitance and dielectrics" [on-line]. *MIT*: [Consulted on November the 2nd of 2014] Available at http://web.mit.edu/8.02t/www/materials/StudyGuide/guide05.p (Cited on page 91.)

[112] Electromagnetics, Electrostatics. "Edge Effects in a Capacitor" [on-line]. *Harvard University*: [Consulted on November the 2nd of 2014] Available at http://people.fas.harvard.edu/~lucas/Edge%20Effects%20in%20a% (Cited on page 91.)

[113] Bradley, M. "Edge Effects in the Parallel Plate Capacitor: The Maxwell Transformation and the Rogowski Profile " [on-line] *University of Saskatchewan*: [Consulted on November the 2nd of 2014] Available at http://physics.usask.ca/~bradley/pll_plate_edge.pdf (Cited on page 91.)

[114] Olssen, M. "AC/DC and Magnetic Modeling. TRAINING COURSE" COMSOL Minicourse. USA, 2011. (Cited on page 91.)

[115] Cole, K. S.; Cole, R. H. "Dispersion and Absorption in Dielectrics I. Alternating Current Characteristics", Journal of Chemical Physics, vol. 9, issue 4, pp. 341-352, February 1941. (Cited on page 93.)

[116] Florida Sola Energy Center, "Humidity" [on-line]. [Consulted on: March the 24th, 2011]. Available at: http://www.fsec.ucf.edu/en/consumer/buildings/basics/humidit (Cited on page 97.)

[117] Pozar, D. M. "Microwave Engineering". *Addison-Wesley Publishing Company*. 3_{rd} ed. 1993. (Cited on page 99.)

[118] Senturia, S. D.; Sheppard, N. F.; Poh, S. Y. and Appelman, H. R. "The feasibility of electrical monitoring of resin cure with the charge-flow transistor," Polym. Eng. Sci., vol. 21, no. 2, pp. 113–118, February 1981. (Cited on page 106.)

[119] Hobdell, J.L. "Optimization of interdigital capacitors", IEEE Trans. Microwave Theory Tech. MTT-27 (1979) 788–791. (Cited on page 106.)

[120] Esfandiari, R.; Maki, D.W.; Siracusa, M. "Design of interdigitated capacitors and their application to gallium arsenide monolithic filters", IEEE Trans. Microwave Theory Tech. 31 (1983) 57–64. (Cited on page 106.)

[121] Igreja, R.; Dias, C. J. "Analytical evaluation of the interdigital electrodes capacitance for a multi-layered structure", Sensors and Actuators A. 112 (2004) 291–301. (Cited on page 106.)

[122] Scott, K.J. "Electrostatic potential Green's function for multi-layered dielectric media", Philips J. Research, Vol. 45, pp. 293-324, 1990. (Cited on page 108.)

[123] Jackson, J.D. "Classical Electrodynamics", Chap. 3, John Wiley & Sons, Inc., third edition, 1999. (Cited on page 108.)

[124] Physics 8.02 Electricity and Magnetism Study Guide. "Capacitance and dielectrics" [on-line] . *Massachussets Institute of Technology*: [consulted on: January the 25th of 2012] Available at: http://web.mit.edu/8.02t/www/materials/StudyGuide/guide05.pdf (Cited on page 108.)

[125] Research and Education Association. "The physics problem solver". *Research & Education Association*. 4_{th} ed. USA, 2004. (Cited on page 109.)

[126] Li, N.; Zhu, H.; Wang, W.; Gong, Y. "Parallel double-plate capacitive proximity sensor modelling based on effective theory", AIP Advances. 4, 027119 (2014). (Cited on page 114.)

[127] Chen, T.; Bowler, N.; Bowler, J. R. "Analysis of Arc-Electrode Capacitive Sensors for Characterization of Dielectric Cylindrical Rods". IEEE Trans. Instrum. Meas. 61(1), 233–240 (2012). (Cited on page 114.)

[128] Ganssle, J.; Barr, M. "Embedded Systems Dictionary", p.173. (Cited on page 152.)

[129] Rillo, F. I. "Autonomous sensor system for the measure of temperature on composting piles and tunnels", Master Thesis report. Universitat Politècnica de Catalunya (UPC). Escola Politècnica Superior de Castelldefels (EPSC). Castelldefels, 2008. (Cited on page 152.)

[130] Wiederholt, R.; Jorgensen, M. "Livestock composting as an alternative disposal method" [online]. *North Dakota State University Agriculture*: [Consulted on: January the 11th of 2011] Available at: http://www.ag.ndsu.edu/ndsuag/. (Cited on pages xv and 160.)

[131] Finstein, M. S.; Miller, F. C.; Strom, P. F. "Monitoring and Evaluating Composting Process Performance". Journal (Water Pollution Control Federation). Vol. 58, No. 4 (Apr., 1986), pp. 272-278. (Cited on page 162.)

[132] Haug, R.T. "The practical handbook of compost engineering". *Lewis Publishers, Boca Raton*. USA, 1993. (Cited on pages xv, xviii, and 162.)

[133] Golueke, C.G. "Composting. A Study of the Process and its Principles". *Rodale Press*. USA, 1972. (Cited on page 162.)

COLOPHON

This thesis was typeset with LaTeX 2_ε using Hermann Zapf's *Palatino* and *Euler* type faces (Type 1 PostScript fonts *URW Palladio L* and *FPL* were used). The listings are typeset in *Bera Mono*, originally developed by Bitstream, Inc. as "Bitstream Vera". (Type 1 PostScript fonts were made available by Malte Rosenau and Ulrich Dirr.)

Final Version as of December 30, 2015 at 11:26.

DECLARATION

This Ph.D thesis has been realized under the supervision of J. Oscar Casas Piedrafita and within the studies framework of *Universitat Politècnica de Catalunya*. My rights to the ownership of the results and products from this thesis may be limited, but the learning and growing will be only own by me and will be part of my carreer forever.

I hope this work has been helpful to the scientific community. I hope this work can help others with their work or to encourage other to improve my work. I hope nobody has been negatively affected by this work and pray for a good impact in all the idividuals involved.

If anybody thinks this work is wrong or has strong feelings against it, I am sorry for it. I am satisified with my work and will not discuss any matter denigrating it whatsoever.

Thank you.

Castelldefels, from September 2008 to November 2015

Francesc Iu Rillo Moral